Time-Resolved Mass Spectrometry

Dissertation
zur Erlangung des Doktorgrades
der Naturwissenschaften

vorgelegt beim Fachbereich 14: Biochemie, Chemie, Pharmazie
der Johann Wolfgang Goethe-Universität Frankfurt/Main
in Frankfurt am Main

von
Tobias Lieblein
aus Offenbach am Main

Frankfurt am Main (2019)
(D 30)

vom Fachbereich 14: Biochemie, Chemie, Pharmazie
der Johann Wolfgang Goethe-Universität Frankfurt/Main
als Dissertation angenommen

Dekan	Prof. Dr. Clemens Glaubitz
Gutachter	Jun.-Prof. Dr. Nina Morgner (Fachbereich 14: Biochemie, Chemie, Pharmazie, Goethe-Universität Frankfurt/Main)
	Prof. Dr. Josef Wachtveitl (Fachbereich 14: Biochemie, Chemie, Pharmazie, Goethe-Universität Frankfurt/Main)

Datum der Disputation:

Abstract

Many processes in living cells involve interaction and cooperation of multiple proteins to fulfill a specific function. To understand biological processes in their full complexity, it is not sufficient to only identify the molecules being involved but also to understand the kinetic aspects of a reaction. Mass spectrometry (MS) is a very powerful tool which allows to precisely identify the molecules of a reaction. Usually this is done with tandem-MS experiments for purpose of de-novo peptide sequencing. However, since this involves protein digestion, a statement of the in-vivo constitution of non-covalently bound protein complexes is not possible. In order to detect an intact protein complex it is necessary to analyze the biological system softly and in a near-native environment with native MS. Native MS allows the non-destructive analysis of these non-covalent protein complexes as well as to detect their components. However, up to now native MS does not offer a possibility to resolve the timing of the constitution of protein complexes on a fast time-scale. Therefore, the progress of reactions on fast time-scales is invisible. However, a method which delivers both types of information - identification of the components of a protein complex, as well as time-resolving their interaction - would be of high interest.

A suitable ionization technique for native MS is laser-induced liquid-bead ion desorption (LILBID). LILBID employs well-defined droplets which are irradiated by IR laser pulses to generate gas phase ions. The not-continuous, repetitive nature of ion generation offers itself to the development of a time-resolved (TR) native MS system which is able to investigate protein complexes on a fast time scale. The LILBID-droplets can serve as reaction vessels if they are levitated in an electrodynamic Paul-trap. This new setup would allow sample manipulation and MS analysis on precise and fast reaction time-scales. The first part of this dissertation presents the construction and characterization of a setup for TR-LILBID-MS.

An example for a complex biological system is the self-assembly of beta-amyloid ($A\beta$). This small peptide is the major component in plaques related to Alzheimer's disease. Clinically relevant is especially the 42 amino acid peptide $A\beta_{42}$ which aggregates from monomers to oligomers through to fibrils. The oligomers are the neurotoxic species in this process and thus of high interest. Nevertheless, standard analytical techniques are unable to detect those oligomers which makes MS an optimal tool to study the oligomerization process of $A\beta$ with the focus on disease relevant oligomers. TR-LILBID-MS allows to follow the oligomerization of $A\beta$ enabling to study molecules which influence this kinetic. Combining MS with ion-mobility spectrometry adds an additional dimension - the collision cross section - to the mass-to-charge ratio obtained from MS. Therewith structural alterations induced by ligands can be correlated to differences in the aggregation kinetic. This allows to draw a picture of the aggregation process of $A\beta$ for the development of disease-relevant small oligomers on a molecular level.

Contents

Part I

Time-Resolved Mass Spectrometry

1

Introduction to Time-Resolved Mass Spectrometry

For the understanding of biological processes where multiple proteins contribute, two questions are of particular interest: which molecules are involved and how fast do those biological reactions progress? Regarding the first question, mass spectrometry (MS) is a well-suited tool which allows to accurately identify biological molecules. State-of-the-art ionization techniques (e.g. electrospray ionization, ESI) can maintain non-covalent interactions, which play a major role in the function of biological processes [1]. Nevertheless, these methods are not universally applicable. To overcome this issue the soft ionisation technique laser-induced liquid-bead ion desorption (LILBID) was introduced [2]. In LILBID, a piezo-driven droplet generator produces small droplets (50 µm diameter) containing the biological sample in a near-native aqueous solution. Infrared (IR) laser irradiation with a wavelength of 3 µm is focused on those droplets. By absorbing the IR light the droplet undergoes an explosive expansion which transfers the analyte of interest, e.g. proteins, RNA, DNA and their complexes, (solvated inside the droplets) into gas-phase. Thereby it is possible to maintain non-covalent interactions. Optionally the IR laser can be tuned to high energy mode, which allows to fully or partially dissociate the non-covalent bonds. The involved molecules can then be analyzed by Time-of-Flight (ToF). LILBID thus represents an ionization method that is highly suited in preserving the nature and stoichiometry of macromolecular complexes, or to determine constituing proteins [3].

To investigate fast time-scales on which biological processes occur it is necessary to link the LILBID technique with methodology for fast time-resolved mass spectrometry as up to now only biological processes in the minute to hour range can be followed [4]. The approach taken here to achieve the goal of fast time-resolved MS includes electrodynamic levitation of the sample droplet with a Paul-trap. The levitated droplet can now serve as a tiny reaction vessel: the sample within the droplet can be manipulated to start a reaction.The biochemical manipulation of the sample can either be done

via photochemical uncaging of one of the reaction partners or by combining two droplets each of them containing one of the reaction partners. After the reaction runs for a specific amount of time the droplet is released to the LILBID ionization source and analyzed by ToF. This allows to record series of mass spectra in dependence of the time the reaction undergoes inside of the droplet. Thereby, the full control of the reaction time can be maintained before LILBID-MS analysis which enables to measure time-resolved processes on a sub-second to minute timescale.
To enable the use of a droplet-levitating Paul-trap for the goal of time-resolved mass spectrometry the LILBID-MS instrument has to be refined. For this purpose it was necessary to design the Paul-trap electrodes, the electronics for the high voltage AC signals, as well as finding parameters which allow levitation and a controlled release of the droplet to the LILBID-MS instrument. The following part of this dissertation shows the development, testing and construction of a TR-LILBID-MS setup.

1.1 Native Mass Spectrometry

Investigating biological processes means analyzing molecules with high mass, complex structural elements and non-covalent as well as transient interactions [5]. Mass spectrometry is a very precise tool to identify molecules by their exact mass, to detect interactions between different biological molecules [1, 6, 7] as well as to study the structure and structural changes of big molecular complexes [6, 8–11]. Nevertheless, it is necessary to analyze biological molecules in near-native conditions to ensure the relevance of the MS investigations to the native environment of the molecule. Thereby some serious drawbacks occur.
The most critical step is to ionize the analyte of interest (AOI) in a way which retains the composition and the conformation of the sample as well as non-covalent interactions to other molecules, ligands and oligomeric partners. For this purpose two soft ionization techniques to ionize liquid samples are most relevant: ESI and LILBID [1, 6, 12].

Ionization Techniques In ESI the sample solution is injected into a metal coated glass capillary. High voltage of up to 5 kV applied to the metal coating drives the capillary to emit a spray of the sample solution. The high voltage leads to charge separation within the capillary and thus the evolving droplets

are highly charged. The consequence is a so-called Taylor-cone which appears due to a power balance between cohering (e.g. surface tension) and rejecting forces (e.g. Coulomb repulsion) [13]. The size of the droplets within that Taylor-cone shrinks due to solvent evaporation to the Rayleigh limit (when Coulomb repulsion of the charges equals surface tension of the solvent). This causes the droplets to explode. Thereby, micrometer sized droplets emerge [14] which carry the AOI, some solvent and a high amount of charges.

The exact mechanism for the production of sample ions out of those highly charged droplets is still under discussion [14, 15]. For protein ions it was shown with strong evidence that the size of the droplets decreases due to solvent evaporation and fission of the electrosprayed droplets (driven by Coulomb repulsion) to a ”zero-sized” droplet which only contains sample-ions and the remaining charges [16]. This ionization process occurs at atmospheric- and low vacuum pressure [13]. When solvent evaporation is done the ions are transferred to high vacuum where they are analyzed by their m/z value (where m is the mass of the ion and z the amount of elementary charges). The ionization via the ESI mechanism enables the analysis of non-covalent biomolecular complexes, highly specific and sensitive [5]. However, the complexity of the systems of interest brings about serious challenges.

Usually biological molecules are highly complex because they are composed of different subunits. Thus, the spectra of these complexes comprise many peaks. Since ESI produces a distributed number of highly charged ions, ESI spectra of biological systems are often difficult to analyze [17]. Signals may overlay which makes an unambiguous identification often very difficult.

The ionization via ESI is a soft ionization method. Nevertheless the preservation of soft non-covalent interactions often depends on salt- and buffer conditions. Both additives for conserving those interactions impact the ionization efficiency of electrosprayed sample molecules. Therefore a reduction in concentration is necessary as well as a substitution to more volatile agents. Together with Coulomb forces caused by the high amount of charges this makes the detection of soft non-covalent complexes challenging [1, 6]. Coulomb forces are also the reason for structural instabilities of sample molecules in the gas phase which lead to rearrangements and eventually the disruption of biological complexes [18]. Beside those specific interactions proteins may interact unspecifically and aggregate; those unspecific interactions appear predominantly at high concentrations [19]. Biological molecules appear sometimes in low concentration in their native environ-

ment. However, to differentiate between specific and unspecific interactions it is necessary to decrease the sample concentration for in-vitro experiments to near native conditions [5]. This challenges the limit of detection of the ESI-MS system [20].
Furthermore, the mechanism to artificially charge molecules requires a chemical element which accepts the charges. Thus, hydrophilic surfaces of biological molecules are region of ionization. Those hydrophilic surfaces can be found for soluble proteins. However, there are biological systems which are very challenging to investigate with ESI, such as integral membrane proteins (IMP) [3, 21–23]. As IMP are cellular proteins which are fully embedded in the cell membrane, their surface is completely hydrophobic. Those hydrophobic parts hardly gather charges. Furthermore, solubilization of hydrophobic IMP in a hydrophilic environment, which is a prerequisite for analysis with analytical tools, requires the use of amphiphilic substances like lipids or detergents. Those substances mimic the membrane of a cell by forming bilayers and micelles, respectively. Thereby the IMP are preserved from precipitation. However, analyzing membrane proteins with lipids or artificial detergents is challenging with ESI [24]. To prevent precipitation, it is not possible to remove the emulating substance of the liquid phase of ESI droplets e.g. by harsh ionization conditions. Therefore it is necessary to transfer the IMP in this emulating environment into gas phase followed by stripping off the membrane mimicry [25]. However, the force which is necessary to strip off the emulator entirely is high; on the other hand, to preserve the native conformation and constitution of proteins the ionization is desired to be soft. Thus, some emulators remain bound. The size and mass of those emulator-attachments are diverse, which makes it impossible to unambiguously detect IMP embedded in this synthetic environments.

To overcome the drawbacks of ESI-MS (to analyze biological complexe, especially IMP) another ionization technique was introduced, namely LILBID-MS [2, 26, 27]. Thereby a piezo-driven droplet generator produces droplets with a diameter of 30 or 50 µm. Those droplets contain the AOI in a near native environment including volatile buffers, salt, detergents and potentially additional additives. Those LILBID droplets are transferred into high vacuum where they are irradiated by IR lasers emitting light with a wavelength of 2.94 µm which excites the asymmetric O-H stretch vibration; due to high laser intensities non-radiative relaxation of the absorbed energy transfers the water molecules to a super critical state and thus the droplet undergoes an explosive expansion. Thereby the analyte of interest is transferred in its

natural charge state to the gas phase. Incomplete charge recombination leads to ionized molecules which can be accelerated by electric fields and the ToF can be measured [3].
LILBID has some advantages in terms of analyzing IMP and non-covalent complexes. The ionization process is more tolerant to high salt concentrations, detergents and buffers. Therefore, it is possible to analyze IMP via MS in near native conditions. A major critical aspect for the native analysis of IMP is the hydrophobic surrounding which are lipids in their native cellular environment. Those lipids can biochemically influence the appearance of IMP in terms of tertiary and quaternary structure [28, 29]. LILBID opens the possibility for investigating IMP in a lipid environment using nanodiscs [28, 30] and styrene maleic acid co-polymer lipid particles (SMALPs) [31]. Thereby it is possible to study the effect of lipids on the quaternary structure of membrane protein complexes.
Next to this, LILBID offers a good possibility to study non-covalent interactions of protein complexes. Since the intensity of the IR laser can be varied, the ionization with LILBID can be tuned between harsh and soft conditions. Thus it can be used to investigate the subunits of a protein complex individually or the whole intact protein complex, respectively. Thereby it was for example possible to investigate protein complexes of high mass like the MDa machinery of complex I of the respiratory chain of *Yarrowia lipolytica* [32], the interaction of the viral RNA TAR wild type and mutants to peptide ligands [33], the composition of the RNA polymerase II as well as a $F_O F_1$ ATP-synthase [34], and the native composition of the green absorbing proteorhodopsin [35]. Furthermore, LILBID enables to investigate the kinetics of oligomerizing peptides and proteins, so called amyloids (Part II of this dissertation gives a more detailed description of this investigation). Summarizing the properties of LILBID show that it is a well suited tool to investigate the behavior of amyloids as well as factors which influence their oligomerization and kinetics. Prerequisites for a MS ionization method to investigate amyloids is a technique for soft ionization which maintains non-covalent interactions, which has the possibility to detect high masses, which enables to analyze hydrophobic molecules, and which produces sample ions in low-charge states. Since these are the advantages of LILBID-MS, LILBID experiments enabled to study ligand effects on the oligomerization of amyloids. Thus it was possible to develop a molecule to inhibit the oligomerization of beta-amyloid ($A\beta$) which has advantages for a potential in vivo applications (see section 5.3.2 [4]).

Mass Analyzers Various techniques allow to analyze the *m/z* value of ions (e.g. orbitrap, ion cyclotron, sector fields, quadrupole, ToF). The instrument used for the studies presented in this dissertation analyzes masses by using quadrupole and ToF mass analyzers. In a quadrupole radiofrequency (RF) AC signals of high voltages are used to guide ions through four cylindrical electrodes. Thereby the trajectory of an ion with a given *m/z* is just stable for a specific frequency and voltage. By detecting the transmission of ions during scanning the RF frequencies it is possible to determine the *m/z* values of the analyte ions present in the sample solution [36]. However, the analysis of AOIs with a high m/z ratio requires high voltages and low frequencies. This limits the range in *m/z* quadrupoles can analyze.

A technique which is in theory unlimited in *m/z* range and which shows high resolution is ToF [1]. In ToF the ionized AOI is accelerated by an electric field followed by a drift within a field-free region. Due to the electric energy

$$E_{el} = \frac{1}{2} \cdot \frac{Q}{U} \tag{1.1}$$

(where *Q* is the amount of charges which equals the amount *z* of elementary charges *e*, and *U* is the electric voltage) the AOI is accelerated having a kinetic energy

$$E_{kin} = \frac{1}{2} m v^2 \tag{1.2}$$

where the velocity *v* is depending on the AOIs mass *m*. Thus, by measuring the time *t* the AOI needs to travel through the field-free drift region *s* enables by calculating

$$m/z = \frac{e}{U \cdot s^2} \cdot t^2 \tag{1.3}$$

to determine the *m/z* value. Combining mass analyzers (e.g. quadrupole and ToF) enables to measure multidimensional mass spectra (MS^n). Thereby it is for example possible to analyze with the second mass filter the composition of a complex detected with the first mass analyzer. For this purpose the first mass analyzer is a quadrupole for detecting the species of the AOI complex, followed by a cell which enables to manipulate the sample ions. Most common in native MS the manipulation is due to collisions to an inert buffer gas which results in collision induced unfolding (CIU) and collision induced dissociation (CID) of the complex which was detected in the first mass analyzer. The second mass analyzer can now be used to study the composition of sub-units out of which the complex detected in the first mass

analyzer is combined. Those techniques enable a precise determination of the analyte's mass and can thereby provide conclusions on its composition.

1.2 Ion Mobility Spectrometry

Next to studying the composition of molecules by their mass with MS experiments it is possible to analyze the structure of molecules, especially biological molecules, in ion mobility spectrometry (IMS) experiments [12, 17, 37, 38]. Thereby the charged molecules produced on either one of the ionization methods described above are accelerated by electric fields through a drift cell filled with an inert buffer gas. This method (being reviewed in Gabelica et al. [39]) measures the drift time t_D of the ions traversing the drift tube with the length l under influence of an accelerating electric field E which results in a certain mobility K of the ions:

$$K = \frac{v_D}{E} = \frac{l}{t_D E} \tag{1.4}$$

The velocity v_D of the ions depends on the amount of collisions the analyte undergoes with the buffer gas. Relevant parameters are the gas number density (N), temperature (T) and the gas pressure (p). For standard conditions this results in

$$K = \frac{3}{16}\sqrt{\frac{2\pi}{\mu k_B T}} \cdot \frac{ze}{N\Omega} \tag{1.5}$$

where k_B is the Boltzmann constant, ze the charge of the analyte molecule, μ the reduced mass of analyte molecule and buffer gas and Ω the collision cross section (CCS). Since MS offers the possibility to determine the mass and charge of the analyte a combination of these methods in a single instrument enables to calculate the CCS from the mobility K after calibration for the instrumental parameters. The simplest setup uses a linear electric field E accelerating the ions through the drift tube [37]. This enables to calibrate CCS either by measuring drift times t_D at different strength of the electric field E [40] or by sensibly measuring instrumental parameters like gas pressure p, temperature T, etc. [41]. However, nowadays a traveling-wave (TW) electric field is used more often than a linear electric field. Radio frequency (RF) electric fields guide ions through the drift tube instead of a linear voltage gradient. This speeds up the ion sepa-

ration resulting in less ion loss during the IM experiment [37]. Nevertheless, TW-IM lacks the possibility of easy calibration which can be used with a linear electric field. For TW-IM a set of calibrants with known CCS has to be used for calibration. CCS are available in databases like `http://depts.washington.edu/bushlab/ccsdatabase/#native`. The calibration of the IM signals will correct for the variation of instrumental parameters. This procedure is discribed well in Ruotolo et al. [42]. Thereby the measured drift time t_D is corrected for the mass-to-charge ratio m/z and the instrumental parameter C 'enhanced duty cycle':

$$t'_D = t_D - \frac{C\sqrt{m/z}}{1000} \tag{1.6}$$

Also the calibrant's cross section is corrected for the charge and the reduced mass of analyte and buffer gas:

$$\Omega' = \frac{\Omega}{ze \cdot \sqrt{\frac{1}{\mu}}} \tag{1.7}$$

When t'_D is plotted against $ln(\Omega')$ the fit expression of

$$\Omega' = X \cdot lnt'_D + lnA \tag{1.8}$$

delivers the fit-determined constants A and X (which include the instrumental parameters). With those values the CCS of an unknown sample can be determined when measured under the same experimental settings.
Using the IMS technique it is possible to answer questions on structural biology with low resolution [43]. Nevertheless, IMS has some advantages over established high-resolution methods like X-ray diffraction or nuclear magnetic resonance (NMR) spectroscopy. X-ray diffraction is for example limited regarding the solution conditions which can be used since it is necessary to grow protein crystals. Crystallizing proteins is time intensive and not always successful. Since many proteins do not crystalize (for example a lot of membrane proteins or flexible proteins as well as flexible parts lacking a stable 2D structure) this limits the amount of structures being possible to study [44]. NMR on the other hand requires a lot of isotopically labeled sample in a high concentration. Additionally for both established methods it is difficult to study unstructured proteins and proteins with unstructured parts. IMS on the other hand has the ability to study proteins in a solution which can be described as native-like [41]. Furthermore, IMS enables to study the structure of oligomerizing samples, separately for each of the oligomeric species.

Combining IMS with MS adds mass selectivity to IMS signals which enables to unambiguously differentiate between various oligomeric species of a protein. Furthermore, IMS enables to probe the stability of a certain structure by determining the drift time t_D with different collision energies in a CIU and CID experiment.
Nevertheless, the CCS determined by IMS can be compared to theoretical CCS derived from PDB structures. However, this comparison of structures from X-ray diffraction and NMR with those from IMS is not unconditionally possible. This is due to various influencing factors. For IMS it is necessary to transfer the AOI from solution into gas-phase. This alters intramolecular interactions, especially hydrophobic ones, which leads to structural changes [45]. Furthermore, the molecules studied by ESI-IMS contain net charges which differ from its solution charge state. A different charge state also might distort the conformation of the AOI due to Coulomb repulsion. Both factors have to be accounted for when comparing IMS results to solution structures. Molecular dynamic (MD) simulations are an optimal tool to simulate the behavior of a given structure in the situation as a charged molecule in gas-phase rather than being electrically neutral in solution [45]. This allows to compare theoretically calculated CCS from an electrically neutral solution-phase structure with experimental CCS determined for charged molecules in gas-phase with IMS. These investigations help to identify molecules influencing the structure of a protein.

1.3 Time-Resolved Mass Spectrometry

Several approaches to achieve time-resolved (TR) MS analysis were published within the last decade [46, 47]. The majority focusses on non-universally applicable techniques [48, 49], the analysis of the reactions of small molecules [50–52] and only some of the publications focus on native protein analysis by MS [53–55]. All of the approaches for the time-resolved analysis of native proteins use ESI as ion source. That way it was possible to achieve a minimum time-resolutions of 10 µs for the analysis of structural changes of small soluble proteins like cytochrome c [53]. A reaction is started by mixing the reaction components. The mixing was either achieved with rapid mixing of two components in stopped- and continuous-flow devices followed by ionization of the mixed compounds [47] or via the crossing of the sprays of two ESI sources followed by the reaction of the charged compounds within combined droplets of both sprays [53]. Both ways of time-resolved mixing

show drawbacks for the TR-MS analysis of protein ions. The approach of a rapid mixing device gives a good control of a stoichiometric combination of the mixed components since every separate component is adjustable with the starting concentration. But the method is limited to time-resolutions of minutes to seconds [55]. The latter approach of mixed ionization sprays indeed brings the possibility for subsecond kinetic measurements. However, the mixing occurs on ESI droplets with a distribution in their size; thus it lacks control over the stoichiometric ratio of the mixed components. As described above ESI is a good ionization source for soluble proteins but it has issues to detect hydrophobic membrane proteins. Therefore, it was not possible until now to measure TR spectral changes of hydrophobic proteins. Additionally, ESI has limitations in analyzing amyloid peptides. A TR analysis of non-covalent protein complexes, and thereby of high masses was not published before. A lot of those drawbacks could be overcome by TR-MS measurements using the LILBID ionization technique. As the previous paragraph shows LILBID has some advantages over ESI for analyzing native proteins, especially membrane proteins, and non-covalent interactions. Additionally, it would allow to control the starting point of a reaction and time resolution in a manner that cannot be achieved with ESI.

To observe biological reactions with LILBID-MS two methods to trigger the reaction start are conceivable: either two separated reactants are combined or one of the reactants is chemically caged to prevent the biochemical reaction. In terms of TR-LILBID-MS both methods prevent mentioned drawbacks of TR-ESI. Mixing two reactants can be achieved by combining two LILBID-sample-droplets each of them containing one single reactant. This enables to maintain the control of the component's concentration as well as allows for a good time-resolution since the droplet's volume is small and the mixing of the components is performed rapidly before the MS analysis. The second method to trigger the start of a reaction involves caged compounds which consist of the AOI chemically linked to a photolabile protecting group (PPG). The PPG prevents the biochemical reaction and can be released upon irradiation with the correct wavelength. Various strategies exist to design those molecules in order to provide proper absorption as well as proper chemical and biochemical properties [56–59]. Chromophores are designed to have a reddish absorption to minimize photodamage to the biological sample molecules; solubility and toxicity of the PPGs are also main targets for the design strategies. Since the PPGs are equipped with a chromophore which absorbs specific wavelength of light it is possible to use optical radiation to

release the PPG and to set the AOI free. Using optical radiation results in a very precise temporal reaction control. This good time-resolution can be combined with the accuracy to identify molecules by mass spectrometry.
For TR-LILBID-MS experiments it is necessary to manipulate the sample molecules solvated in the LILBID-droplets in either one of those ways. To accurately achieve this manipulation and to control the stoichiometry and the concentration of the reaction partners as well as to maintain the exact control of the reaction time after sample manipulation and prior to MS analysis, it is necessary to levitate the respective sample droplet. Levitation of particles can be achieved on different ways: magnetically, optically, aerodynamically, as well as acoustically or electrodynamically (in a Paul trap) [60]. A lot of those levitation techniques cannot be applied due to technical reasons: for transfer reasons of the droplet to the ionization area in the MS instrument the droplet has to be levitated in vacuum. This necessity excludes the levitation methods which use air to produce the levitation force (e.g. aerodynamic and acoustic levitation). Electric fields are easy to control and good to shield to the active area of levitation. Thus, the best option for particle levitation in terms of TR-LILBID-MS is electrodynamic levitation.

1.4 Electrodynamic Levitation

The most descriptive picture of an electrodynamic levitation using a Paul trap tells an anecdote by Wolfgang Paul himself [61]. Once he was preparing for breakfast in bed with his wife. He was bringing two eggs with different masses on a tray. The eggs started to roll down the tray but to counteract the motion of the eggs he shook the tray periodically. This made it possible to confine the larger egg, but the smaller one still rolled down the tray. By increasing the frequency of his shaking though, it was possible to stop the movement of the smaller egg with the disadvantage of restarting the movement of the big egg. That morning Wolfgang Paul realized the possibility of oscillating forces to levitate particles and to mass select them by varying the frequency. In 1989 he received the Nobel Prize for his idea using oscillating electric fields as tray and ions as eggs.
Since the first publication in 1953 [62] the Paul trap was used very often as mass analyzer or as ion guide in mass spectrometers [63, 64]. But next to ions it is also possible to use the Paul trap to levitate charged particles [60, 65–73] as the only relevant difference of particles and ions is the amount of mass and charges.

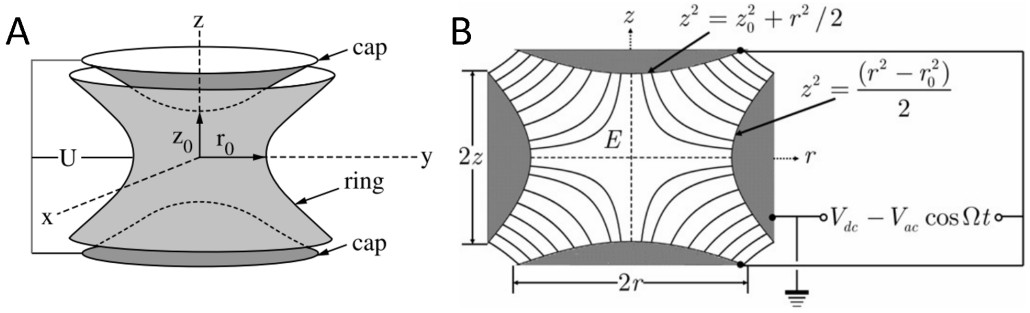

Fig. 1.1: Scheme of an electrodynamic Paul trap. A shows the composition of the electrodes.Three electrodes are shown: two cap- and a ring electrode [74]. B shows equipotential lines of the electric field when an electric AC field of the form $V_{DC} - V_{AC} \cdot cos(\Omega t)$ is applied [75]. The dimensions r_0 is the radius of the ring electrode and $2z_0$ is the separation of the two cap electrodes.

The architecture of a cylindrical Paul trap contains three electrodes, all of them with a hyperbolic surface. Two of those electrodes are essentially the same namely the cap-electrodes; the third electrode is confined as a ring thus it is called the ring-electrode (compare figure 1.1A). The arrangement of hyperbolic electrodes and thus hyperbolic force fields is called quadrupole. Figure 1.1B shows the electric equipotential lines when an electric AC field of the form $E = V_{DC} - V_{AC} \cdot cos(\Omega t)$ is applied (where V_{DC} is a DC potential, V_{AC} an AC potential, Ω the angular frequency).

All of the electrodes are driven with AC voltages where frequency and amplitude are chosen depending on various factors, especially the mass to charge ratio of the ion or particle to be levitated. The two cap-electrodes are driven by the same AC signal whereas the signal of the ring-electrode has a phase shift of π. Due to those forces the motion of the levitated particle never stagnates; therefore it is called electrodynamic. However, by choosing the correct parameters the AC character of the force field confines the particle to a periodic motion in a small volume.
The first mathematical description of a periodic motion of a particle within an unstable field was given in 1868 by Par M. Emile Mathieu [76]. He established a theory of region-depending stability and instability which can be adapted to a particle motion within an electric field - the so called Mathieu equation:

$$\frac{d^2u}{d\xi^2} + (a_u + 2q_u cos(2\xi)) = 0 \tag{1.9}$$

where *u* represents the coordinate axes *x, y, z* and ξ is a dimensionless parameter equalling $\omega t/2$ so that ω is a frequency at the time *t*; a_u and q_u are

also dimensionless parameters known as the trapping parameters. Reference [77] delivers a solution to solve the Mathieu equation for the purpose of ion trapping in a Paul trap.
Substitution by $\xi = \frac{\omega t}{2}$ and multiplication by *m* brings the equation to the form of

$$m\frac{d^2u}{dt^2} = -\frac{m\omega^2}{4}(a_u + 2q_u cos(\omega t))u \tag{1.10}$$

which already can be interpreted as a force of a particle in any direction. The force acting on a charged particle within an electric field is given by

$$F = m\frac{d^2u}{dt^2} = -e\frac{d\Phi}{du} \tag{1.11}$$

where Φ is the electric potential and *e* is the charge of the particle. In a quadrupole field the potential can be expressed as

$$\Phi = \frac{\Phi_0}{r_0^2}(\lambda x^2 + \sigma y^2 + \gamma z^2) \tag{1.12}$$

where *x, y* and *z* are the room coordinates which are summarized in *u*; λ, σ and γ are weighting constants. To fulfill the Laplace condition the weighting coordinates have to have the relation $\lambda + \sigma + \gamma = 0$ which is in case of an ion trap achieved by $\lambda = \sigma = 1$ and $\gamma = -2$. Substitution of those values and transformation from Cartesian to cylindrical coordinates modifies equation 1.12 into

$$\Phi = \frac{\Phi_0}{r_0^2}(r^2 - 2z^2) \tag{1.13}$$

An electric field which is applied in the form of $\Phi_0 = U + Vcos(\omega t)$ (being U a DC voltage, V the amplitude of the AC voltage, $\omega = 2\pi f$ the angular frequency) transfers equation 1.11 into

$$m\frac{d^2u}{dt^2} = -\frac{2e}{r_0^2}(U + Vcos(\omega t))u \tag{1.14}$$

Combining equation 1.14 with equation 1.10 gives an expression for the trapping parameters in z-direction:

$$a_z = -\frac{8eU}{mr_o^2\omega^2} \tag{1.15}$$

$$q_z = \frac{4eV}{mr_0^2\omega^2} \tag{1.16}$$

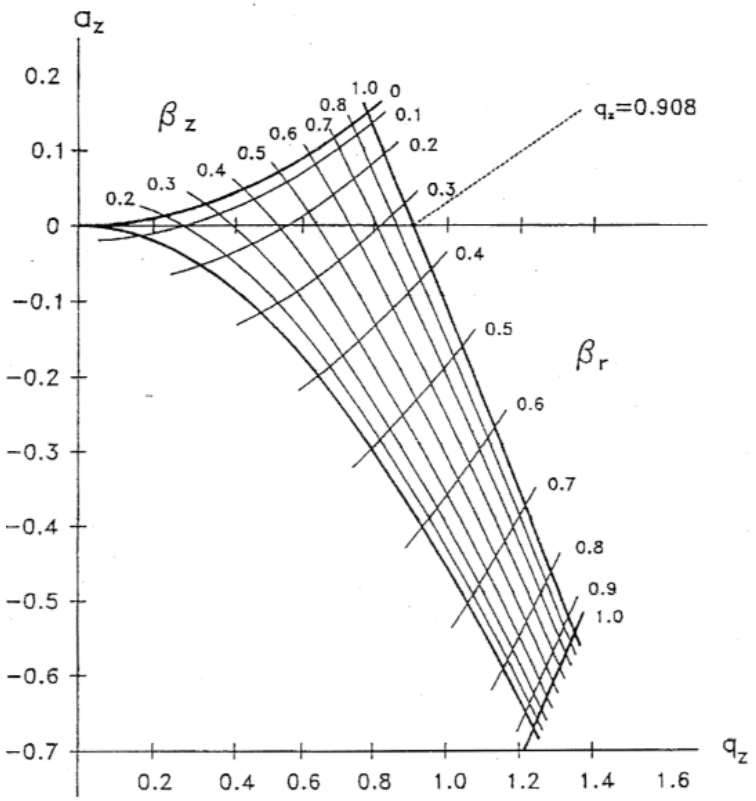

Fig. 1.2: Stability plot for an electrodynamic Paul trap having the parameter a_z as Y- and q_z as X-axis [64].

Equations 1.15 and 1.16 include the parameters of mass m and charge e, AC and DC voltage (V and U, respectively) as well as the frequency of the electric potential ω and the dimensions of the trap r_0. Thus, the variation of those parameters is relevant to obtain a stably levitated particle [77]. It was shown that particles are stably levitated if conditions were chosen that the values a_z and q_z are within the following regions [78]:

$$a = \frac{1}{2}q^2 + \frac{1}{128}q^4 - \frac{29}{2304}q^6 + \frac{68687}{18874368}q^8 \tag{1.17}$$

$$a = 1 - q - \frac{1}{8}q^2 + \frac{1}{64}q^3 - \frac{1}{1536}q^4 - \frac{11}{35864}q^5 \tag{1.18}$$

By plotting these curves on a Cartesian coordinate system where a_z and q_z are chosen as axes the result is a ”necktie shaped” stability plot (figure 1.2).

If conditions are chosen correctly to levitate a particle in the electrodynamic environment the particle will move on a certain trajectory; a typical one is shown in figure 1.3. The movement of a particle can be described by a so called Lissajous curve [77].

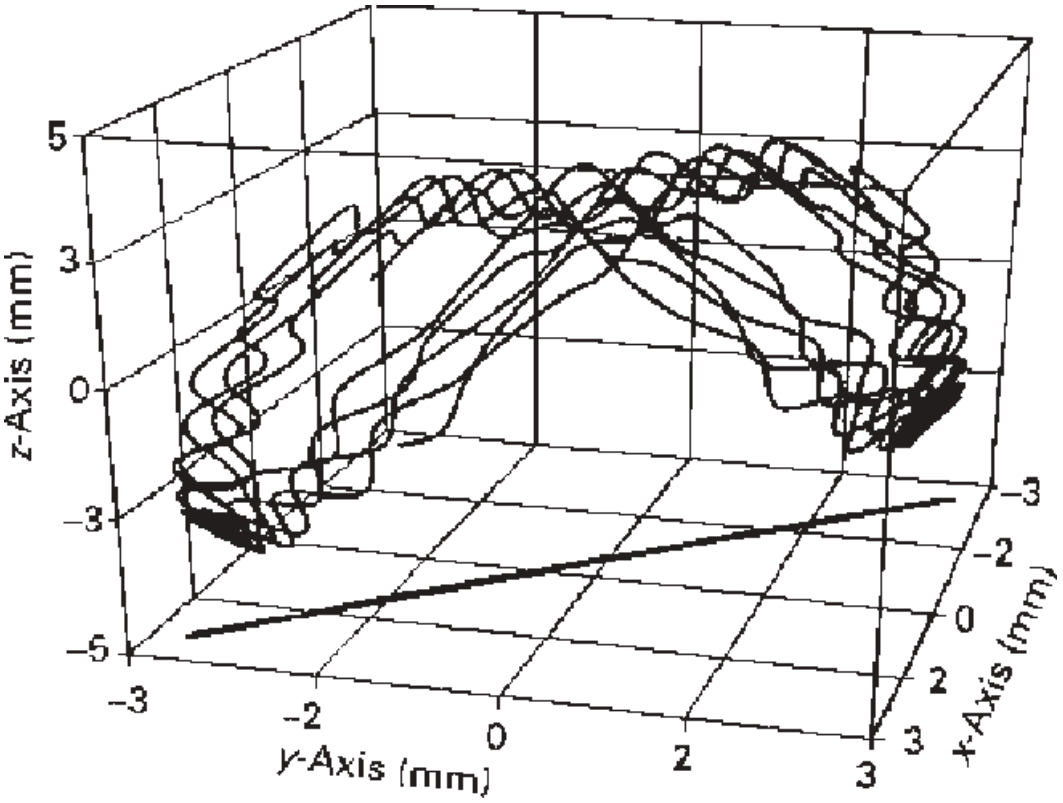

Fig. 1.3: Typical trajectory of an ion within a electrodynamic trap [79].

This shows that ”levitated” does not imply that the movement of the particle stagnates, but the movement is periodical so that the particle is confined within a small volume.

1.5 Electrodynamic Droplet Levitation

The expression ”particles” is not limited to ions and solid materials, but it also includes liquid droplets in air. Also the electrodynamic levitation of liquid particles is goal of research. In most of the cases research on the levitation of liquids aims to study the atmosphere [68, 80–86], just in some few cases electrodynamic droplet levitation is applied for different issues, e.g. to use a micrometer sized droplet as tiny reaction vessel [69, 70, 72, 87, 88].
Here the droplets are used as reaction vessels and levitated for the purpose of TR-LILBID-MS measurements. The LILBID droplet described in section 1.1 has to be charged prior to levitation in an electrodynamic Paul trap. The solvated sample can be manipulated on either one of the ways described at the beginning of section 1.3: either by mixing two separate droplets contain-

ing two reactants or by uncageing a molecule containing a PPG via laser radiation on the levitated droplet to start a reaction. After reaction start the droplet remains in the trap for a controlled reaction time before it is released to the MS instrument where LILBID-MS measurements can be performed. A critical step in this process is the charging of the droplet which allows electrodynamic levitation. This can be achieved inductively by applying a DC voltage to an electrode nearby the tip of the droplet-generating glass capillary. The voltage of this electrode results in charge repulsion of likely charged ions inside the sample solution. During droplet extraction this results in a charged droplet with a charge opposite to the electrode. By varying the voltage of the charging electrode it is possible to control the droplet's charge. This is a very important feature since droplets are not dimensionally stable. The amount of charges Q in combination with solution properties (e.g. surface tension σ, viscosity ν, temperature T) and the size of the droplet determine the stability of charged droplets in an electrodynamic Paul trap [15, 87, 89]. If the droplet contains too many charges the force of charge repulsion is higher than the cohering forces of viscosity and surface tension resulting in the appearance of Rayleigh-jets leading to loss of micro droplets from the main droplet [87]. This changes the mass m and charge e of the droplet which influences the stability parameters a and q (equation 1.15 and 1.16) for electrodynamic levitation and thus the levitated droplet becomes unstable (Figure 1.2) and the levitation terminates.

2

Developing a Droplet Trap for the Purpose of Time-Resolved Mass Spectrometry

For performing time-resolved LILBID-MS measurements it is necessary to ensure the start of a reaction at a precisely defined starting point. This requires the possibility to manipulate the molecule of interest which is solvated in the droplets which can be achieved by electrodynamic levitation of the droplet in a Paul trap. Since stable levitation requires a very exact determination of the parameters, a test-setup was used. This enabled the construction of the different components and the evaluation of the exact parameters before work-piece construction to adapt the TR-setup to the LILBID-MS instrument.

2.1 Characterizing the Process of Droplet Levitation on a Test-Setup

To develop a test setup, we had to calculate and construct the electrodes for the Paul trap, design the electronics to apply stable AC high-voltage signals to generate electric fields which can levitate heavy particles, as well as to characterize the influence of various parameters on the efficiency of droplet levitation. This section describes the design and characterization of all of the components of the test-setup. A detailed description of the materials and methods which were used and the participation of colleagues to the results is given as supplementary information 8.

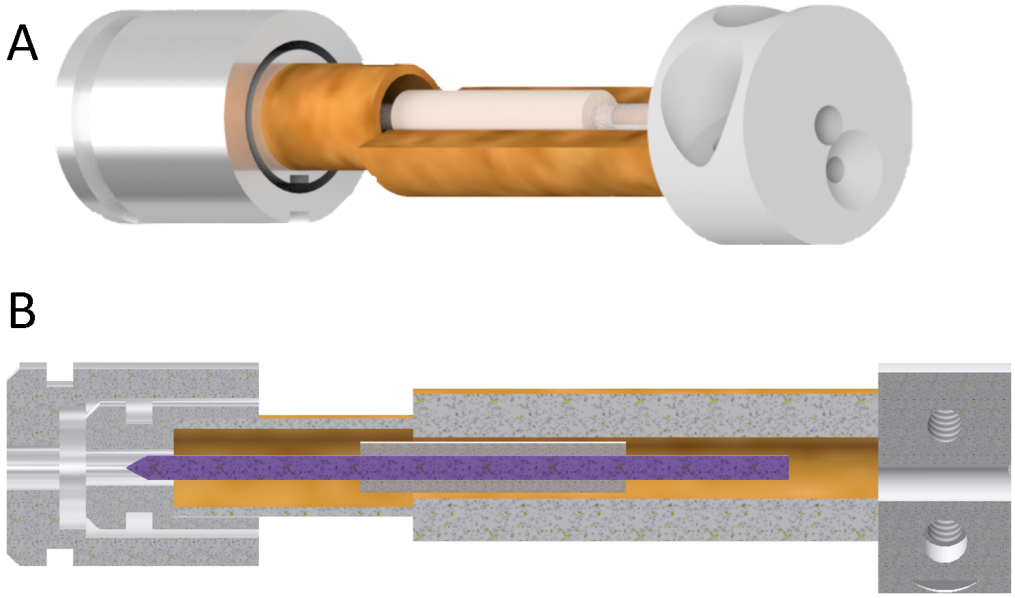

Fig. 2.1: Construction of a piezo-driven droplet generator to produce charged droplets. The housing for the piezo-surrounded borosilica glass-capillary is made of the thermoplastic polymer polyether ether ketone (PEEK). The aluminium electrodes for charging as well as for grounding are wired for applying an electric potential. A shows the whole construction including PEEK case (yellowish), charging and grounding electrode (on the left) and the piezo surrounded glass capillary. B shows a profile of the construction: position of the glass capillary (violet) inside the PEEK case and the charging electrode is shown.

2.1.1 Designing a Setup for Droplet Levitation

Storing a droplet in a Paul trap requires production of charged droplets. So the first step is to develop a system for charged droplet generation with a controllable size (and thus mass) and charge to enable stable trapping in a Paul trap. Therefore, the principle of commercially available piezo-driven droplet generators by Microdrop Technologies GmbH were model for a homemade construction. These commercial droplet generators are too big to place them close to the Paul trap and they do not produce charged droplets.

As explained in section 1.1 droplet generation for LILBID-MS uses piezo-driven droplet generators. This principle was also base for the production of charged droplets. To produce droplets in a reproducible way, borosilicate glass capillaries were pulled to have a finite nozzle with a diameter of 50 µm. A tubular piezo-crystal was adhered to one of these capillaries by hot glue which maintains the possibility to change the capillary for the purpose of

different nozzle diameters or to replace a clogged capillary. By applying voltage pulses of 0 V to 200 V with a duration of 10 µs to 100 µs and a frequency of 10 Hz to 1000 Hz droplet production from the glass nozzle is possible. The piezo-surrounded glass capillaries are assembled to a casing made of polyether ether ketone (PEEK). Figure 2.1 shows a CAD drawing of the complete system to produce charged droplets on demand; figure 2.1A shows the complete system including the PEEK case, the two electrodes, one for droplet charging and one for shielding of external electric fields, as well as the glass capillary which is surrounded by a cylindrical piezo ceramic. Figure 2.1B shows a profile of the setup for droplet generation. The glass capillary is colored violet for better visualization. Applying charges to those droplets can be achieved inductively. Thus, the forefront of the glass capillary (violet in figure 2.1B) is enclosed by a aluminum tip which is used as charging-electrode. DC voltages of 0 V to 500 V on the charging electrode lead to charge separation inside the solvent which fills the glass capillary and droplets emerging from the droplet generator carry a net-charge. Increase of the voltage of the charging-electrode results in droplets with an increased amount of charges. The tip of the droplet generator is positioned close to the ring-electrode of the Paul trap which has a high-voltage potential. This potential can influence the charge state of the droplet. To avoid this it is necessary to shield against its electric field to maintain the full control of the droplet charge by the charging-electrode. Therefore, a ground-electrode surrounds the charging-electrode with the task to enable the control of the droplet's charges exclusively by the voltage of the charging-electrode. Both electrodes are sealed by shrinking tubes for the purpose of electric isolation (not shown). This setup enables to produce droplets with a controllable size and charge which are prerequisites for a reproducible and reliable electrodynamic levitation.

Since Paul traps are widely used, it is well known which electrode dimensions perform best also for particle levitation [74]. This knowledge was base for the construction of an electrode-system for the purpose of droplet levitation in a former diploma thesis [90].
The result of the former construction was base for the herein developed TR-LILBID-MS setup. Figure 2.2 shows a CAD construction of the Paul trap's electrode system (two cap-electrodes, a ring-electrode and isolation mounting). Due to an adequate machinability all the electrodes were made of brass (golden and yellow, shiny color) whereas a ceramic (Macor®) was

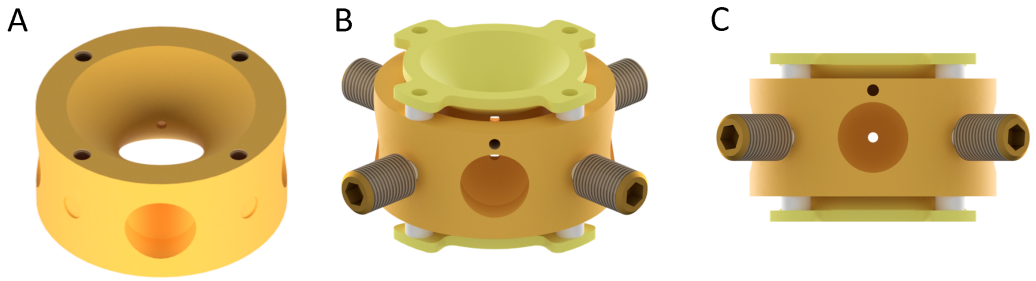

Fig. 2.2: Confinement of the electrodes building the Paul Trap for electrodynamic droplet levitation. A shows the ring-electrode with openings for droplet injection and observation of the levitated droplet. B shows the assembly of both cap-electrodes (yellow) to the ring electrode and the isolated mounting of the electrode system by four ceramic pins. C shows a lateral view of B: determination of the distance between ring- and cap-electrodes is due to ceramic cylinders between the electrodes. The two cap-electrodes and the ring-electrode are made of brass, all white isolations are made of a machinable ceramic (Macor®).

used for isolation between the electrodes (white tubes) as well as between the electrodes and the grounded housing (four ceramic pins). The shape of all the electrodes is hyperbolic with an inner radius of the ring-electrode r_0 of 7 mm. Figure 2.2A shows that four holes with a diameter of 0.85 mm are implemented in the ring electrode which enable to inject droplets as well as to observe the levitated droplets. Those holes also have a pre-chamber to bring the droplet generators closer to the interior of the trap. The two cap-electrodes also have a hole (figure 2.2B) to allow for additional entry-ways for the purpose of UV irradiation on the levitated droplet (hole in the upper cap electrode) as well as droplet release to the LILBID-MS instrument (hole in the lower cap electrode). The cap-electrodes have wings which allow their attachment to the ring-electrode. This builds a stable construction maintaining the distance between the electrodes. To precisely adjust the distance between cap- and ring-electrode, ceramic tubings with a length of 2.4 mm deal as spacer (figure 2.2C). Cables which apply the high-voltage AC signals are screwed to the electrodes: in terms of the ring-electrode a thread is drilled (figure 2.2B), in terms of the cap-electrodes they can be fixed at the ceramic screws. To mount this electrode system in a box four ceramic pins are clipped to the ring-electrode (figure 2.2B and C). These can be fixed by screws to the case to stably locate the electrodes.

For a stable performance of the Paul trap for droplet levitation the electric AC potentials have to match the geometry of the electrodes. To roughly find those parameters calculations of the movement of a charged particle

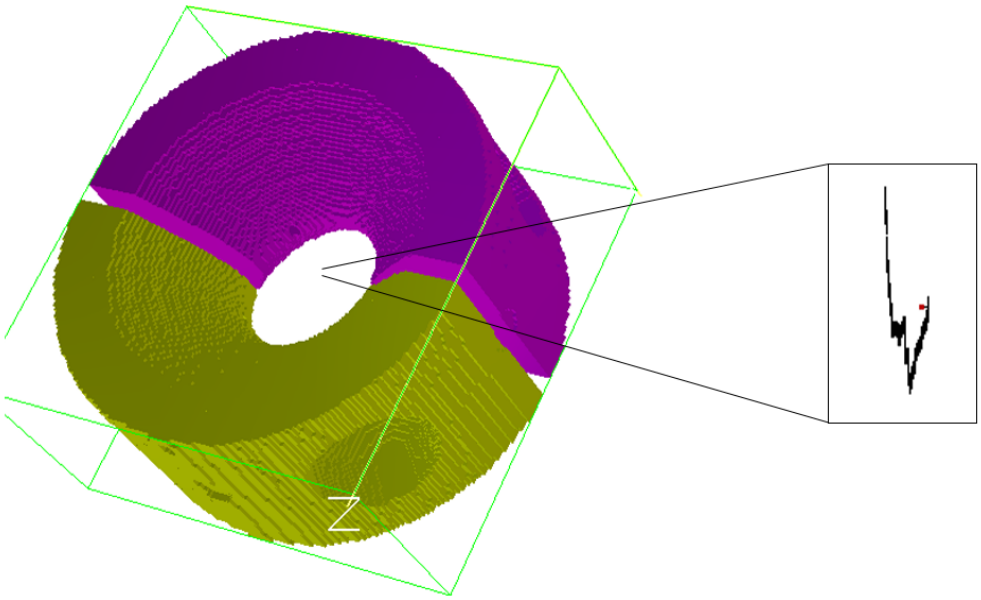

Fig. 2.3: *Simion* calculations can predict droplet movement in the high-voltage AC field of the Paul trap. The confinement of electrodes used for *Simion* calculations is shown. Base for the electrode surface is the CAD construction of the ring-electrode shown in figure 2.2. The inset shows that placing a charged particle with the properties of a droplet inside this theoretical setup results in the periodic movement.

with mass and charge comparable to the droplet in the environment of high-voltage AC potentials can be simulated using the software *Simion*.
Figure 2.3 depicts the setup of these simulations. The geometry of the electrodes used for this calculations can be converted from the CAD construction in figure 2.2. For simplicity reasons it is divided in two parts (yellow and purple). However, by applying the same potential to both parts of this electrodes an electric field similar to a 360° electrode is produced. Inserting a charged particle into this environment will move it in the direction of the respective electric force. If the time-dependent electric field has a sinus character, the movement of the particle will result in a harmonic vibration. Droplets used for LILBID-MS experiments do usually have a diameter of 50 µm which leads to a mass of $4{\cdot}10^{16}\,u$ of the simulated particle, the charging electrode can cause a net-charge of the droplet of about 2 pC [90]. Applying an AC voltage with an intensity of 3000 V peak-to-peak and with a frequency of 250 Hz results in a harmonic motion of this high-mass particle (inset in figure 2.3). To account for gas pressure of this non-vacuum situation, collisions to gas-molecules are also implemented in the *Simion* simulation. This simulated movement resembles parts of the Lissajous curve describing the movement of ions in a Paul trap (compare figure 1.3). Those simulations are sophisticated with the

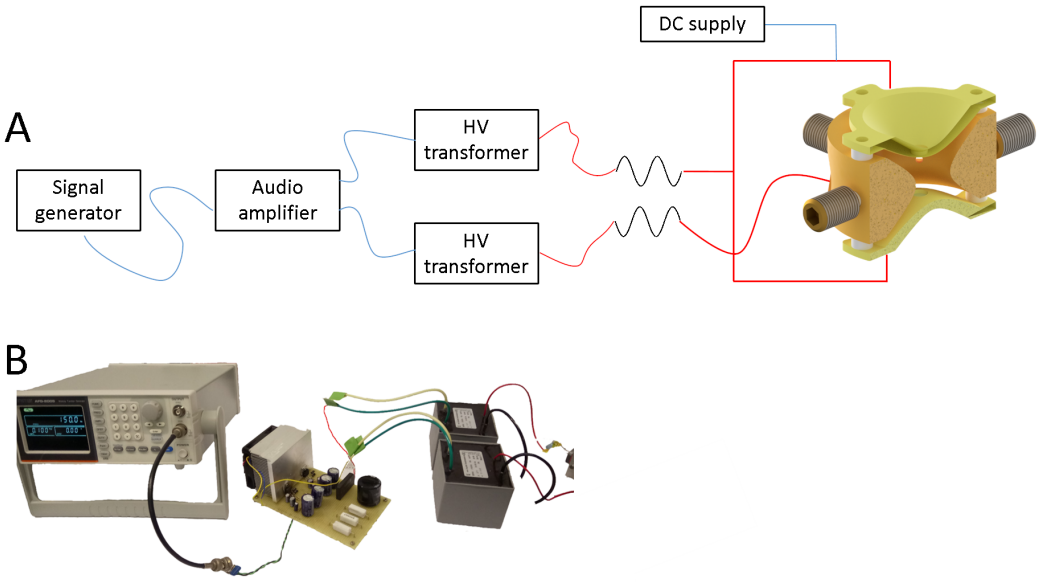

Fig. 2.4: Depiction of the electronics to drive the Paul trap with stable and adjustable high-voltage AC signals. A shows a schematic of the signal generation. Blue wires represent low-voltage and red wires high-voltage connections. Additional to the AC signal a DC voltage can be applied to the upper cap-electrode. A picture of the preliminary electric setup is shown in B.

need for considerable computer resources since the simulation of collisions to gas molecules is effortful. Therefore, the simulation time has to be limited. Nevertheless, properties which do not match the requirements for a stable levitation led to an instability of the levitated particle much earlier than the time used for this simulation.
This simulation reveals properties of an electric field which will result in a stable levitation of a charged droplet. Thus an electronic setup has to be developed which is able to produce electric fields complying with the parameters matching the simulations.

Generating high-voltage AC signals at radio-frequencies is relatively straight forward. The situation changes when instead of MHz smaller frequencies in the Hz range shall be generated; this is necessary because the Paul trap is supposed for the unconventional application to levitate water droplets. For this purpose a signal generator produces sinus signals which can be tuned in frequency between 0 Hz and several kHz and in amplitude between 0 V and 5 V. This signal is split and pre-amplified by an audio amplifier. This is the base for amplification by transformers to high voltage. Thereby the signal's amplitude is amplified by a factor of 1000. The two separate signals, which were originally generated by the same signal generator get phase-shifted by

180° and used as input for the two separate sides of the electrode system of the Paul trap: one side is connected to the ring-electrode whereas the other side is connected to both cap-electrodes. A scheme of this setup is shown in figure 2.4A; B shows a picture of the preliminary test setup. Adjusting the potential regarding amplitude, frequency or signal form, is achieved by changing the respective parameter on the signal generator. Additional to this AC signal a DC potential can be applied to one of the cap electrodes. This DC voltage can compensate for the force of gravity acting on the levitated droplet.

This test setup allowed to produce charged droplets in a controllable fashion which can be inserted in the hyperbolic electrode system forming a Paul trap.

2.1.2 Finding Parameters for Stable Droplet Levitation

To assess the functionality of the Paul trap setup to levitate droplets the test-setup was used to evaluate the effect of the electric potentials, as well as the influence of different parameters of solution properties. Videos of the droplets inside the Paul trap were recorded to evaluate how those parameters influence the achievable time-span each of the droplet's levitation as well as the area in which the Lissajous-like movement appears (a scheme of this procedure is depicted as supplementary figure 8.1). Optimization of both parameters is necessary to maintain the full control of the droplet levitation; increasing the achievable levitation time would enable to investigate long time scales of a reaction. Minimizing the expansion of the Lissajous movement is desired to facilitate the transfer of the levitated droplet to the MS instrument.

The properties of the high-voltage AC potentials were expected to have the strongest effect on the functionality of the Paul trap. The results found during *Simion* calculations were base for evaluation of optimal settings of the AC signals. Therefore, frequency as well as the amplitude were analyzed for their influence on the levitation; figure 2.5 depicts these results.
The first column shows the influence of varying the AC signal's amplitude. Levitation of the droplet is limited to a certain time after which the droplet disappears. However, it is desired to achieve indefinite levitation times to enable the analysis of long-term reactions; reason for this limitation is unknown but has to be evaluated. Clearly the achievable levitation time decreases upon voltage increase (figure 2.5A). The sigmoidal Blotzmann fit describes a smooth continuous decrease of the achievable levitation time. While these experiments show that the voltage of the levitating electric field can influence the time span over which a droplet can be stored in the trap before it is lost, the achieved storing times are not sufficient to use the trap as planned for unrestricted investigations of the time-dependence of biological reactions. After several seconds of levitation the droplet becomes unstable and disappears. A levitation for more than 5 s was not possible. We therefore endeavored to uncover the reason behind the loss of the droplet from the trap. During levitation charged particles stand high forces which can influence the properties of mass and charge which are relevant for stable levitation (compare the next paragraph for figure 2.6B). Therefore a limit

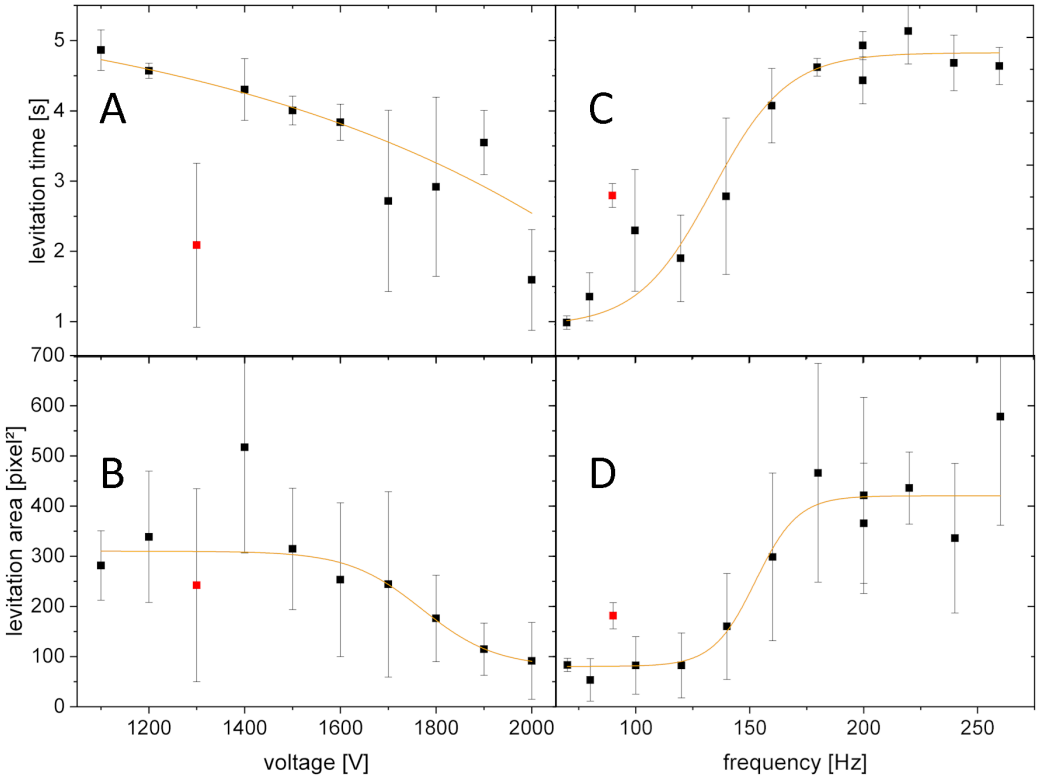

Fig. 2.5: Frequency and amplitude of the high voltage AC signal do influence levitation just slightly. A shows the droplet's levitation time depending on the amplitude of the trap's AC signal; B depicts the influence of the amplitude to the droplet's area of confinement. The right pictures show how the frequency of the HV AC signal influences the levitation. C shows the influence on the levitation time, D on the volume of the droplet's confinement. The yellow fits do have a sigmoidal Boltzmann character.

of the achievable levitation time is not necessarily related to a less stable levitation caused by the AC settings, but it might be related to an unstable confinement of the charged droplet. The voltage of the trap electrodes might for example influence the droplet charge. Since the trap produces AC electric fields, its influence on the droplet charge is time-dependent, depending on the phase of the AC signal.

Nevertheless, an increase in the AC amplitude focuses the droplet levitation to a smaller area. Figure 2.5B shows that the area where the droplet is levitated decreases for high AC voltages. By increasing the voltage from 1100 V to 2000 V the radius of Lissajous-movement decreases by nearly a factor of three. This is due to an increase of the electric forces which constrain the droplet in its path. Enlarged forces can accelerate the periodic movement of the droplet more intense which brings the droplet movement to a smaller expansion.

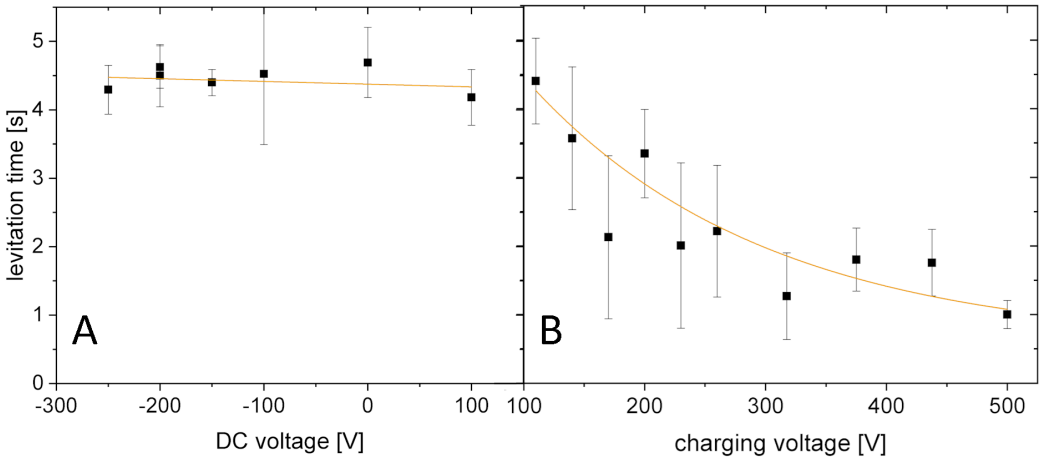

Fig. 2.6: Levitation time depends on the charge of the droplets. The DC voltage between the cap-electrodes was varied in A. No influence on the stability of the droplet in the trap was observed. The linear fit is nearly constant. B shows that the duration of stable levitation decreases exponentially with the voltage of the charging electrode leading ti differently charged droplets.

The influence of the AC frequency on the droplet levitation is depicted in the right column of figure 2.5. C reveals that the electrodynamic levitation for a 50 µm droplet gets more stable with an increase in the frequency from 60 Hz to 260 Hz. The time-span of a droplet being stably levitated increases massively within this frequency range implying a more suitable use of frequencies above 200 Hz. On the other hand figure 2.5D shows that with an increase in the levitation time there comes an increase of the area to which the levitated droplet is confined. A compromise between a longer duration and a smaller confinement of the Lissajous-movement has to be made since it is necessary to optimize both properties. Therefore an amplitude of 2000 V and a frequency of 150 Hz were chosen for the following experiments.

The DC voltages which can be applied to the cap-electrodes are of interest, as they could be used to compensate for the gravity acting on the levitated droplet.To check for the influence of this value on the levitation time different voltages from -250 V to $+100$ V were applied and droplet levitation was recorded. Figure 2.6A shows that different DC voltages do not influence the stability of the droplet in the trap; the linear fit is nearly constant. Thus gravity compensation is not the reason for the disappearance of the levitated droplet. Neither a highly attracting voltage of -250 V, nor an repelling voltage of up to $+100$ V influence the levitation time. Besides it does

not influence the area of levitation (not shown). The DC voltage allows to control the vertical position of the particle's Lissajous-movement (higher or lower in the trap depending of an attracting or repelling voltage of the upper cap-electrode, respectively). Nevertheless, the stability of the droplet in the Paul trap is not affected by the DC voltage.

Influence of the amplitude of the trap's AC voltage on the achievable times for droplet levitation (figure 2.5A) imply that the charge state of the droplet has a crucial role. To vary the charge state of the levitated droplets more reproducibly, different voltages were applied to the droplet generator's charging electrode. The DC voltage of the charging-electrode of the droplet generator varies the charge state of the droplets. Figure 2.6B shows clearly that by increasing the amount of charges of the droplet the levitation time decreases exponentially. Most probably this is due to the appearance of Rayleigh-jets; Rayleigh-jets are the evolvement of micro-droplets from a droplet due to charge repulsion (compare section 1.5) [87]. If Rayleigh-jets change the droplet's mass m and charge z the particle reaches an area of the stability diagram (compare figure 1.2) where it becomes unstable and is not levitated anymore.
Thus, Rayleigh-jets for highly charged liquid particles explain the decrease in levitation time due to an increase in the amount of charges. To solve this issue the voltage of the charging electrode has to be reduced and the droplet ejection has to be synchronized to the Paul trap's AC field.

However, to effectively levitate a particle a specific force is required. For electrodynamic levitation this force can be described by $F = z \cdot e \cdot E$ (where e is the electric constant and E the electric field, which includes the potential of the electrodes). Thus, a decrease of the droplet's charge requires an increase in the electric potential of the Paul trap's electrodes. Due to small distances between the high-voltage electrodes and due to an insufficient isolation an increase above 2000 V of the electrode's potential is not possible. However, none of the tested parameters allowed droplet storage for a time which would be sufficient for planned experiments. Thus, Rayleigh-jets need to be suppressed which can be done by evaluating different solution parameters on the levitation of droplets. Cohering forces in a liquid droplet are surface tension and viscosity. They counteract the disrupting force of coulomb repulsion. The surface tension of a water droplet can be controlled by the

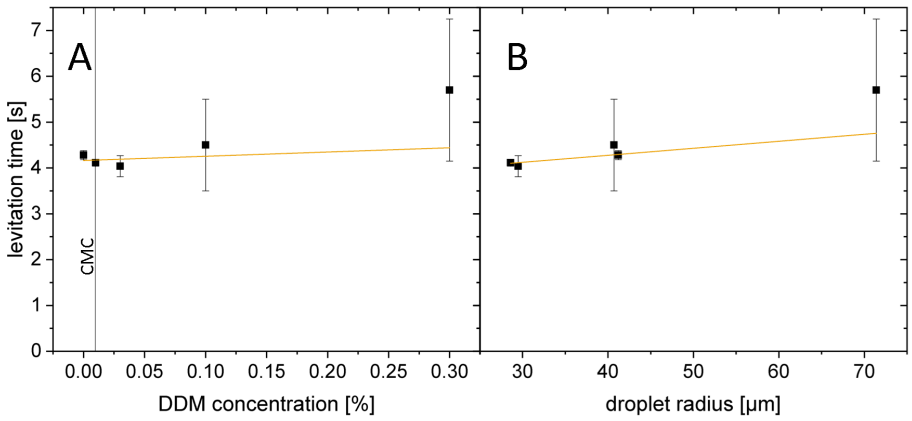

Fig. 2.7: Surface tension and droplet size do not influence levitation time. A shows the levitation time depending on the concentration of DDM which influences the surface tension of liquids. B shows that for the same measurement also the droplet size is varied by the DDM content. The linear fits are nearly constant in both cases.

addition of surfactants like *n-dodecyl-β-D-maltoside* (DDM) [91]. Increasing the amount of surfactants to the *critical micelle concentration* (CMC) results in the formation of micelles which is known as a characteristic for detergent molecules. For DDM the CMC is about 0.2 mM or about 0.01 % V/V [91]. The evolvement of micelles is correlated to a decrease in surface tension of the solvent droplet. Figure 2.7A shows that the time-span of droplet levitation is not influenced by different concentrations of DDM. Even for high concentrations of about 30-fold of the CMC, a levitation for maximum 5 s was possible, comparable without DDM. A reduction in surface tension is also related to an increase in the droplet size. Figure 2.7B shows that the size of droplets was efficiently varied by various concentrations of DDM but without an effect on the levitation time.
The results of this experiment exclude the surface tension of droplets as a major influencing factor on the stability of the droplet's entity and thereby on the levitation time-span.

Different concentrations of glycerol in water were used to test how viscosity influences the stability of droplet levitation. Figure 2.8A reveals that adding 5 % of glycerol to the solution increases the levitation stability massively. Taking the influence of the droplet charge into account enables to levitate the droplet for an indefinite amount of time. The levitation of the droplet is still unstable if the amount of charges is too high. Nevertheless, a stable

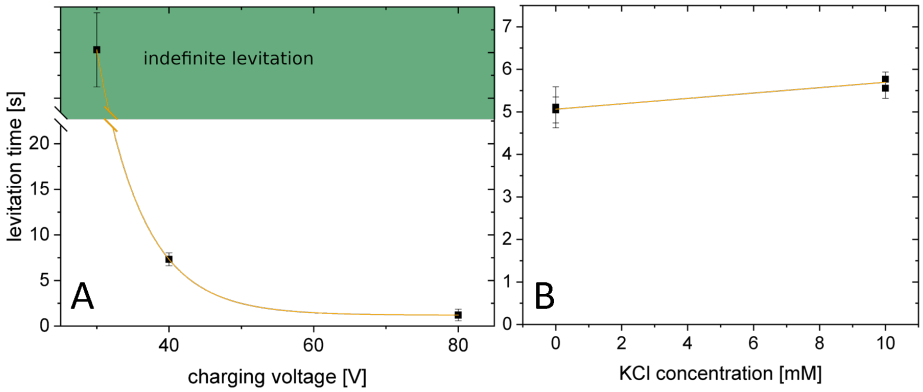

Fig. 2.8: The addition of glycerol changes levitation behavior. A shows the levitation time of the droplet containing 5 % of glycerol for different voltages of the charging electrode. B shows the levitation time for a KCl containing droplet.

levitation for an indefinite amount of time is possible by glycerol addition in combination with a decrease of the potential of the droplet-generator's charging-electrode. A minimum of 5 % of glycerol is necessary to increase the stability of the droplets to a level where an indefinite levitation is possible. This enables the future application to investigate long reaction times.
However, Glycerol is influencing two solution parameters coincidently: the electric conductivity and the viscosity [92]. To uncover the reason for this increase in levitation stability droplets were levitated with different potassium chloride (KCl) concentrations. The addition of KCl provides potassium and chloride ions which modulates the conductivity similar to glycerol. Figure 2.8B shows that the levitation stability is unaffected by the addition of ions to the solvent. This rules the conductivity as a factor for influencing the levitation stability out.

These experiments reveal that the determining factor for indefinite droplet levitation is the viscosity. A stable droplet levitation is enabled when the cohering force viscosity of the solvent is higher than the force of charge repulsion. The appearance of Rayleigh-jets is the effect which is relevant for the instability of a levitated droplet after several seconds. Addition of 5 % glycerol leads to an increase of the stability of droplets and allows levitation for indefinite times.
Since the target of the development of this TR-MS setup is the analysis of biologic systems any additive might hinder an unimpaired analysis. Nevertheless, glycerol in a concentration of several percent is an additive well known for preparation, storage and use of biological molecules [93]. Thus,

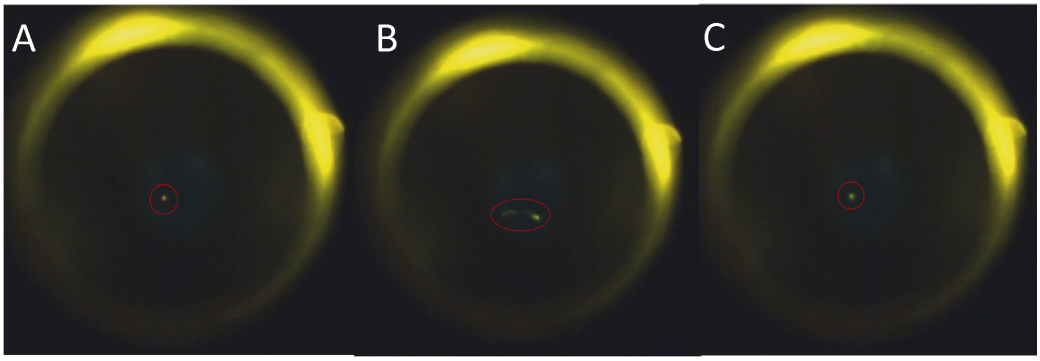

Fig. 2.9: Mixing two levitated droplets with opposite charges. A shows a negatively charged levitated droplet in the trap. Injecting a positively charged droplet (B) leads to Coulomb-driven attraction. If the charges of the two droplets were chosen correctly, the resulting droplet (C) is stably levitated in the Paul trap. Taken from [94].

the addition of glycerol has a low effect on the target systems. Furthermore, it was shown that the addition of detergent molecules like DDM, which are especially necessary for analyzing membrane proteins (compare section 1.1), does not hinder the droplet levitation.

Stable droplet levitation is crucial for a time-resolved analysis of reactions. Section 1.3 explaines that a reaction which will be analyzed by TR-MS can either be started via irradiation with a UV laser resulting in uncaging of a reactant or via mixing of two droplets containing two reactants. To irradiate the sample solvated in the droplet to start a reaction was shown to work straight forward [58]. UV irradiation of a droplet will not influence the process of electrodynamic levitation. More challenging is the second procedure for reaction start. By mixing two droplets in the Paul trap the particle's parameters of mass as well as of charge change upon mixing. Thus, this method requires to adapt the droplet's parameters to the situation after droplet combination. Since the mass of the combined droplet is double of the mass of a single droplet, also the charge of the combined droplet has to be double to maintain the droplet's m/z relation. Figure 2.9 shows the process of droplet combination observed through the recess of the upper cap-electrode. Figure 2.9A shows a levitated droplet containing 10 % glycerol negatively charged by a charging-electrode. Figure 2.9B shows the situation where a second oppositely charged droplet is injected into the Paul trap. Due to the opposite charge of the second droplet they attract each other leading to an effective mixing. The opposite charges compensate each other and the combined droplet has twice the mass of the single droplet. To still allow levitation the charge state of the second droplet has to be triple that of the

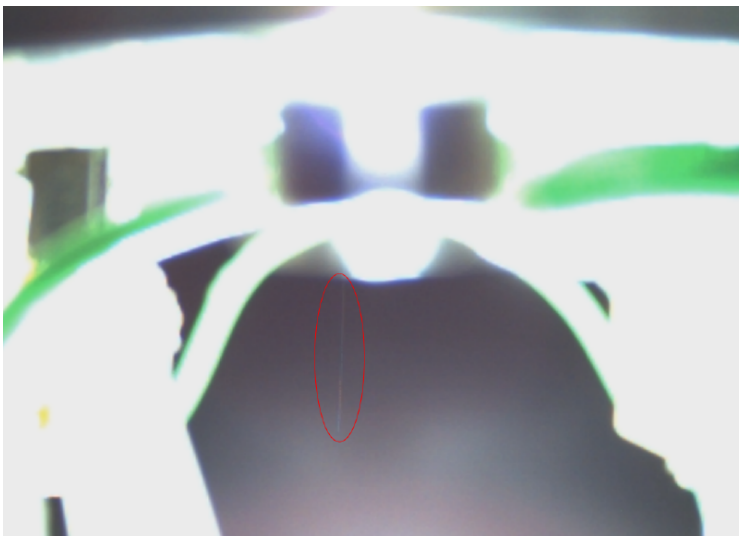

Fig. 2.10: Droplet release from the trap is possible by interruption of the HV AC voltage. The picture is recorded with a camera below the trap using 4 pulsed LEDs to illuminate the droplet. Considering the phase of the trap's AC voltage, a precise droplet ejection through the bottom aperture is possible. The red circle shows a falling droplet accelerated by gravity. Taken from [94]

first one. Voltages of the charging electrodes were scanned for optimal storing of the mixed droplet; $+283$ V and -83 V were found to be most suitable. After mixing the two droplets the Lissajous-movement of the joint droplet covers a larger area. Figure 2.9C shows that the averaged movement during illumination recorded with the camera occurs in an enlarged volume but a stable electrodynamic levitation of the bigger droplet is still possible for an indefinite amount of time. Nevertheless, a change of the levitation behavior (e.g. the increased levitation area) is evidence for a successful mixing of two droplets in the Paul trap during levitation.

Stable droplet levitation and combination of two droplets are prerequisites for TR-MS setup. The droplet has to be transferred from the Paul trap to the MS instrument for LILBID-MS experiments. This requires ejection of the levitated droplet in an exact trajectory.
The pathway for droplet ejection is through the recess in the lower cap-electrode. Turning off the Paul trap's AC voltage during levitation leads to a loss of the gravity-countering force and the droplet is accelerated by gravity towards the lower cap-electrode. Figure 2.10 shows a picture of a falling droplet recorded beneath the test-setup. As seen in figure 2.10 the droplet's trajectory is not pointing directly towards the bottom but it is falling at an angle compared to the direction of gravity. As described in section 1.4 particles

do move during electrodynamic levitation. The magnitude and the direction of a periodic movement are strictly related to the phase of the AC potential. For an effective release of the droplet on a straight trajectory the release has to be phase-matched to the AC signal. Just for some strict time-points droplet ejection through the recess of the lower cap-electrode is possible. A straight direction of the ejected droplet is necessary to exactly convey the droplet through the capillary of the transfer stage to the high-vacuum of the MS instrument.

The test-setup made it possible to build components, evaluate and test different parameters which influence a stable electrodynamic levitation of a droplet. With the design described in this section it is possible to produce droplets in a controlled manner (in terms of size and trajectory) as well as to accurately apply electric charges to those droplets. A Paul trap electrode system was constructed which is electrically isolated to apply high voltage potentials of up to 2000 V. Some recesses were implemented which make it possible to inject charged droplets as well to observe the levitated droplet and to eject it from the trap. *Simion* calculations were used to roughly determine the electric parameters of the high-voltage AC potential necessary to levitate the macroscopic masses of droplets. The result of those calculations were used to construct the electronics to apply HV signals to the Paul trap's electrodes. These constructions make it possible to levitate the droplets produced with piezo-driven droplet generators. Parameters of the trap's AC potential (in terms of frequency, amplitude and DC potential) as well as of the droplets (in terms of charge state and solvent composition) were optimized which results in a stable levitation for an indefinite amount of time. This enables to implement the method of combining two droplets to start a reaction. The last step that had to be tested before constructing a work-piece which can be adapted to the LILBID-MS instrument is the ejection of the levitated droplet from the trap. The results achieved with the test-setup enable to construct a work-piece with optimal parameters for droplet levitation. In cooperation with the in-house workshop for precision engineering a CAD construct of an extension for the LILBID-MS instrument was designed and a work-piece was constructed.

2.2 Designing a Paul Trap as Extension for LILBID-MS

For time-resolved LILBID-MS it is necessary to transfer a levitated droplet to the MS instrument. Due to a turbulent airflow, a transfer of a droplet from ambient pressure to the high vacuum of an MS instrument is not possible. Thus, the pressure of the interior prior the high-vacuum has to be lowered to several mbar.This means that the droplet has to be levitated in a hermetically sealed environment at low pressure. However, embedding the Paul trap setup into a case is not straightforward. A compromise on small distances for the workability of the system (e.g. in terms of droplet injection, exact positioning of the droplet generator, illumination of the levitated droplet and production of an undisturbed electric field) as well as on distances which are large enough to enable electric isolation between the electrodes among themselves as well as towards the grounded potential of the case is necessary. It further involves to implement an air entrance to precisely control the pressure inside the levitation chamber, as well as a manometer for pressure readout. Pressure-sealed cable passages for driving the droplet generator with its charging electrode, the high-voltage potentials of the Paul trap and to energize the LED illumination are required to maintain full control of the pressure with a valve on the air inlet. This section describes the construction of the setup for extending the LILBID-MS instrument for time-resolved measurements. Details on materials and methods used for this design are given in the supplementary information 8.

Figure 2.11 shows the CAD construction of the LILBID-MS extending Paul trap setup; A shows the whole work-piece and B a sectional drawing. The case is made of aluminum centered around the Paul trap with four extensions. Two extensions are used as inlets for two droplet generators, each positionable by X-Y-stages (1 and 7 in figure 2.11). The extensions perpendicular to these deal as conduct for the Paul trap's electric signals (6) as well as for a view onto the levitated droplet with a camera through a fused silica window (8). The illumination system of the levitated droplet as well as pressure control of the levitation chamber are contained at the lid on top of the case: a fused silica window (3) enables irradiation of the levitated droplet by an UV laser for the purpose of reaction start via uncaging (compare section 1.3). Optical control of the droplet levitation is possible by lightning of the Paul trap interior with four LEDs (13) which illuminate the inside of the Paul

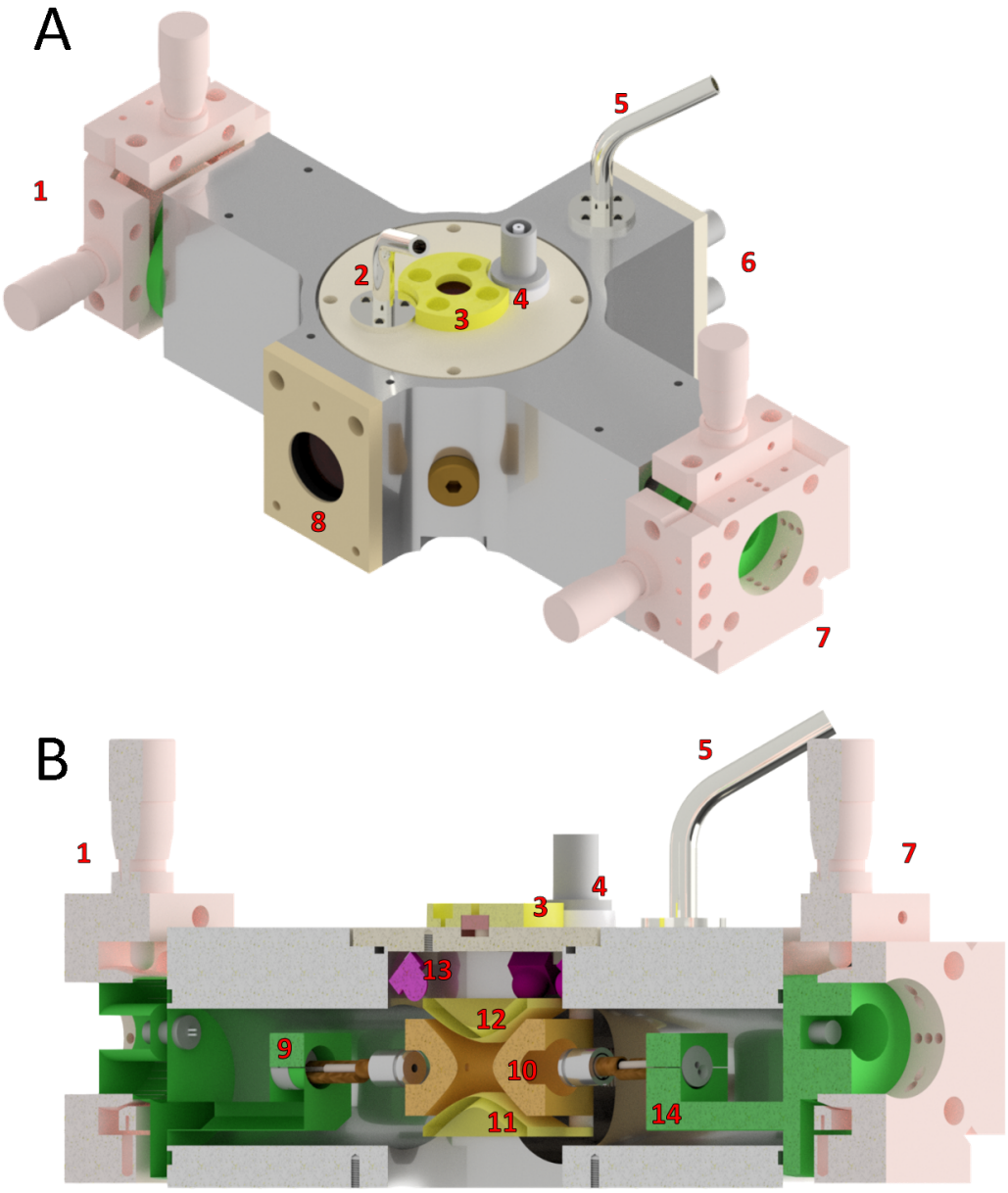

Fig. 2.11: Three-dimensional CAD drawing of the Paul trap construction for electrodynamic droplet levitation. A shows the work-piece including all components; B shows a profile of the construction. The components of the work-piece are numbered: 1 X-Y stage for positioning of the droplet generator, 2 air inlet for pressure regulation, 3 UV transmittable window, 4 connector for LED illumination, 5 port for barometer, 6 connectors for the trap's high-voltage AC signal, 7 X-Y stage for positioning of a second droplet generator, 8 window for a view of the levitated droplet, 9 mount for droplet generator, 10 ring-electrode of the Paul trap, 11 lower cap-electrode of the Paul trap, 12 upper cap-electrode of the Paul trap, 13 LED for droplet illumination, 14 mount for a second droplet generator.

trap. A BNC conductor (4) delivers the electric signal which energizes the LEDs. The airinlet (2) is connected to a needle valve to control the air flow. Pressure readout can be done by a manometer attached to opening (5). Figure 2.11B shows the inside of the construction. The droplet generators are located on their holders (9) and (14). The position of both holders can be controlled precisely by translation stages (1) and (7), both holders contain a conduct for the electric actuation of the droplet generators. The droplet generators target holes in the Paul trap's ring-electrode (10). An electrically shielded fixation of the ring-electrode is achieved by four hermetically sealed screws which push a ceramic pin to the electrode's wall. The cap-electrodes (11) and (12) are fastened by ceramic screws to the ring-electrode to ensure a stable geometry of the electrode system. The bottom of the construction is open to enable droplet release to the transfer stage.
This construction allows stable droplet levitation in vacuum of several mbar. However, the levitated sample droplet has to be transferred into high-vacuum of the MS instrument; in other words the Paul trap system has to be attached onto the LILBID-MS instrument.

Based on experience with the already existing conventional LILBID-MS instrument, a transfer stage to convey the droplet into high vacuum of the LILBID-MS instrument is required. This transfer from the levitation chamber at low vacuum of several mbar to high vacuum of 10^{-5} mbar of the inside of the MS instrument involves the use of a differential pumping stage. From the conventional LILBID instrument it is known how to achieve a droplet transfer: this requires a differential pressure stage encapsulated by two cones with an opening for droplet transition. The construction of this transfer stage can be seen in figure 2.12. Figure 2.12A shows the whole construction where the Paul trap (1) is adapted to the transfer stage; the two cones are numbered (2) and (3). The connections between the parts are hermetically sealed with sealing rings (represented by a black ring in figure 2.12B and by the notch in figure 2.12C). Thus, the pressure can be controlled separately in each of the components (levitation chamber, transfer stage and MS instrument) and adjusted in a differential way ranging from 10^{2} mbar to 10^{-2} mbar to 10^{-5} mbar, respectively. The pressure inside that chamber is controlled separately by a rotary vane pump attached to flange (4). The lower cone includes openings for attaching glass fibers to introduce a light barrier (5). Figure 2.12C shows this in more detail. When a droplet crosses the light barrier (laser light by a frequency doubled Nd:YAG laser at 532 nm) the light gets scattered. This scattered light can be captured by a second glass fiber

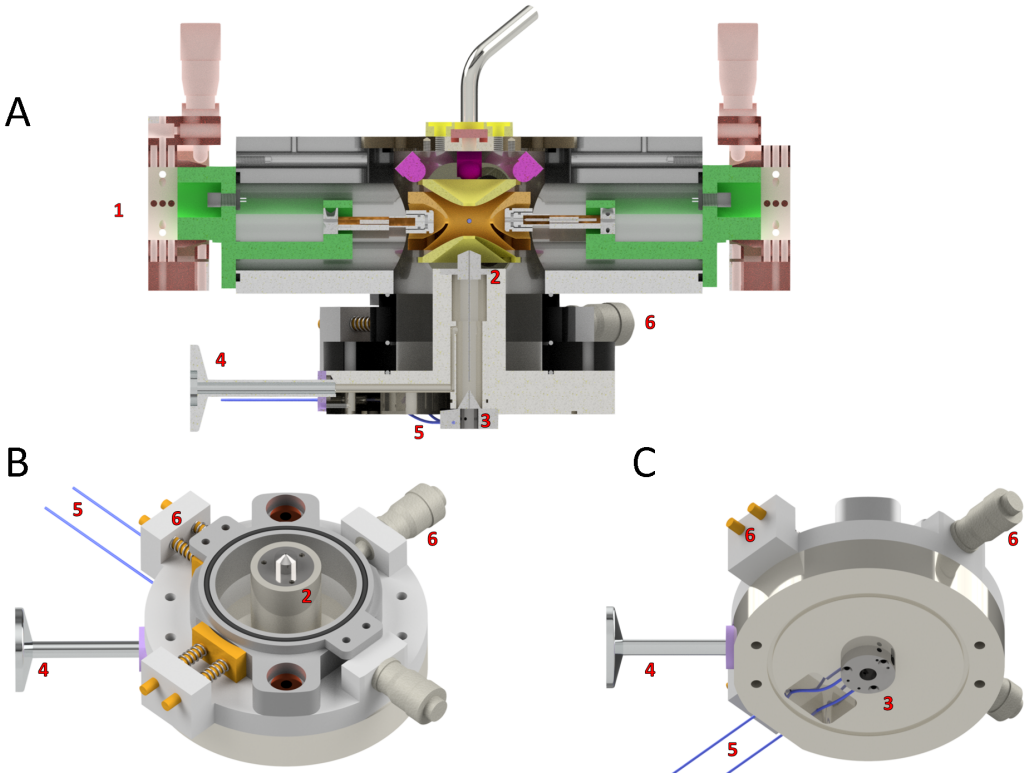

Fig. 2.12: CAD drawing of the stage which transfers the LILBID droplet from the Paul trap to the LILBID-MS instrument. A shows the cross section of the Paul trap (1) adopted to the transfer stage. The droplet has to cross two cones (2) and (3); the pressure in this area is controlled separately by adding a second vacuum pump to flange (4). The lower cone (3) deals as light cross to record the time the droplet is passing through it. Glass fibers (5) deal as conduct for shining laser light onto the crossing droplet and to record the scattered light. The position of the trap relative to the cone is controllable by a XY stage (6). B shows a CAD drawing of the transfer stage viewed from above and in C viewed from bottom up.

connected to a photo-multiplier tube. This enables to record the time-point when the droplet crosses the second cone and allows to adjust the exact time for laser irradiation and ion acceleration within the explosion chamber. Precise positioning of the levitated droplet towards the opening of the cone is necessary for an exact droplet transfer through the cone hole. This can be done via two micrometer stages (6). Each of them includes a micrometer screw (depicted with number (6) in figure 2.12B and C) which pushes the levitation chamber against a spring. Thereby the Paul trap and therewith the position of the levitated droplet can be adjusted precisely relative to the transfer stage. This allows to transfer the droplet from the levitation chamber through the differential pressure of the transfer stage to the high-vacuum of the explosion chamber.

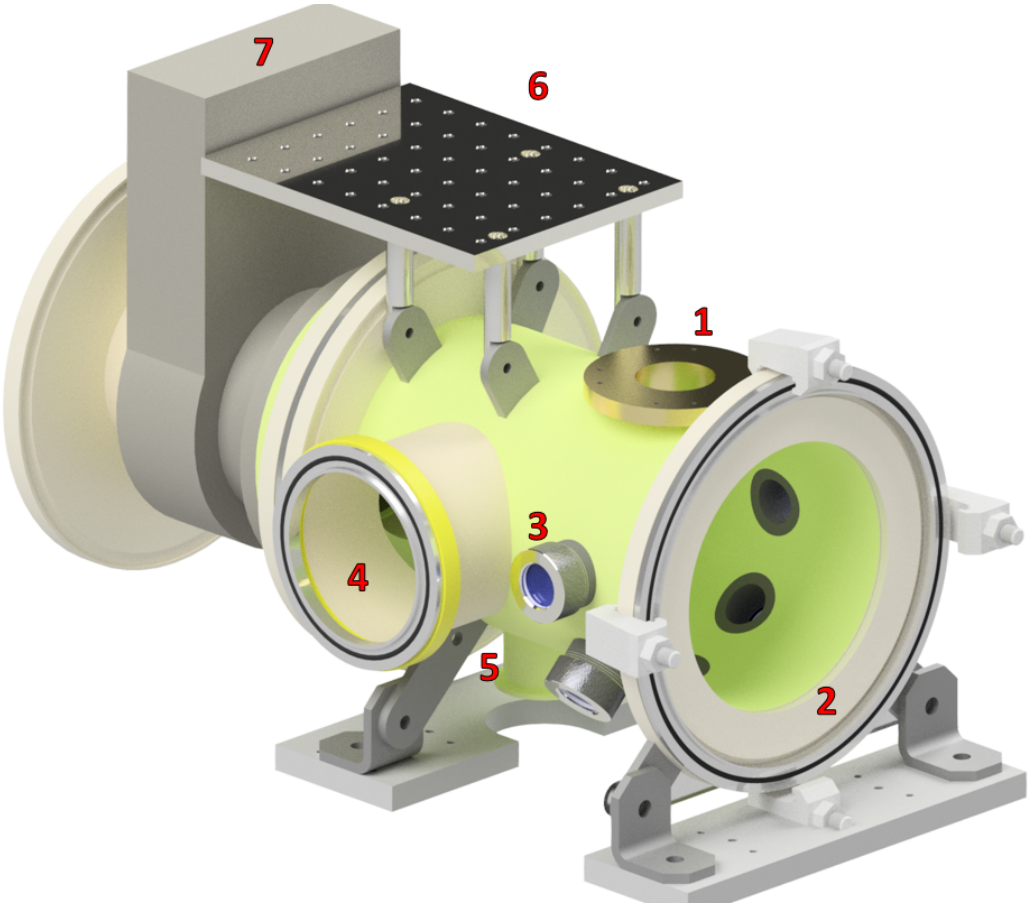

Fig. 2.13: Flight tube extension for adapting the Paul trap to the LILBID-MS instrument. 1 is the place for adapting the Paul trap, 2 is the conventional inlet for the droplet generators, 3 are multiple windows for droplet illumination and observation, 4 is a flange for planting a high-vacuum pump, 5 is a flange for planting a pressure gauge, 6 is an optical table, 7 is a shut-off valve. All elements are made of stainless steel except the optical table (6) which is made of aluminum.

Nevertheless, in contrast to the conventional LILBID-MS instrument where the droplet generator produces droplets with a horizontal trajectory, ejecting a droplet from the Paul trap to the MS instrument occurs vertically. This means the droplet will enter the desorption chamber of the LILBID instrument from top. Thus, the chamber for ion production via LILBID mechanism has to be redeveloped to adapt to the new situation. Figure 2.13 shows a 3D CAD drawing of this construction. It is made of stainless steel to guarantee solidity. The construction of the explosion chamber contains two separate droplet inlet positions: one for a vertical trajectory where the Paul trap with the transfer stage is placed (1) and another one for conventional horizontal droplet injection (2). The droplet injected on either one of these ways enters the electrode system for Wiley-McLaren like ion acceleration. From this

point on injecting the droplet on the conventional way horizontally (2) or from the Paul trap vertically (1) is possible. IR lasers are focused through one of the windows (3) onto the droplet between the Wiley-McLaren electrodes (window (a)). Visualization of the droplet explosion due to absorption of the IR laser light is also performed through the windows (3) (window (b)); one window can be used illuminate the LILBID process with light of a frequency-doubled Nd:YAG laser having a wavelength of 532 nm. A third window (c) in an angle of 90° or 135° to the window of visual illumination (b) is used to record pictures of the droplet during the LILBID process. By adding a turbo-pump to the flange (4) a high-vacuum is produced in the explosion chamber; read out of this pressure is done by adding a pressure gauge on flange (5). The optical table (6) can be used for mounting optics for the purpose of UV illumination of the levitated droplet in the Paul trap. This will finally allow to start a reaction via uncaging a PPG-containing compound which can than be subsequently time-resolved with LILBID-MS.

3 Summary and Outlook of Time-Resolved LILBID-MS

A precise understanding of biological processes can exclusively be achieved by a detailed analysis of its biochemical reactions. A detailed analysis involves the exact description of the reaction partners as well as of the reaction time of each process. Mass spectrometry is an analytical tool that can answer the first aspect precisely, nevertheless for several reasons the second remained elusive so far. This part of the dissertation describes the development of a system to extend LILBID-MS for time-resolved measurements to allow to analyze biological reactions holistically with native MS.

Since ion production via the LILBID mechanism involves small droplets, those droplets can be useds as small reaction vessels which can be manipulated contactless and on demand be directly injected into the mass spectrometer. For the purpose of contactless sample manipulation the LILBID droplet has to be levitated to ensure a precise reaction control. Levitation can be achieved electrodynamically in a Paul trap. The development of a system for TR-LILBID-MS includes several components: a framework to produce droplets with a precisely controllable amount of electric charges, an electrode system of a Paul trap and a generator for production of high-voltage AC signals to levitate macroscopic particles, an electrically isolated case including illumination of the levitated droplet as well as hermetical sealing and pressure control and a stage to transfer ejected droplets from the Paul trap to the MS instrument. Additionally the redesign of the high vacuum chamber where desorption takes place was necessary. The assembly of all of those components is shown in figure 3.1. The settings and parameters of each component have to be optimized in order to enable the most efficient realization of the individual purpose. This is essential in terms of a stable electrodynamic levitation of the droplet and thus involves a precise control of the charge of the droplet, the solvent condition, as well as a precise production of high-voltage AC electric fields. These settings were evaluated on a test-setup, separately from the main instrument. The derived parameters can be transferred to the work-piece constructed for extension of the LILBID-MS instrument.
This development enables the electrodynamic levitation of LILBID droplets

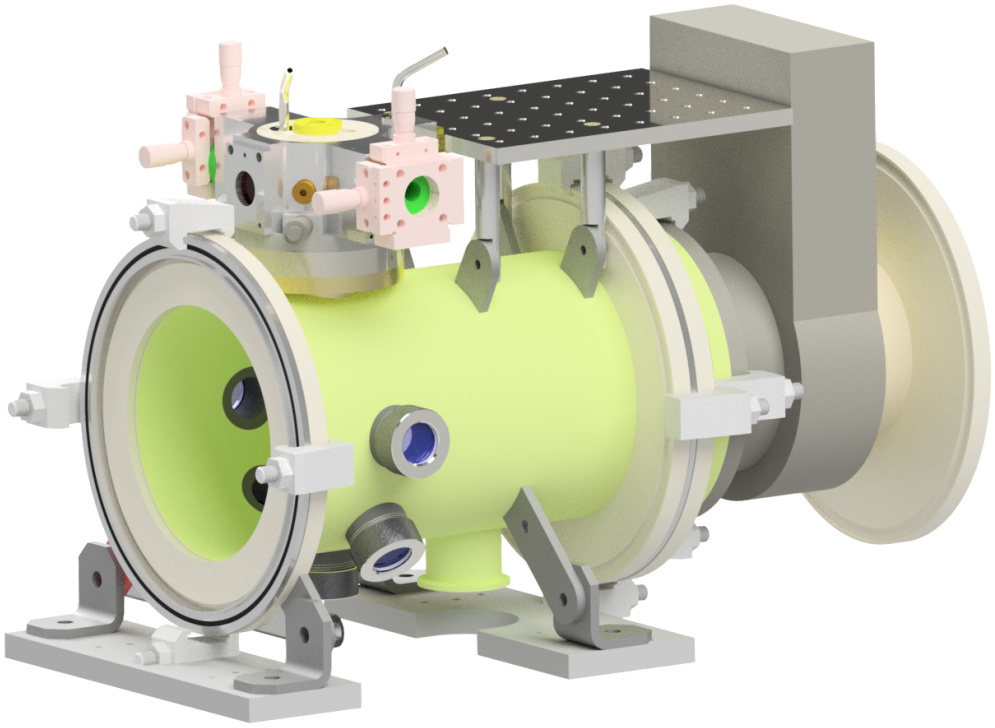

Fig. 3.1: CAD drawing of the whole TR-LILBID-MS setup. The Paul trap is placed on the transfer stage which adapts it to the flight-tube where the LILBID process is performed.

with a precision required for their transfer to the MS instrument. Nevertheless, the transfer of the droplet into the MS instrument is still unresolved. Attention has to be payed for the exact positioning of the trap (and thus the levitated droplet) towards the entrance of the transfer stage, as well as to adjust the time for droplet release in a specific phase of the droplet's Lissajous movement. The latter point is extremely sensitive since the vector of the droplet motion is highly dynamic resulting in different momenta of the released droplet.

Once the setup is running, a reaction can be started via two different ways inside the Paul-trap: either two droplets (each containing one reactant) are combined, which will start the reaction, or a single droplet contains both reactants, where one of them is a caged compound. Irradiation with an UV laser activates this component and uncaging occurs. A precise control of the time after reaction start on either one of the ways will enable high precision time-resolved MS experiments. For either method the limit of the time-resolution is affected by the transfer of the droplet from the levitation chamber to the MS instrument. Since the principle of this transfer is comparable to the con-

ventional LILBID-MS mechanism; this limit will be less than a millisecond. This allows to plan experiments to analyze sub-millisecond reactions.
An example for a time-dependent biological process is the oligomerization of the beta-amyloid peptide. The monomeric peptide can accumulate to oligomers and further to macroscopic fibrils which are related to Alzheimer's disease. Part two of this dissertation shows examples for time-resolved MS experiments of this process on the minute to hour time scale. Nevertheless, some reactions related to this process are too fast to be studied on this large time scale accessible with the conventional LILBID-MS instrument. The interaction of ligands to the beta-amyloid peptide as well as the exchange of monomeric subunits of an oligomer for example occur on much faster time scales and thus cannot be addressed so far. This shows the need for the herein described Paul trap setup. Addressing those processes enables to obtain knowledge about the physico-chemical properties allowing a deeper comprehension of the underlying molecular mechanisms.

Part II

Mass Spectrometric Analysis of Amyloids

4 Introduction to Amyloids and Related Diseases

The health of human beings has always been a great motivation for the development and progress of research in life sciences. In early days the recognition as well as the understanding of symptoms of a pathological phenotype had only been possible from an exterior view. This limits the insights people were able to obtain on the properties and on the cause of diseases. Thus, the development of scientific methods was an additional approach to improve understanding of the microscopic processes. New methods enabled the study of human physiology in more detail allowing to shed light on the onset of diseases even on a molecular level.
This was the case when Alois Alzheimer made the first observation about the mental disease *senile dementia*. He monitored the 51 year old patient Auguste Deter which eventuated in disorientation, paranoia, perplexity, forgetfulness, poverty of speech, etc. [95]. After 4.5 years of disease progression Auguste Deter died. The autopsy of her brain showed histological alterations, today known as plaques. Thereby, Alois Alzheimer primarily observed an amyloidogenic disease which was named after him: Alzheimer's Disease (AD). AD is a prime example for a class of umpteen amyloidogenic diseases. All of them share the histological finding of amyloid deposits in intra- or extracellular spaces. Other examples for these amyloidogenic diseases are plaques of α-synuclein known as Lewy Bodies related to Parkinsons Disease (PD), fibrils of the human islet amyloid precursor polypeptide (hIAPP) related to type 2 diabetes or poly-Q expanded huntingtin related to Huntington's Disease [96].

4.1 Parkinson's Disease and Alpha-Synuclein

The second part of this dissertation aims to analyze the oligomerization of amyloidogenic proteins which are related to several diseases. Analyzing the oligomerization process includes time-resolved measurements of the AOI

since the change of the kinetics of this oligomerization can be evidence for several parameters influencing amyloid behavior and thus might be a key for treating amyloidogenic diseases. PD is a typical example of an amyloidogenic disease which is characterized by the oligomerization of the protein α-synuclein (α-syn) to the evolvement of Lewy bodies (LB). These LB influence the dopamin metabolism in human brains and cause thereby Parkinson's Disease [97–103]. PD is a movement disorder affecting about 1 % of the population older than 60 years [104]. The symptoms are dramatic and motor- as well as non-motor-related [105]. Motor symptoms include tremor, slowed movement (bradykinesia) which ends up in a total loss of movement (akinesia), muscle stiffness as well as speech and writing changes. Additionally non-motor symptoms become noticeable by attacks of sweating, enhanced appetite, strong emotional acts as well as depression [106]. Since one of the hallmarks causing PD is the evolvement of LB, it is relevant to study the behavior of α-syn to understand the mechanisms of disease onset. It was for example shown that the ingredient of green tea epigallocatechin-3-gallate (EGCG) [99, 107], as well as dopamin have an influence on the structure of the α-syn protein which affects thereby the aggregation kinetics and pathway [101]. As part I of this thesis explains, mass spectrometry is a versatile tool to study the oligomerization of proteins. Nevertheless, with the state-of-the-art ionization technique ESI mainly dimers of α-syn are detected as oligomeric species in sufficient intensity. α-syn is a protein of 140 amino acids with a molecular weight of 14460 Da [101]. This, in combination with the hydrophobicity of oligomers [108] makes a detection with ESI-MS challenging. LILBID-MS on the other hand seems to be a more efficient method in detecting these oligomers [109]. Using this method enabled to observe hydrophobic non-covalent oligomers of high mass [35]. This opens the possibility to study the oligomerization of α-syn with mass spectrometry and to analyze the influence of different ligands on the oligomerization kinetic.

4.2 Alzheimer's Disease and Beta-Amyloid

Another amyloidogenic illness is Alzheimer's disease (AD). Especially AD has an extensive influence on the human population since it is the most common form of dementia [110–113]. 5.7 million U.S. Americans suffer from it, mainly people older than 65 years are affected (about 10 % of all Americans

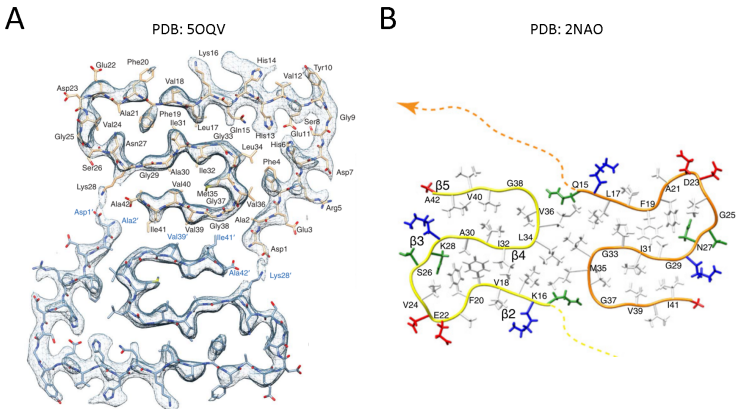

Fig. 4.1: The two most promising PDB structures of $A\beta_{42}$ oligomers, 5OQV by Gremer et al. and 2NAO by Wälti et al. Pictures were taken from [121] (A) and [119] (B).

of that age group). Just about 4 % of AD patients are younger than 65 years; these cases are named younger-onset AD [114]. The huge amount of patients in combination with demographic changes in human society make it necessary to understand the molecular cause for the onset of AD. Thereby the mechanism of the appearance of AD plaques is a valid question to be answered. AD plaques consist of fibrils of the beta-amyloid ($A\beta$) peptide and tangles of the tau protein [115]. Beta-amyloids are peptides consisting of 38-43 amino acids which result from degradation of the amyloid precursor protein (APP) by β- and γ-secretase [116].
Various kinds of beta-amyloid peptides exist but the most relevant ones in terms of AD are the species containing 40 ($A\beta_{40}$) and 42 amino acids ($A\beta_{42}$). 80 % of the beta-amyloid deposits in the brain are $A\beta_{40}$ [117]. Nevertheless, the ability to oligomerize and to evolve fibrils is substantially enhanced in the case of $A\beta_{42}$. It has a higher potential for neurotoxicity and shows faster aggregation kinetics than $A\beta_{40}$ [117]. Next to the differences in the ability and speed to oligomerize and also the differences in their structure [118, 119], both peptides have the possibility to evolve mixed oligomers and fibrils [120].

$A\beta$ peptides are natively unstructured but have the possibility to interact with each other in a partially folded state [122]. This amyloidogenic behavior of $A\beta$ peptides causes the evolvement of β-sheet rich fibrils which were found in 1906 by Alois Alzheimer as plaques. $A\beta$ plaques are about 10 nm in diameter [123], stainable by dyes like Congo red or Thioflavin T (ThT) [124, 125] and insoluble in water. In recent years it was found that the neurotoxic behavior of $A\beta_{42}$ is not caused by those macromolecular fibrillary plaques

but by the small soluble oligomers of $A\beta_{42}$ which are intermediate during the formation of fibrils [113, 116, 122, 126–129]. It was struggling to determine the structure of the monomeric subunits involved in the oligomers and fibrils [130], but recently solid-state NMR and cryo electron microscopy revealed an S-shaped conformation of the monomeric subunits within $A\beta_{42}$ fibrils consisting of two loops [119, 121, 131, 132] (compare figure 4.1). The first loop is kept together by hydrophobic interactions between the amino acids from Leu17 to Ile32 [119, 121, 131, 132] including the hydrophobic KLVFF region (amino acids 16-20). The second loop is stabilized via an ionic interaction between the C-terminal carboxy group of Ala42 and the positive charge of the side chain of Lys28 (compare figure 4.1B and 6.1A) [119, 131, 132].
Oligomerization of those monomeric S-shaped molecules is conceivable as parallel stacking of the $A\beta_{42}$ peptides with a monomer as base of the aggregates (monomer base: MB); but recently published structures of $A\beta_{42}$ fibrils show the base consisting of an $A\beta_{42}$ dimer (dimer base: DB) [119, 121, 131]. The monomers within the DB conformation of the fibril base are oriented in a ying-yang like way; however, the exact orientation of these monomers is still matter of debate. Two competitive arrangements are shown in figure 4.1A and B. Since DB arranged oligomers lead to fibrils, they are also the origin for so-called *on-pathway* aggregates which have neurotoxic properties. Next to this pathway there exists an *off-pathway* which terminates to amorphous aggregates rather than fibrils. Amorphous aggregates do not show neurotoxicity [113, 122, 133–137]. Looking for structural differences of $A\beta_{42}$ peptides undergoing *off-* and *on-pathway* oligomerization might be a key for the treatment of AD.

4.2.1 Treating Alzheimer's Disease

In most of the cases investigations to cure AD were by regulating the $A\beta$ content. This can be achieved either by moderating the function of the β- and γ-secretase or by increasing the clearance of $A\beta$. Few studies investigated a compound which affects the aggregation of $A\beta$ (this topic is reviewed in Folch et al. [111]). Nevertheless, screening the ability of molecules to inhibit the evolvement of small soluble *on-pathway* oligomers with neurotoxic properties might be a possible way to prevent, cure or at least moderate the severity of AD.

A physiological factor which influences the amount of $A\beta$ present in the central nervous system (CNS) and in the cerebrospinal fluid (CSF) is the

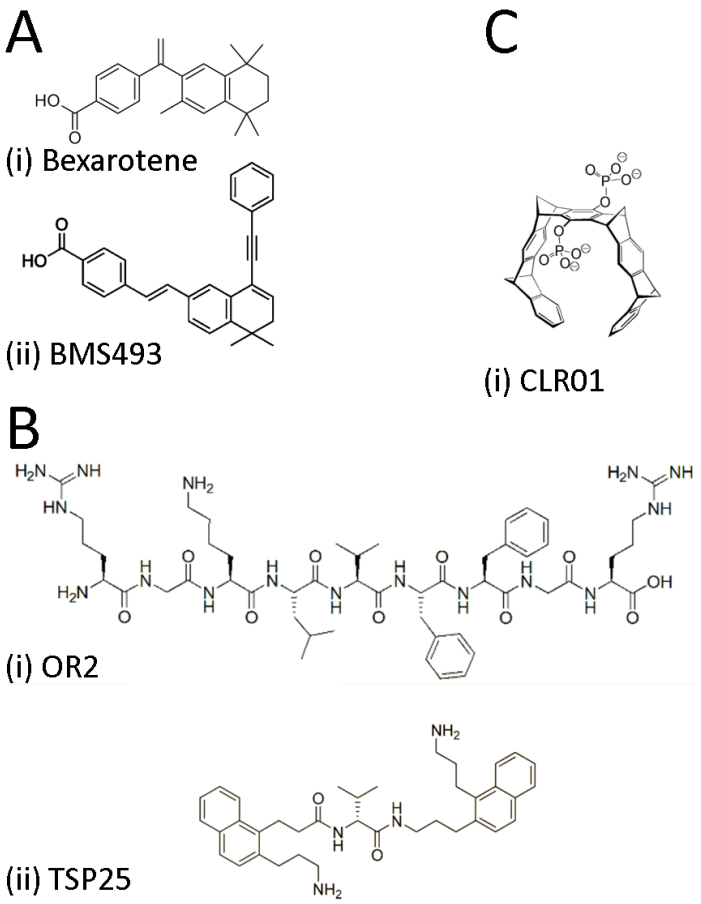

Fig. 4.2: Structures of molecules used in this dissertation to test for ability to inhibit $A\beta$ oligomerization. A: examples for RXR and RAR ligands: (i) bexarotene, (ii) BMS493; B: peptides and peptidomimetics: (i) OR2, (ii) TSP25; C: the molecular tweezer CLR01.

presence of the apolipoprotein E (apoE) [138]. apoE supports the evolvement of high-density lipoprotein (HDL) particles which promote degradation of soluble $A\beta$ in the CSF [139]. Thus mouse models with an increased amount of apoE agonists showed reduced $A\beta$ contents in the CSF as well as improved cognitive functions [140]. Therefore, it is important to study the influence of apoE agonists on $A\beta$ in terms of searching for a possible AD treatment. One example is the anti-cancer drug bexarotene (trade name: Targretin®), approved by the U.S. Food and Drug Administration (FDA) for cancer treatment (structure is shown in figure 4.2A(i)). Bexarotene is an apoE agonist of the class of retinoid X receptors ligands (RXR) which combines two effects. It clears the CSF from $A\beta$ [139, 141] and it influences its aggregation in terms of slowing the interaction of monomeric $A\beta$. This was shown for the evolvement of fibrils [142]. The aggregation of monomeric $A\beta$ is known as the primary nucleation. This nucleation process can ad-

ditionally be catalyzed by the existence of $A\beta$ fibrils. The surface of those fibrils can serve as catalyst and thus enhance the kinetics of oligomerization known as secondary nucleation [143]. The addition of bexarotene delayed fibril evolvement of about 2 h [142]. Experiments investigating the effect of bexarotene on the presence of neurotoxic oligomers are missing but simulations suggested no impact [142]. Nevertheless, this insight caused a more intensive search for molecules of the class of RXR and the related retinoid A receptor ligands (RAR) effectuating the evaluation of several molecules which additionally influence the secondary nucleation steps of $A\beta$ [144].

Peptides are another class of molecules which can influence the oligomerization of $A\beta$. The $A\beta$ ligand OR2 which mimics the hydrophobic KLVFF sequence of $A\beta$ (amino acids 16-20) and thus interferes with the hydrophobic part of $A\beta$ [137, 145–147] has the ability to inhibit the formation of fibrils [145] (structure is shown in figure 4.2B(i)). Furthermore it was shown that this molecule also has the ability to inhibit the formation of oligomers and even to reverse this oligomerization to rebuilt monomeric $A\beta$ from oligomers [4, 146]. Nevertheless, OR2 is a peptide which is susceptible to be degraded by peptidases. Thus it cannot be applied as a pharmaceutical drug. Furthermore, for executing a pharmacological function within the human brain a molecule has to cross the blood-brain barrier to reach areas relevant for AD. This is highly unfavored for big hydrophilic molecules [148]. Thus it is ineffective to test the ability of OR2 to prevent AD in vivo. Therefore, OR2 was used as base for development of a molecule with more suitable properties for in vivo applications. A molecule with D-amino acids instead of the naturally occurring L-isomers was synthesized which prevents degradation of the peptide by peptidases. To maintain the structural motive of the D-amino acid sequence the peptide has to have the reverse order FFVLK (known as retro-inverso). Several hydrophilic parts of this retro-inverso peptide were substituted by smaller hydrophobic parts to enhance to probability to cross the blood-brain barrier. This molecule (TSP25) still shows an inhibitory effect and additionally has positive effects on cell viability [4] (structure is shown in figure 4.2B(ii)).

A molecule which is tested to cross the blood-brain barrier and to tackle $A\beta$ oligomers in vivo is the molecular tweezer CLR01 [149]. The function of CLR01 is different from KLVFF peptides. Instead of interacting with the hydrophobic part of $A\beta$ it is an ionic molecular tweezer for lysine side chains [149–156]. It was introduced in 2005 by Fokkens et al. [157] and proven

that its interactions to lysine influences the $A\beta$ oligomerization and toxicity by Sinha et al. in 2011 [155]. CLR01 consists of a hydrophobic cavity with two phosphate moieties orthogonal to the expansion of this hydrophobic part (structure C(i) in figure 4.2). The hydrophobic cavity is designed to interact with the hydrophobic butyl chain of lysine and the negatively charged phosphate group with the positively charged ε-ammonium NH_3 of the lysine side chain. Thereby the positive charge of the lysine is shielded which can influence the behavior and structure and therewith the toxicity of $A\beta$ fibrils [155]. However, the interaction of CLR01 to lysine and thus to $A\beta$ has only a moderate affinity [157] resulting in high on- and off-rates of the ligand interaction [155].

4.2.2 Analyzing Amyloid Fibrillation

Investigation of the oligomerization and fibrillation of $A\beta$ is only feasible with in-vitro experiments. Therefore, it is necessary to produce the $A\beta$ peptide in a suitable amount, high purity and as a monomer. This can be achieved in two different ways: either synthetically by Fmoc solid-phase synthesis [158] or recombinantly by gene expression using *E. coli* bacteria [159], each followed by a disaggregation procedure. To compare different studies using either synthetically produced $A\beta$ ($A\beta_S$) or recombinantly expressed $A\beta$ ($A\beta_R$) it is important that both peptides behave similar. This was shown in terms of the morphology of the fibrils which were formed by both peptides [113].
Since $A\beta$ has a strong tendency to self-assemble into oligomers and fibrils it is necessary to reverse the aggregation which happened during the peptide preparation prior to investigating the $A\beta$ oligomerization. To achieve this, several methods were introduced starting with purified and lyophilized $A\beta$ peptide in a non-defined oligomeric state resulting in pure $A\beta$ monomers. $A\beta$ can be solvated either in a sodium hydroxide (NaOH) [160], hexafluoroisopropanol (HFIP) [161], or guanidinium hydrochloride (GuHCl) solution [159]; the latter two methods were used for the experiments in this thesis. Solvating $A\beta$ in either one of those solvents promotes monomerization of $A\beta$ oligomers. After incubation with the solutions it is necessary to remove the monomerizing agents. In terms of HFIP this can be achieved simply by evaporation of HFIP in a vacuum centrifuge (using a SpeedVac™). The use of GuHCl makes it necessary to clear the solution of guanidine by chromatography. Using a size exclusion chromatography (SEC) column on a fast protein liquid chromatography (FPLC) system (for example an Äkta™) enables to separate the monomerized $A\beta$ peptide from the guanidinium salt and to convey it into the desired buffer solution [159]. This strict preparation of the $A\beta$ peptide is necessary to start reliable studies on $A\beta$ oligomerization.

The evolvement of $A\beta$ fibrils was studied extensively in several publications; but experiments on the evolvement of neurotoxic oligomers are lacking. Furthermore, to the best of my knowledge, studies on the structural influences of ligands on $A\beta$ are missing and no clinical trials were performed until now. In spite of several in vitro experiments proving the ability of molecules inhibiting $A\beta$ fibrillation, none of them aims to achieve the important goal to understand the influence on the structure of $A\beta$ [126].
In most studies the oligomerization of $A\beta$ and the inhibition of this oligomer-

ization process was investigated by fluorescence spectroscopy using a ThT assay. ThT is a benzothiazole salt consisting of an extended π-system. This system is composed of two phenyl rings, which are connected with a rotational-flexible single bond. The presence of a hydrophobic interaction group that stabilizes the parallel conformation of the complete π-system enables ThT fluorescence [162]. $A\beta$ fibril evolvement includes β-sheet formation [163]. These can act as immobilizers for the C-C bond rotation within ThT leading to fluorescence [162]. Thus, detecting kinetics of the modification of the fluorescence of a ThT sample can be used to detect kinetics of $A\beta$ fibrillation. Nevertheless, the evolvement of ordered structures does only occur for oligomers larger than a tetramer [121]. However, the fluorescence intensity induced by these small oligomers is below the detection limit. Because of this, ThT assays enable to detect the evolvement of fibrils exclusively, while the detection of the appearance of the neurotoxic small oligomers is not possible [164]. Additionally, the discussion whether the presence of the ThT molecule does influence the aggregation behavior is still controversial [165–168]. ThT fluorescence requires a specific surface structure of amyloids and does not stain each of the different morphologies of amyloid aggregates. Next to the evolvement of fibrils also amorphous aggregates might occur, which are not detectable by ThT fluorescence [167, 169]. Thus, ThT is not a uniform tool to obtain a full picture of amyloid aggregation which might aggregate via different pathways into different morphologies. On the other hand, mass spectrometry (MS) is a very sensitive and specific tool which has the possibility to detect different oligomers of amyloids. Combined with ion-mobility spectrometry (IMS) this can be a useful technique to detect the peptide structure as well as changes of this structure induced by inhibitor molecules. These structural changes can be correlated to the kinetic of oligomerization on the level of neurotoxic oligomers. Thereby it is possible to study structural details which are key in choice of the evolvement between neurotoxic fibrillary aggregates or amorphous aggregates which do not show neurotoxicity.

4.2.3 The Analysis of Amyloids with Mass Spectrometry

The history of mass spectrometry studying native biomolecules like peptides or proteins and especially their non-covalent interactions is rather recent [5] (this topic is described in paragraph 1.1). Especially the analysis of amyloids

using MS is new. The focus of investigating amyloid behavior was at first on $A\beta$ [134, 170–175]. Since $A\beta_{40}$ is aggregating much slower than $A\beta_{42}$ a lot of these studies were conducted using $A\beta_{40}$ [134–136, 176]. As the kinetic as well as the structure of $A\beta_{40}$ differs from $A\beta_{42}$ the results found within those studies cannot directly be compared to the experiments shown herein. Nevertheless, due to the good resolution of the MS spectra in those studies it was possible to distinguish between different oligomers. By combining MS with IMS several conformations of $A\beta_{40}$ could shown to co-exist in the gas-phase [134]. This reveals that a combination of MS with IMS is necessary to obtain a specificity which is high enough to analyze certain $A\beta$ oligomers precisely [42, 135, 177, 178].
Analyzing $A\beta_{42}$ is not that straight forward, thus minor of the $A\beta$ studies and results are related to this disease relevant form of the peptide; majority of the studies focused on $A\beta_{40}$ and peptide fragments. However, it was for example possible to show that several IMS species of a certain m/z peak originate from different morphologies of a certain $A\beta_{42}$ oligomer [175]. This underlines that different structures of $A\beta_{42}$ do co-exist.
The specificity accessible with IMS-MS is key to study the interactions of ligands to $A\beta$ precisely [176, 179, 180]. However, the difficulties on MS investigations of $A\beta_{42}$ lead to nearly exclusive investigations of ligands with $A\beta_{40}$. Thereby it was shown that several ligands of different molecular classes influence the oligomerization of $A\beta_{40}$ [176] as well as the stability of a compact conformation [136]. To the best of my knowledge, the effect of ligands on the molecular structure of the $A\beta_{42}$ peptide never was studied. Furthermore, since ESI-MS is not able to detect time-dependent changes in the oligomerization (compare figure 5.7), it is not possible to follow the ligand's effect on the oligomerization kinetic.

Goal of the study of this dissertation is to reveal the effect of ligands on $A\beta_{42}$. Therefore the results of two ionization techniques are combined: LILBID-MS and ESI-IMS-MS. The former one enables to detect the oligomerization process of $A\beta$ in a time-dependent manner. This provides to analyze the effect of ligands on the aggregation kinetic of $A\beta$ for small disease relevant oligomers. Furthermore, these experiments can be refined by analyzing the effect of ligands on the peptide structure with ESI-IMS. By combining these results with published high resolution structures of $A\beta$ enables to conclude on a model for the molecular mechanism of oligomerization.

5 Investigating Amyloids with Mass Spectrometry

5.1 Insulin and α-synuclein: Proof of Principle

The power of MS analysis is generally the possibility to gain detailed knowledge of the oligomeric state even for heterogeneous samples. However, amyloids also present a challenge due to their probability to oligomerize. Different charge states of several oligomers overlap to the same m/z value which makes it difficult to distinguish the oligomers specifically. Furthermore, amyloid aggregates are polydisperse and might occur as a distribution of oligomer intensities which are high for the monomer and small oligomers but low for big oligomers [182]. On the contratry also specific oligomers are conceivable. Small oligomers can be building blocks on the oligomerization path to bigger oligomers [171]. To evaluate the possibility of the two ionization techniques ESI and LILBID to obtain accurate results, insulin is a great peptide for a proof of principle (details of the intrumental parameters and the participation of colleagues to the results are given in the supplementary information 9). Insulin is a protein with a mass of 5734 Da which has the property to aggregate. The aggregation of insulin can be tuned from a distribution of oligomers to a specific pathway by the addition of zinc [41]. Figure 5.1 shows MS spectra for 500 µM insulin in the absence and presence of 5-fold excess of zinc. Both ionization techniques (ESI in figure 5.1A and LILBID in figure 5.1B) do show different oligomeric species which are separated in m/z scale. For the spectra in the absence of zinc (upper black spectra in figure 5.1A and B) several oligomers can be detected; using ESI oligomers up to a trimer are visible. In case of LILBID even higher states of oligomers can be seen. Clearly insulin shows high intensity of oligomers up to the hexamer (and with smaller intensity even higher oligomers up to the 11-mer). Thus, LILBID seems to be a good tool to study high oligomeric species (compare figure 5.2). In figure 5.1 both oligomerization procedures (distribution of oligomers and specific oligomers) can be identified by the two ionization techniques. Figure 5.1A shows for ESI the appearance of specific

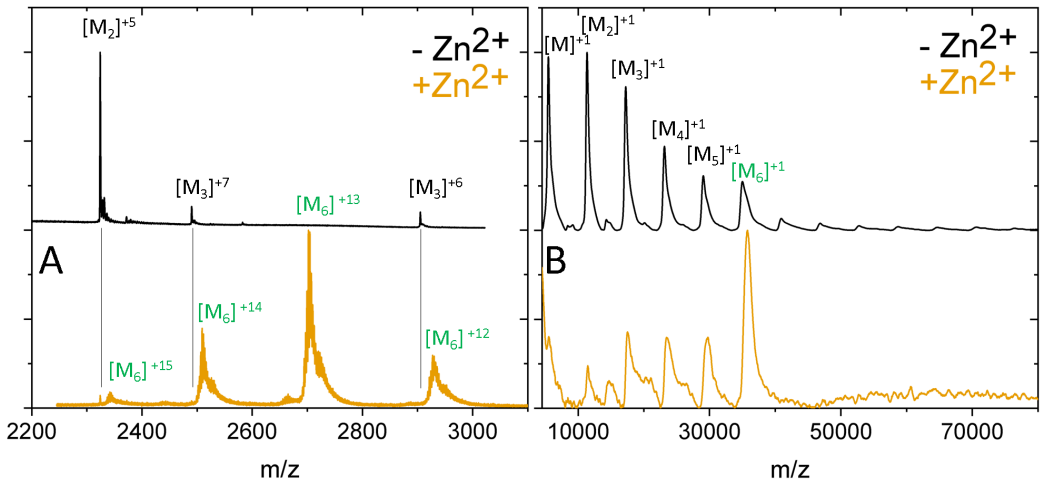

Fig. 5.1: Oligomerization of 500 μM insulin in absence and presence of 5-fold excess of zinc in 50 mM NH_4OAc. A shows ESI and B LILBID spectra. Acidic conditions (pH=4) lead to specific oligomers of insulin in presence of zinc which can be detected by both ionization techniques (modified from [181]).

hexamers after zinc addition (lower yellow spectrum). Monomer (not shown), dimer and trimer peaks, which were visible prior to zinc addition, decrease massively in intensity and the hexamer appears with several zinc ions interacting to the insulin oligomer. This behavior can be mirrored by LILBID in figure 5.1B. Due to the addition of zinc the intensity of all the oligomers decreases massively but the intensity of the hexamer is prominent. This proves that both ionization methods, ESI and LILBID, detect not just the presence of oligomers but also reflect the amyloid's ability to oligomerize. Both methods can pick up oligomerization via specific building blocks. Furthermore, the shift between the two states shown in figure 5.1 appears in LILBID promptly and already for lower zinc concentrations as by using ESI. This hints for LILBID being a more suitable technique to precisely determine specificities in the oligomerization behaviour of proteins.

High-mass oligomers bridge the gap between the monomeric and the fibrillary form of the amyloid protein which are the hallmarks of amyloidogenic diseases. These are impossible to detect with other methods (compare section 4.2.2). In terms of $A\beta$ amyloid fibrils start roughly in the range of >60 kDa or >100 kDa [183, 184] eventuating in oligomers as large as a 16-mer or 22-mer, respectively. Thus a gap-less detection of oligomers has to at least cover the range up to this mass and oligomer size. This requires the detection of high-mass oligomers. To evaluate the ability of both ionization techniques to detect those high-mass oligomers, α-synuclein was

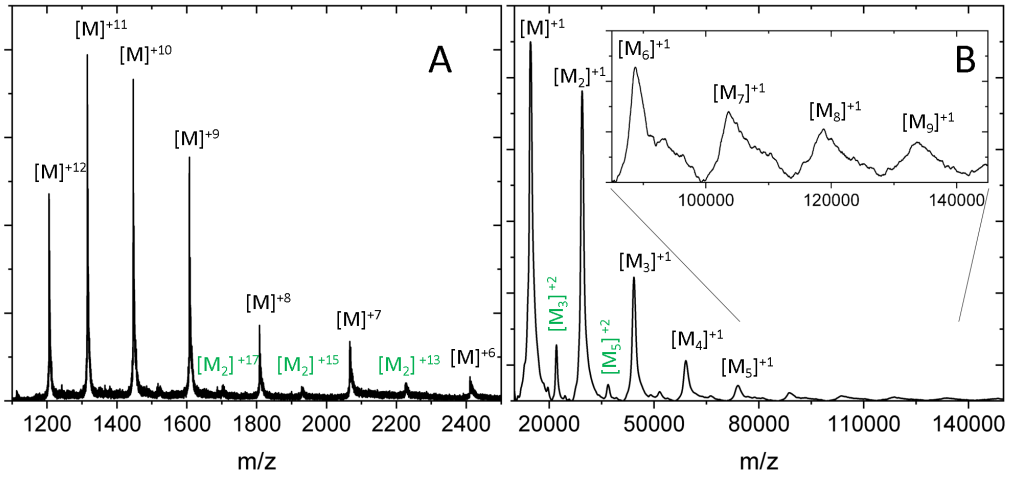

Fig. 5.2: Oligomerization of 25 μM α-synuclein in 50 mM NH_4OAc at pH 7.4. A shows an ESI spectrum of a sample incubated for 24 h at room temperature. The biggest oligomer visible is a dimer. B shows a measurement of the same sample using the LILBID ionization technique. Much higher oligomers until nonamer can be detected. (modified from [181]).

used as a model peptide. Section 4.1 explains that α-synuclein is an amyloidogenic peptide with a molecular weight of 14.6 kDa. Figure 5.2 shows spectra of this peptide recorded with the two ionization techniques ESI and LILBID. In figure 5.2A it can be seen that ESI produces various charge states of the monomer species [M]. The largest oligomer visible is a dimer [M_2], also in various charge states but just with a very small intensity near detection limit. This situation changes when the same sample is analyzed using LILBID ionization: almost exclusively singly charged oligomers are produced. High-mass oligomers can be detected up to the α-synuclein nonamer with a molecular weight of about 130 kDa. This α-synuclein analysis proves that LILBID is a good ionization technique to study oligomers of amyloidogenic proteins which bridge the gap between monomers and fibrils. The size of detectable non-covalent oligomers and thus also their mass and hydrophobicity is much higher in terms of LILBID ionization compared to ESI. Possible reasons for this finding include softness of the ionization technique which maintains non-covalent interactions as well as the detection of hydrophobic complexes. Both properties are preferable for analysis of amyloid oligomers.

Investigating amyloids implies to analyze the oligomerization of amyloidogenic proteins in a time-dependent manner. After the procedure of monomerization (compare section 4.2.2) amyloid proteins should be in a monomeric state showing none or at least just very few oligomers. Upon incubation amy-

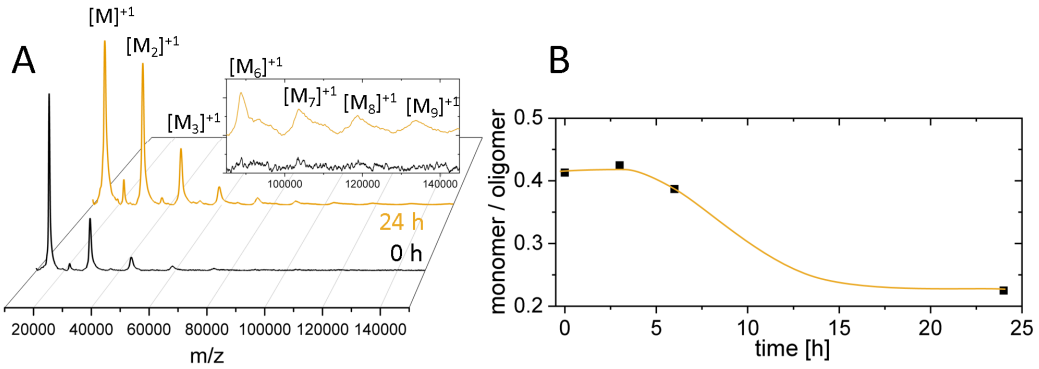

Fig. 5.3: Time-resolved oligomerization of 25 μM α-synuclein in 50 mM NH_4OAc at pH 7.4 incubated at room temperature. A shows LILBID spectra for the two distinct time points 0 and 24 h. Clearly an increase of oligomers is visible (the inset shows an enlargement of the signals appearing for high m/z values). B shows the time course of the M/O ratio over 24 h. The decreasing value shows the oligomerization process of α-synuclein (modified from [181]).

loidogenic proteins start to evolve into oligomers. A criterion for a suitable technique to study the amyloidogenic behavior of proteins is the ability to follow this oligomerization process. This property is not given by ESI (data not shown for α-synuclein, but depicted for $A\beta$ in figure 5.7). Even if this is a common fact the reason for this remains unknown. LILBID on the other hand monitors changes in size and amount of amyloid oligomers upon incubation. Figure 5.3A shows two LILBID spectra for α-synuclein either freshly solvated (lower black spectrum) or incubated for 24 h at a temperature of 22 °C (upper yellow spectrum). Clearly the amount of oligomers increases massively. This is for example visible for the trimer [M_3]: the intensity increases by a factor of 4 within 24 h. Furthermore, the average size of α-synuclein oligomers increases. The biggest oligomer at 0 h of incubation is a pentamer, after 24 h a nonamer. Nevertheless, α-synuclein is difficult to handle which resuts sometimes in non-appearance of the oligomerization. Thus, not all of the incubation experiments succesfully started the oligomerization process of α-synuclein.

A good measure to quantify the oligomerization state in a spectrum is the monomer-to-oligomer ratio (M/O), obtained by dividing the integral of the monomer by the weighted sum of the integrals of the oligomers:

$$M/O = \frac{I_1}{\sum n \cdot I_n} \tag{5.1}$$

where I is the integrated intensity of the respective peak and n is the size of the respective oligomer (e.g. $n = 4$ for the tetramer). Figure 5.3B shows the time-course of the M/O value over the incubation time of 24 h. Clearly the M/O value decreases within the incubation time which shows the oligomerization of α-synuclein. The M/O ratio decreases by a factor of roughly two to a value of 0.22 after 24 h of incubation.

This result proves the ability of LILBID-MS to detect time-resolved changes of the oligomerization of amyloidogenic proteins. It is possible to detect specific oligomeric sizes, high-mass oligomers as well as time-dependent changes of the oligomeric state. These proofs of principles make LILBID an optimal tool to study the evolvement of small oligomers of amyloidogenic proteins which is an important question to be answered in terms of understanding diseases related to those amyloids. In terms of analyzing oligomers of amyloids, LILBID seems to be a better choice than ESI due to the ability to detect high-mass oligomers and the possibility to detect time-resolved changes of those oligomers upon incubation. Also the evaluation of a distribution of oligomers or specific oligomers is more robust with LILBID since aggregation tendencies can be seen more reliably. LILBID can pick up specific oligomerization tendencies from the onset whereas higher concentrations are necessary for ESI. Nevertheless, an additional dimension can be added to the analysis of the mass of molecules by using IMS. Combining ESI-MS with IMS enables to add structural information of the studied molecules to the oligomerization kinetic.

5.2 Investigating Beta-Amyloid Oligomerization and Structure

Beta-amyloid oligomerization The possibility for investigating amyloids in terms of the evolvement of oligomers of amyloidogenic peptides as well as their structure with MS opens a good method to study the ”Alzheimer’s peptide” beta-amyloid. The possibility to detect time-resolved changes of the $A\beta$ oligomerization with LILBID is demonstrated in figure 5.4. Synthetically produced $A\beta_{42}$ was monomerized with the HFIP-method (compare section 4.2.2) and re-solubilised in 50 mM NH_4OAc at pH 7.4. The black spectrum in figure 5.4 shows a peak at roughly 4.5 kDa and just very tiny signals at 9 kDa and 13.5 kDa revealing $A\beta_{42}$ almost entirely in monomeric conformation just with few oligomers. Upon incubation at 22 °C $A\beta_{42}$ aggregates and oligomers from monomer up to the 11-mer can be seen, with decreasing intensities for higher oligomeric states. The blue spectrum shows respective oligomer peaks after 50 minutes and the yellow spectrum after 270 minutes

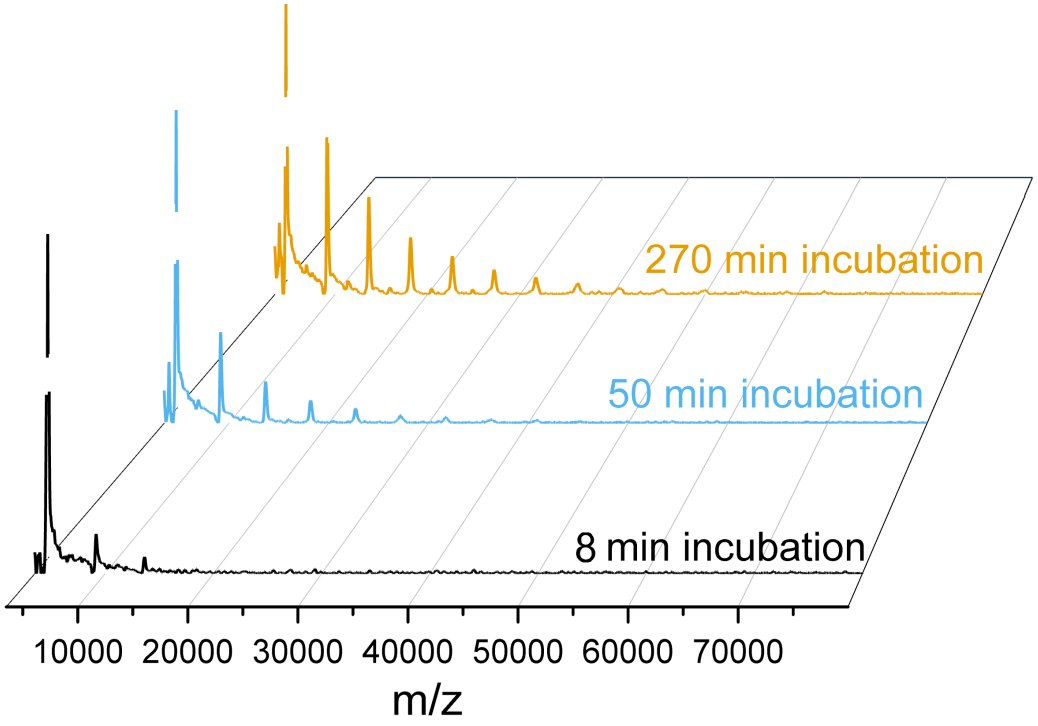

Fig. 5.4: Time-resolved oligomerization of 25 μM synthetic β-amyloid in 50 mM NH_4OAc at pH 7.4 incubated at 22 °C. The black spectrum shows the sample incubated for 8 min, the blue spectrum after 50 minutes, the yellow spectrum after incubation for 270 minutes. Clearly an increase in oligomers can be seen through to the 11-mer.

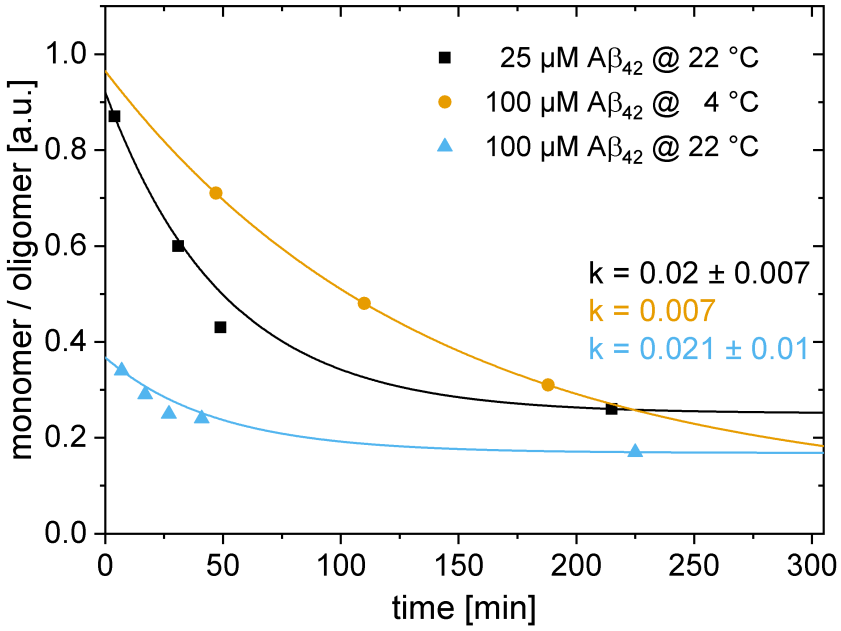

Fig. 5.5: Time-course of monomer-to-oligomer values for different $A\beta_S$ concentrations and incubation temperatures. A dependence of the oligomerization kinetics on the incubation temperature can be seen. The k-values of the exponential fit of the form $M/O = A \cdot e^{-kt} + y_0$ are indicated.

of incubation. No specific oligomers are evident, which would appear in higher intensities (compare figure 5.1). Detecting time-resolved changes in the appearance of $A\beta_{42}$ oligomers opens the possibility to study influencing factors on this aggregation.

A factor which is well known to influence the aggregation of amyloids is the incubation temperature. Higher incubation temperatures should lead to an increased oligomerization kinetic [185]. To verify that LILBID-MS is feasible to detect relevant changes in the oligomerization kinetic, $A\beta_{42}$ was incubated at different temperatures. Figure 5.5 demonstrates this for the appearance of $A\beta_{42}$ oligomers in terms of the M/O ratio (equation 9.1). Clearly the temperature does influence the kinetic of amyloid oligomerization. 100 µM $A\beta_{42}$ is aggregating much faster when incubated at 22 °C (blue triangles) as at 4 °C (yellow circles). The k value of the exponential fit of the form $M/O = A \cdot e^{-kt} + y_0$ is significantly lower when incubating $A\beta$ at 4 °C compared to an incubation temperature of 22 °C. The difference is much higher than the error of the fit. Additionally, both measurements at 22 °C (black squares and blue triangles) reveal the same rate constant, regardless of the

$A\beta$ concentration. However, this is unexpected since a higher concentration should also lead to increased aggregation kinetics. Nevertheless, the equilibrium of $A\beta$ aggregation is lower for concentrations of 100 µM as it is for 25 µM. The supplementary figure 9.1 shows the reproducibility of kinetic constant determination. The M/O values for different batches of the $A\beta$ peptide incubated at the same temperature reveal the same rate constant as for the experiment shown here. This underlines the reliability of the determination of aggregation kinetics by LILBID-MS. Still, the speed of the aggregation seems to be unaffected by the concentration of $A\beta$. Nevertheless, the supplementary figure 9.1 reveals that the equilibrium of $A\beta$ aggregation has lower M/O values for higher $A\beta$ concentrations. However, the error of the y_0 value, which determines the offset of the exponential decrease and therewith the equilibrium of $A\beta$ oligomerization, is high. Thus it is not possible to make a reliable statement about the steady state; this characteristic has to be manifested in a more detailed study.
In some of the cases $A\beta$ is already aggregated at the start of the incubation experiment. This is also shown in the supplementary figure 9.1 (red hexagons). Nevertheless, those cases are clearly evident and were excluded from all the experiments on evaluating changes in the aggregation kinetic shown later on.
This experiment proves the feasibility to use LILBID-MS to determine factors that can influence the aggregation kinetics of synthetic $A\beta_{42}$.

Nevertheless, native production of $A\beta$ is via recombinant gene expression. These peptides might differ in the oligomerization kinetic from synthetic $A\beta$. Thus, evaluation of the feasibility to analyze the oligomerization of recombinant peptides is necessary. Figure 5.6 shows ESI-IM spectra for fresh solvated and LILBID-MS spectra for incubated $A\beta$, each for 50 µM HFIP-treated synthetic $A\beta_S$ (lower lane) and 25 µM recombinant $A\beta_R$ (upper lane). Both peptides behave comparably. The 5-times charged $A\beta$ dimer at $m/z = 1806$ was analyzed with ESI-IMS for intensity and specificity reasons (compare the discussion for figure 5.8). Figure 5.6A shows that the molecular structure detected with IMS is identical. Three conformers are detected with a perfect coincidence of the drift time for both molecules. Two signals represent native solution structures. CIU experiments (compare figure 5.11A) reveal that the two peaks having the lowest drift time are coexisting structures which are native and shall be contained in solution phase. The third peak having the highest drift time arises from the unfolding of the first peak with the lowest drift time; in other words this peak is not a solution structure

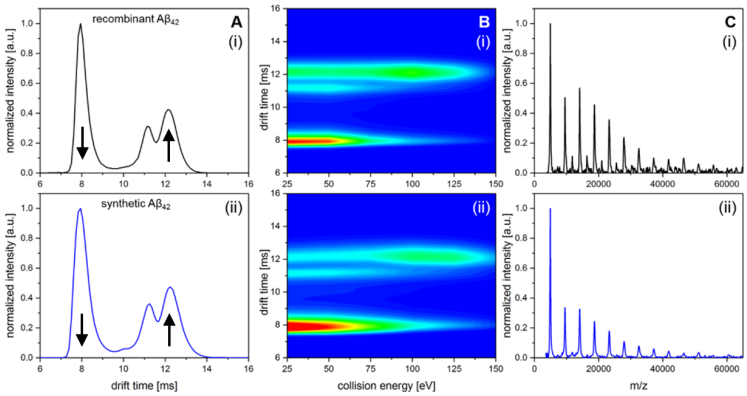

Fig. 5.6: Comparing the oligomerization of synthetic and recombinant β-amyloid in 50 mM NH_4OAc at pH 7.4 incubated at room temperature. The upper lane shows data for recombinant $A\beta_R$ whereas the lower lane data of synthetic $A\beta_S$ are depicted. A shows the arrival time distribution (ATD) of the 5-times charged $A\beta$ dimer at $m/z = 1806$, B shows the stability towards CIU and CID in a collision experiment as heatmap, C depicts a typical LILBID-MS spectrum of an aggregated $A\beta$ sample. Reproduced with permission from Journal of American Chemical Society, submitted for publication. Unpublished work copyright 2019 American Chemical Society. [186]

but appears upon unfolding in the gas phase. This is indicated by arrows. Upon increase of collision energy the intensity of the first peak decreases which correlates with an intensity increase of the third peak. Figure 5.6B shows that the structure of both $A\beta$ peptides behaves the same upon collision to inert gas molecules in a collision induced unfolding (CIU) experiment (for a detailed discussion of this effect compare description for figure 5.9). The conformer with the lowest drift time at 8 ms unfolds at energies of about 85 eV into the conformer with the highest drift time at 12 ms. The species with a drift-time of 11 ms dissociates without unfolding. This shows that the procedure of peptide-production has no influence on the structure and its stability. Nevertheless, the appearance of oligomers of recombinant $A\beta$ does differ from that of synthetic $A\beta$. LILBID-MS spectra in figure 5.6C show that the amount of oligomers for synthetic and recombinant $A\beta$ is different. Even if the concentration of $A\beta_S$ is lower, $A\beta_R$ aggregates are more intense. The recombinant peptide in C(i) shows more oligomers in higher intensity than the synthetic peptide in C(ii). Also the kinetic of the aggregation process differs for both peptides. The supplementary figure 9.2 shows that aggregation kinetic and equilibrium state are depending on the procedure for peptide production as well as on the procedure for monomerization.

This shows that the peptides produced with both methods behave similar;

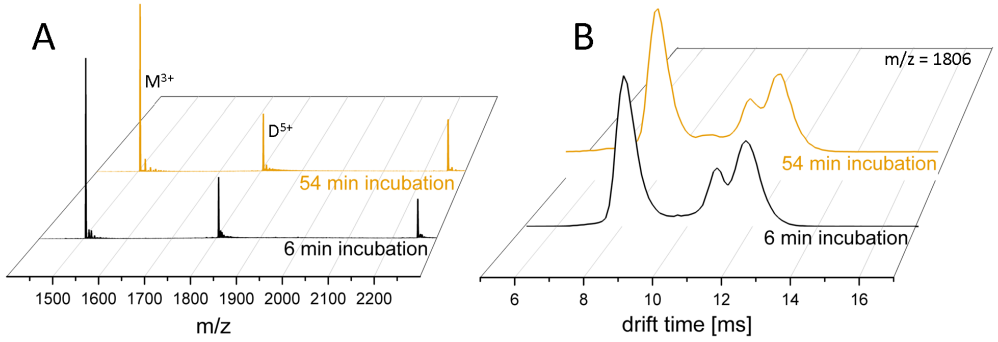

Fig. 5.7: Time-resolved oligomerization of 50 μM synthetic β-amyloid in 50 mM NH_4OAc at pH 7.4 incubated at room temperature. A shows two ESI mass spectra at time-points 6 min and 54 min of incubation. Signals for monomer and dimer can be detected independent on the incubation time. B shows IMS spectra of the 5-times charged $A\beta$ dimer peak at $m/z = 1806$ of the same sample and the same incubation times as in A.

thus, the results received for synthetic and recombinant $A\beta$ are comparable. Nevertheless, these results also demonstrate that it is essential to apply control experiments at standard conditions for studying aggregation kinetic influencing factors. For those control experiments it is absolutely necessary to use the same experimental details (for example incubation temperature, concentration, pH, ionic strength, peptide production procedure, monomerization procedure, instrumental settings). All of those conditions do influence the aggregation of $A\beta$ and its detection and have to be taken into account when planning an experiment to analyze $A\beta$ oligomerization.

This also holds true for studying the structure of $A\beta$ with ESI-IMS. As seen for the analysis of α-synuclein (chapter 5.1) in contrast to LILBID, ESI is suited to measure MS spectra with high resolution but time-resolved changes cannot be captured. Figure 5.7 shows that this is also the case for $A\beta$. In A two spectra of the same $A\beta$ sample are shown. The different peaks are assigned by isotopic pattern. Neither the oligomers nor their intensity change upon incubation from 5 to 55 minutes, as opposed for LILBID-MS (and also not for further incubation times for several days, data not shown). In figure 5.7B the IMS signals of the 5-times charged dimer peak at $m/z = 1806$ are shown for both respective spectra in A. Additionally to the MS signal, also the IMS signals do not change upon incubation, indicating no detection of structural changes. This behavior is not due to a sample which fails to aggregate (as the red hexagons in figure 9.1) but was found for all experiments. However, ESI-IMS is a suitable tool to study the structure of $A\beta$ and structural changes.

Beta-amyloid structure Analyzing the structure of amyloids is relatively complex, since oligomers are polymorph and transient on the way to fibrils [122]. Therefore it is relevant to use techniques which have the ability to study structures of isolated species; exactly this is the strength of the combination of MS with IMS. Using MS it is possible to separate different species resulting in isolated oligomer signals which can be studied specifically. Figure 5.8A shows a typical ESI-MS spectrum of $A\beta$ with peaks of several oligomer orders in several charge states. All of those peaks can be assigned by isotopic pattern.

However, every species appears with a charge distribution in ESI mass spectra. The oligomerization of peptides leads to species with mass-multiples of the monomer. This results in many cases in an overlap of signals of different oligomers in different charge states to the same m/z signal; this is for example shown in the inset (ii) in figure 5.8A. This overlap of several oligomers with different charge states occurs for all of the assigned peaks except the 5-times charged dimer at $m/z = 1806$ (figure 5.8A(i) and B). Since this peak appears also with high intensity, IMS experiments on that species are most promising to determine the structure of $A\beta$ oligomers. IM signals on that

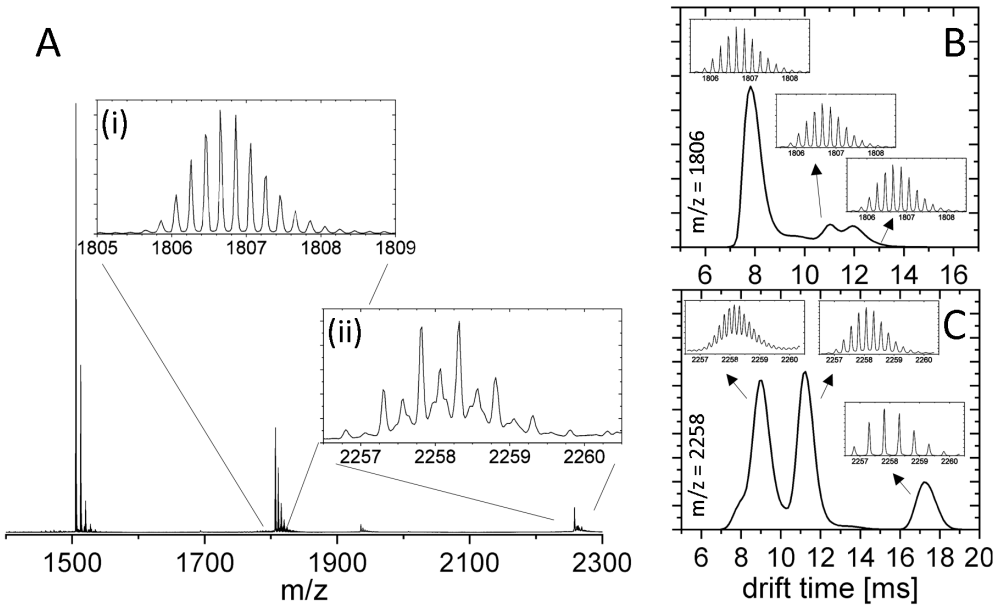

Fig. 5.8: ESI-IMS-MS spectrum of 50 μM synthetic β-amyloid in 50 mM NH_4OAc at pH 7.4 before incubation. A shows an ESI spectrum of $A\beta$. The insets show enlargements of the peaks at $m/z = 1806$ (i) and $m/z = 2258$ (ii). In B the result of an IMS experiment on the 5-times charged dimer peak at $m/z = 1806$ is shown. The insets show the isotopic pattern of the contributing m/z signal for all the IM species. C depicts the same analysis for the peak at $m/z = 2258$.

peak (in figure 5.8B) show three different species which are caused by different geometries of that dimer species. Since the m/z distance of isotope signals proves the charge state of a species, the insets in figure 5.8B prove that only 5-times charged molecules contribute to that peak, proving the existence of three different conformers of $A\beta$ dimer. However, also differently charged oligomers can overlap to the same m/z peak, as in the case of $m/z = 2258$. This can also be captured with the peak's isotopic pattern (figure 5.8C). Three isotopic distributions reveal the co-existence of differently charged molecules and thus of different oligomers. The 2-times charged monomer, the 4-times charged dimer as well as the 6-times charged trimer contribute to the appearance of the peak at $m/z = 2258$. This overlap makes it difficult to separate the different oligomeric species which substantiates why a specific structure analysis is not possible on all of the peaks.
Due to the combination of signals of various oligomers overlapping at the same m/z ratios, detailed analysis of a specific oligomer would be impossible with IMS alone. A proper analysis of $A\beta$ oligomers is just possible by combining MS with IMS. With IMS and a sufficient MS resolution to detect the isotopic pattern of MS signals enables to separate distinct conformers and distinct oligomers. The identification of those two different cases is necessary to calculate collision-cross-sections (CCS) for all the oligomers. Based on the specificity of the signal of the dimer, the peak at $m/z = 1806$ is most promising for experiments to investigate structural changes. However, similar results are found for other oligomeric species.

Figure 5.9A shows a 2D driftscope of the ESI-IMS-MS analysis of $A\beta$. Many peaks can be detected, which also overlap to single m/z peaks and thus are just visible by a combination of MS with IMS. Nearly all of the assigned oligomers are identified by isotopic pattern with a nonamer as the biggest oligomer detected in sufficient signal-to-noise ratio. The insets in figure 5.9A show the purity if the 5-times charged dimer peak at $m/z = 1806$ and the overlap of several charge states of different species to the peak at $m/z = 2258$.
Figure 5.9B shows a comparison of the solution phase structures of the IMS experiment to linear and isotropic fits (solid and dashed lines, respectively). The peak with the highest drift time of the 5-times charged dimer species is an gas-phase unfolding product of the smaller solution-phase structure (compare figure 5.11A). Thus this species is excluded from this analysis. Two series of oligomer structures cause the two coexisting solution phase CCS values (red and blue). For both series CCS increase upon

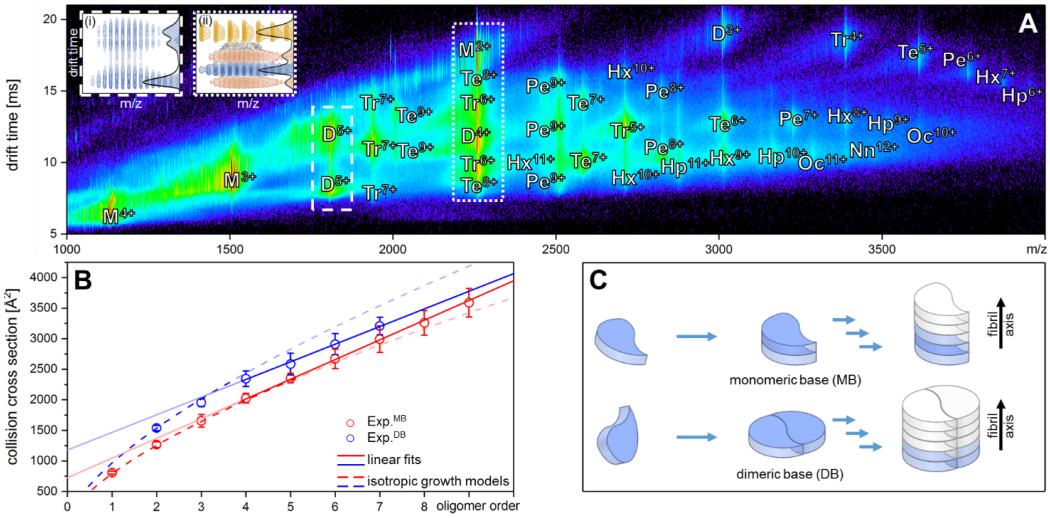

Fig. 5.9: ESI-IMS-MS analysis of 50 μM synthetic β-amyloid in 50 mM NH_4OAc at pH 7.4 before incubation. A shows a 2D driftscope of the MS spectrum on X-axis and the respective IMS signals on the Y-axis as a heat-map in logarithmic intensity (blue as a low and red as a high intensity). Several charge states of each species in various conformations can be detected. Nearly all assigned peaks are identified by isotopic pattern. The insets depict this for two different cases: (i) shows the IMS signal of 5-times charged dimer where just a single species can be detected, (ii) shows an overlap of monomer, dimer and trimer within a single m/z peak. B shows CCS values of the solution phase species of different oligomers. Those values are compared to either isotropic (dashed lines) or linear growth (solid lines) models [187]. C illustrates a model for the oligomerization process of MB (upper process) and DB (lower process) oligomers. Reproduced with permission from Journal of American Chemical Society, submitted for publication. Unpublished work copyright 2019 American Chemical Society. [186]

oligomer growth behaves differently whether the oligomers are smaller or bigger than a tetramer. Growth of oligomers can occur either spherically with an isotropic size increase or fibril-like with a linear size increase. For oligomers smaller than a tetramer the increase in CCS can be described by an isotropic fit which renders a spherical growing structure. From tetramer on both curves can be described perfectly by a linear growth function. Thus, the tetramer seems to be a hallmark for the spherical structure of $A\beta$ oligomers and linear fibrils. The hallmark character of the tetramer species was also suggested by Gremer et al. in terms of the evolvement of ordered fibrillar structures [121]. A more detailed analysis is possible when the IMS structures are compared to PDB structures. Section 4.2 explains that the structure of $A\beta$ fibrils consists of $A\beta$ dimers which are base for fibrillar stacking (dimer base: DB). Two competitive arrangements of fibrils which consist

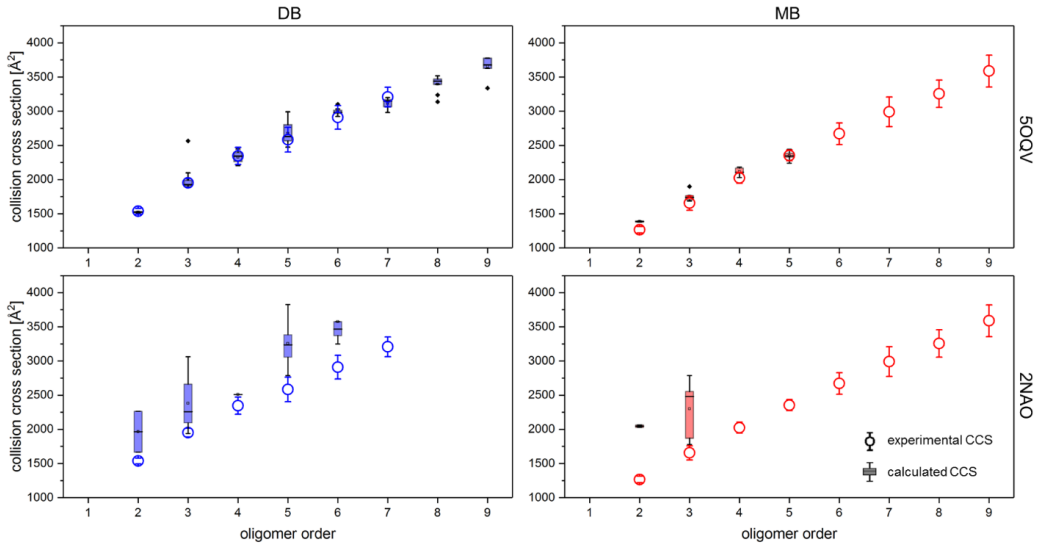

Fig. 5.10: Correlating experimentally determined CCS values (circles) to the CCS of the molecular models 5OQV and 2NAO (box plots). Cuts of different sizes of MB and DB arranged oligomers were MD simulated to resemble the experimental environment of a charged molecule in vacuum. Reproduced with permission from Journal of American Chemical Society, submitted for publication. Unpublished work copyright 2019 American Chemical Society. [186]

of S-shaped dimers were published recently: PDB structure 5OQV shows an $A\beta$ fibril detected with cryo-EM by Gremer et al. [121], PDB structure 2NAO was found with solid-state NMR experiments by Wälti et al. [119]. Both entries do have an $A\beta$ dimer as base for the fibril (dimer base: DB) but different arrangements. Nevertheless, $A\beta$ oligomers might also stack via a monomer as base (monomer base: MB). Thus, both PDB structures deal as base for generation of MB and DB oligomers. Since those structures were measured for uncharged molecules in a solid environment, they are not comparable to the situation during IMS measurements, since IMS shows structures of charged molecules in gas-phase. To correct for this difference, Rene Zangl and Jan Hoffmann sent the substructures to molecular-dynamic (MD) simulations which enables to transfer the PDB structures to the situation of a charged molecule in vacuum. This allows to compare experimentally determined CCS values by IMS to these molecular models.

Several charge states per oligomer were send to MD simulations. Figure 5.10 depicts the comparison of the two sets of CCS values with theoretically obtained CCS for substructures of PDB 5OQV and 2NAO in MB and DB conformation. The experimental values resembling a native state with a low drift time (red circles in figure 5.9) were compared to MB conformed oligomers

and the native state with higher drift times (blue circles in figure 5.9) to the DB conformation. The upper parts of figure 5.10 reveal a perfect agreement of the experimental values to the simulations of the model 5OQV. The different oligomers of both arrangements (MB and DB) match the experimental findings for all oligomers (monomer to nonamer for DB and monomer to pentamer for MB) perfectly. On the other hand, simulations of the substructures based on the ssNMR structure 2NAO (lower parts of figure 5.10) deviate significantly from our experimental data. Different charge states lead to various CCS; however, non of the values fits the experimentally determined CCS value. Thus, 5OQV describes the experimental findings best and was used for further interpretation of the results.
These simulations support the interpretation that the solution phase IMS peak with the lowest drift time shows an oligomer in MB conformation, whereas the higher drift time of the solution conformations is caused by DB arranged oligomers. The occurrence of both proves that these arrangements coexist in solution side by side.

Due to a clear and intense signal of a single oligomeric species which does not overlap with other charge states of other oligomers, the 5-times charged dimer peak (D^{5+}) at $m/z = 1806$ was used for a more detailed analysis. D^{5+} shows three species in IMS experiments which can be assigned to the coexisting native solution-phase structures MB and DB, as well as an additional peak. By collisional activation of the natively folded species it is possible to unfold the structures whereby the IM peak shifts to a higher drift time. Figure 5.11A shows that this is the case for the MB solution phase structure at a drift time of 8 ms. Upon increase of collision energy the intensity of that species decreases in favor of an increase of the intensity of the biggest drift time species at 12 ms. This shows the unfolding of the MB solution-phase structure to the gas-phase structure at 12 ms. The overall intensity of the signal decreases continuously as collision induced dissociation (CID) is a competing effect of CIU; in other words the non-covalent dimer dissociates to monomer species upon collision leading to a decrease of the dimer signal. Interestingly, unfolding of the MB arranged dimer can be detected whereas the DB structure does not unfold before dissociation of the dimer. However, higher charge states lead also to unfolding of the DB species. In figure 5.11B driftscope plots of D^{5+} (i) and the 7-times charged trimer peak (Tr^{7+}) (ii) are shown. D^{5+} in B(i) only shows three IM species, but already for the Tr^{7+} in B(ii) an additional species can be detected whose intensity increase correlates to the intensity decrease of the native DB conformation (another

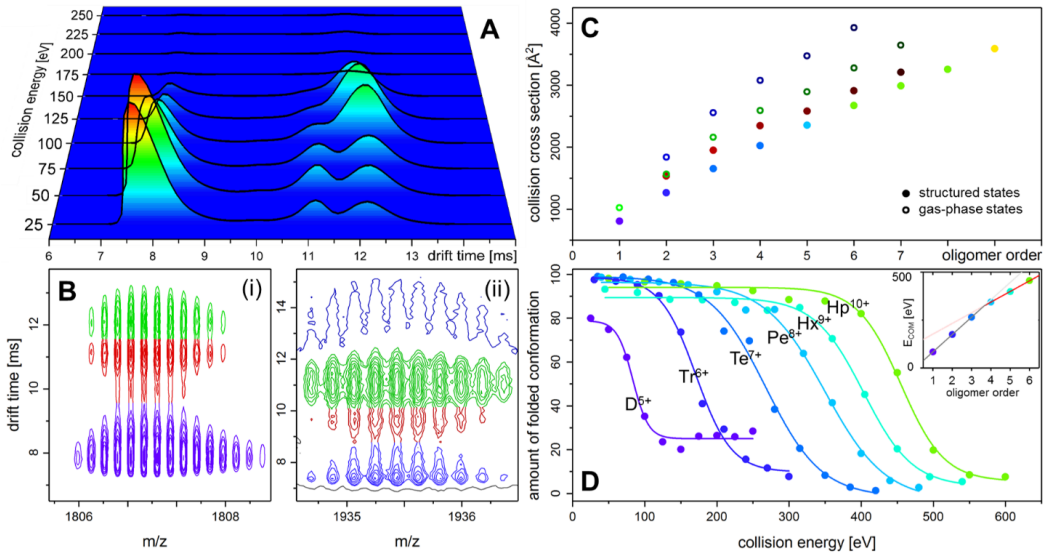

Fig. 5.11: CIU experiment of 50 μM synthetic β-amyloid in 50 mM NH_4OAc at pH 7.4 before incubation. A shows a 3D plot of ion-mobility spectra recorded for different collision energies. B shows a zoom of a driftscope plot for two different species; (i) shows the peak of the 5-times charged dimer, (ii) shows the peak of the 7-times charged trimer. The color-code of the peaks is the same as in C where a complete picture of the CCS values of all the peaks is shown. D shows the result of CIU experiments on the different oligomer species corrected for their charge state. The inset in D shows the medium energies of the unfolding process of each of the oligomers. The gray and red line show a fit to the energies for monomer to tetramer and for larger oligomers, respectively. Reproduced with permission from Journal of American Chemical Society, submitted for publication. Unpublished work copyright 2019 American Chemical Society. [186]

example is shown for the 9-times charged pentamer in the supplement figure 9.3). For higher charged oligomers the unfolding of the DB can be detected next to the unfolding of the MB conformation; this holds true for all oligomers. The values for all the oligomers are shown in figure 5.11C. For every oligomer the smaller structures (filled circles) are assigned to native solution structures (MB and DB conformation) whereas the upper CCS values are due to the unfolding of them (green for unfolded MB and dark-blue for unfolded DB conformations).

Orthogonal to the CCS values of the IM species, the stability of the structure of an oligomer can be probed by increasing the collision energy for the purpose of CIU. Figure 5.11D shows that for increasing sizes of $A\beta$ oligomers also the energy required for unfolding increases. This energy increase is not equidistant from dimer to heptamer. Calculating the energies where 50 % unfolding of the different oligomers occurs shows a different behavior for

oligomers smaller and bigger than a tetramer. The inset in D shows by linear fits that the stability change upon oligomer growth is different for small and big oligomers (indicated by a gray and a red fit, respectively). Again the tetramer shows up as a hallmark between different behaviors of oligomerization.

All together this section shows that it is possible to use mass spectrometry to specifically detect amyloid aggregates and their structure. Ensuring the agreement of the results of the two ionization techniques ESI and LILBID enables to combine both methods for a deep study of amyloid systems. Insulin as a model system reveals that both ionization techniques do capture specific oligomers, which can be triggered by zinc (figure 5.1). However, each of these ionization techniques has its drawbacks and strengths. LILBID has the ability to detect large oligomers with a high molecular weight. A nonamer of α-synuclein is the biggest species detected with LILBID as compared to a dimer with ESI (figure 5.2). Additionally, LILBID has the possibility to detect time-dependent changes of the oligomerization status of amyloids (compare figure 5.3). On the other hand, our ESI instrument has a better resolution which makes it possible to unambiguously identify the origin of the different species, allowing to explicitly assign different signals at the same m/z to the respective oligomeric species when combining ESI-MS with IMS.
Combining the advantages of both methods enables to study an amyloidogenic system in more detail with three dimensions of information (time, oligomerization, structure). This analysis was applied in detail to the "Alzheimer peptide" beta-amyloid. LILBID enables to detect a high amount of $A\beta$ oligomers up to the 11-mer (figure 5.4) as well as the kinetics of their formation. Additional information can be gained with ESI-IMS which enables to analyze the structure of $A\beta$ oligomers. Therewith it was possible to detect two coexisting solution structures of $A\beta$, monomer-based and dimer-based oligomers. The $A\beta$ oligomer structure detected via IMS can be correlated to theoretical growth models as well as to published PDB structures of $A\beta$ fibrils. This analysis reveals that a hallmark for the formation of well-ordered fibrils is the tetramer. Altogether, this shows that the IMS technique which can analyze molecular structures on a low-resolution level can make a statement on microscopic molecular events by combining the results with literature knowledge.

5.3 Ligands Affect the Structure of $A\beta$ which Inhibits Oligomerization

The insight in the evolvement process of $A\beta$ oligomers opens the possibility to analyze the influence of ligand molecules on the oligomerization kinetic and to correlate this influence to structure alterations. This might help to understand the mechanism of $A\beta$ oligomerization and thus to influence this process as a means to treat Alzheimer's disease.
For this purpose we analyzed the influence of ligands from three different classes: agonists of the retinoid X and retinoid A receptors, peptides and peptidomimetics that reflect the KLVFF sequence of $A\beta$ and a molecular tweezer interacting with lysine side-chains.

5.3.1 RXR and RAR Ligands Influence Primary and Secondary Pathway of *A*β Oligomerization

One approach to tackle AD was to clear the cerebrospinal fluid (CSF) of $A\beta$. Additionally to the clearance effect, it was found that molecules of the class of RXR and RAR ligands showed to influence the primary and secondary oligomerization step of $A\beta$ during fibril evolvement (compare section 4.2.1). Since the influence on primary and secondary oligomerization happens on the first small aggregates during the lag-phase of fibrillation it should be possible to detect it with time-resolved LILBID-MS measurements.

ThT experiments suggested an influence of bexarotene on the primary nucleation of $A\beta$. An increase of the aggregation half-time from 2.2 h to 4.5 h was detected due to the addition of 4-fold excess of bexarotene to 2 µM $A\beta$ [142]. Figure 5.12 shows two oligomerization processes of $A\beta$ detected with TR-LILBID-MS. To one part of the sample the RXR ligand bexarotene was added in 4-fold excess, whereas the second part contained just pure $A\beta$. During sample incubation LILBID-MS spectra were recorded. In figure 5.12A selected spectra for pure $A\beta$ are shown. The process of oligomerization is evident by an intensity increase of the oligomer peaks. A more detailed look on the oligomerization is possible by calculating M/O ratios for all spectra which were recorded during the incubation. The black circles in figure 5.12C show the time-courses of the M/O ratio for pure $A\beta$. The expo-

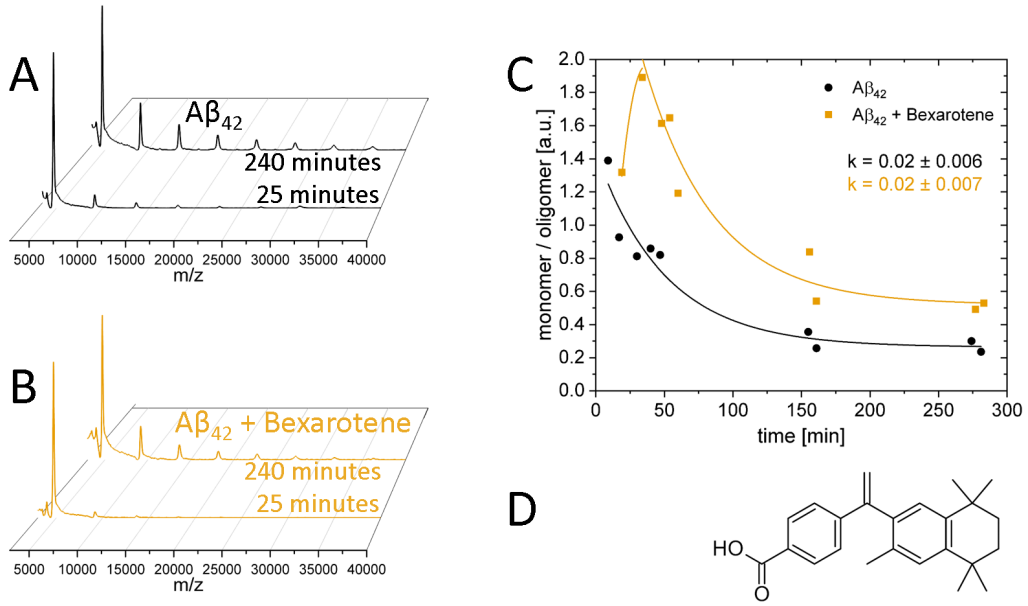

Fig. 5.12: Time-resolved process of $A\beta$ oligomerization influenced by bexarotene. A shows two respective spectra for pure $A\beta$ for an incubation time of 25 and 240 minutes. B shows two respective spectra for the same incubation times for bexarotene-influenced $A\beta$. 50 μM synthetic $A\beta_S$ was incubated in the absence or presence of 4-fold excess of bexarotene at 22 °C in 50 mM NH_4OAc with a pH of 7.4. C shows the time course of the monomer-to-oligomer ratios during the experiment. The fits are of the form of exponential decay; in the case of the yellow curve starting from minute 40. The first minutes of the yellow curve are just to guide the eyes. D gives the molecular formula of bexarotene.

nential decrease of the M/O ratio of pure $A\beta$ shows a steady oligomerization (black circles).

Figure 5.12B shows two representative spectra for bexarotene-influenced $A\beta$. Several oligomers of $A\beta$ were detected without a hint for bexarotene interaction. This is explicable in view of bexarotene being a ligand with weak and multiple interactions with the peptide [188]. Transient and weak interactions of ligands to $A\beta$ are also known for other small molecules like congo-red and lacmoid. Those weak interacting agents are known to influence $A\beta$ oligomerization [189]. This lack of observable binding also appears for bexarotene in figure 5.12B. Both $A\beta$ samples (with and without bexarotene) show an increase in size and amount of oligomers from 25 to 240 minutes of incubation. Thus, bexarotene does not inhibit the oligomerization of $A\beta$. However, comparison of both samples for the two time-points shows less oligomers for the bexarotene-containing sample. After incubation for 240 minutes the highest oligomer visible is an octamer for pure $A\beta$, wherease it is a heptamer for bexarotene-containing sample in figure 5.12B.

So bexarotene does not completely inhibit the oligomerization but it indeed modulates this process, even if no binding can be detected with MS. A more detailed look at the effect of bexarotene is possible by calculating the M/O ratio of the spectra recorded during incubation, which is shown in yellow in figure 5.12C. Bexarotene affects the continuous oligomerization of pure $A\beta$, which gets obvious within the first hour of incubation. Oligomers decrease which results in an increase in M/O ratio. Since the first minutes of the experiment are lost due to instrumental handling, it is not possible to say if bexarotene stops an ongoing $A\beta$ oligomerization or if the bexarotene effect is to act on small oligomers at the very beginning of incubation. Nevertheless, bexarotene dissolves those small oligomers and monomerizes $A\beta$. The increase of the M/O ratio reveals that this monomerization effect goes on for about 40 minutes. This is followed by a restart of the $A\beta$ oligomerization with the same kinetic as for pure $A\beta$; the kinetic constants of pure an bexarotene-influenced oligomerization (for the yellow line starting from minute 40) reveal the same values. This indeed results in less oligomers for each of the time-points during the whole experiment. Thus all of the spectra in figure 5.12B show smaller oligomers in the bexarotene-containing sample as for pure $A\beta$.
This LILBID-MS analysis on $A\beta$ aggregation reveals bexarotene affecting the very first aggregation steps of this primary nucleation process. The disaggregation of small oligomers at reaction start leads to a delay in oligomerization of about 1 h.

Next to this effect it was suggested that RAR ligands have the additional ability to block secondary aggregation which further delays the aggregation halftime. Analogue to the LILBID-MS experiment on the influence of the RXR ligand bexarotene on synthetic $A\beta_S$ an experiment was conducted where the influence of the RAR receptor BMS493 on recombinant $A\beta_R$ was studied. An $A\beta_R$ sample was split into two separate tubes. To one of them a 4-fold excess of BMS493 was added. Additionally, a DNA molecule with a molecular weight of roughly 7.5 kDa was added to both solutions for the purpose to detect intensity changes of $A\beta$ which are unrelated to the ionization efficiency (details are given in supplementary information). Figure 5.13A shows spectra for pure and figure 5.13B for BMS493 containing $A\beta$ at two time points.
Pure $A\beta$ in figure 5.13A shows several oligomer peaks with an intensity increase for longer incubation times. Additionally to signals of $A\beta$ oligomers, the peak of the DNA additive is detected. The increase of its intensity rela-

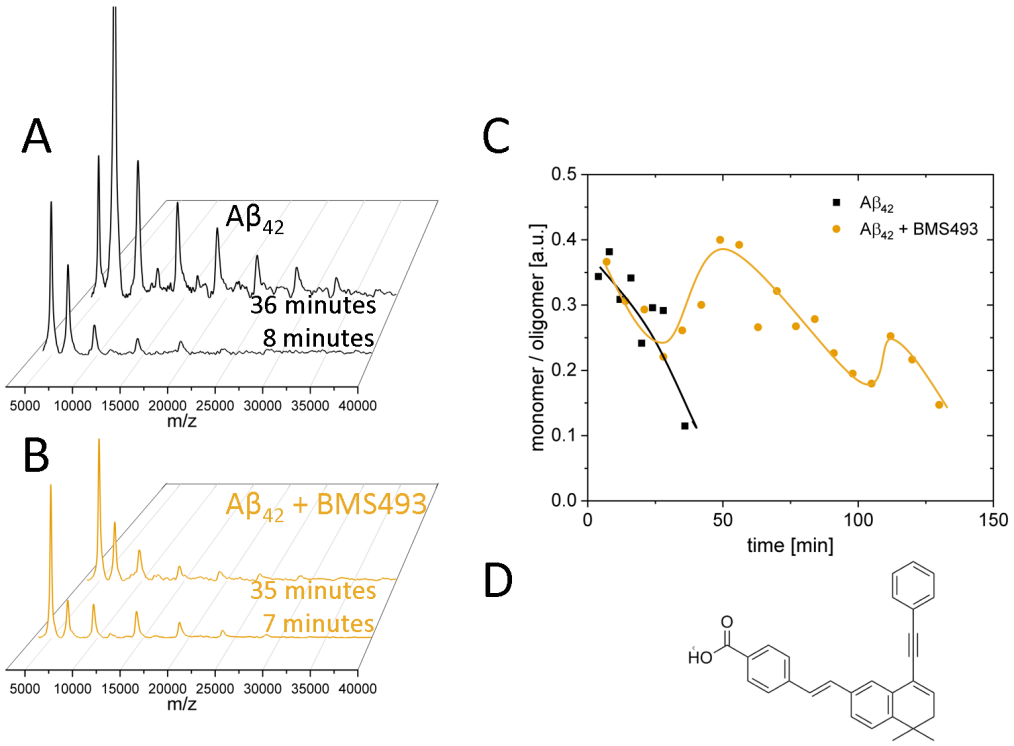

Fig. 5.13: Time-resolved LILBID-MS detects the influence of BMS493 on the process of $A\beta$ oligomerization. 20 μM of recombinant $A\beta_R$ were incubated in the absence or presence of BMS493 at 22 °C in 50 mM NH_4OAc with a pH of 7.4. A shows two respective spectra for pure $A\beta$ for an incubation time of 8 (lower) and 36 minutes (upper). B shows two representative spectra depicting the influence of the presence of a 4-fold excess of BMS493. C shows the time course of the monomer-to-oligomer ratios during the experiment. The lines are no fits but are just to guide the eyes. D gives the molecular formula of BMS493.

tive to the intensity of the $A\beta$ signals reveals a decrease in concentration of soluble $A\beta$. The signal of the herein detected small oligomers disappears because fibril structures are formed out of those aggregates. Those fibrils cannot be detected with LILBID-MS. Thus, the overall signal of $A\beta$ decreases in contrast to the signal intensity of the DNA molecule (upper spectrum in figure 5.13A). For this experiment recombinant peptide was used with the monomerization and purification procedure using SEC on an FPLC system. Thus the aggregation kinetic is much faster compared to the case of synthetic peptides (compare supplementary figure 9.2). This involves to decrease incubation times. Figure 5.13C shows that pure $A\beta_R$ oligomerizes with a fast kinetic (black squares). After 40 minutes of incubation almost no monomeric $A\beta$ is left; the M/O value decreased massively.

BMS493 influences the kinetics of the oligomerization of recombinant $A\beta$. The spectrum at start of the incubation (lower spectrum in figure 5.13B) is

similar to pure $A\beta$ in the amount of $A\beta$ aggregates. An inhibiting effect of BMS493 can be seen after a lag time of 25 minutes. The oligomer amount after half an hour (upper spectra in figure 5.13B) stays constant. Also the concentration of $A\beta$ is unaffected when comparing the signal intensities of the DNA additive. Likewise to bexarotene, no binding of BMS493 to $A\beta$ can be detected. Plotting the time-course of the M/O values gives a more detailed view on the aggregation influence of BMS493. The BMS493-containing sample (yellow) behaves similar to the aggregation of pure $A\beta$ within the first 30 minutes. The influence of BMS493 gets apparent after this lag time. BMS493 disaggregates the oligomers which were formed within the first minutes which increases the M/O ratio. As in the case for bexarotene, after 70 minutes the aggregation of $A\beta$ proceeds. As distinguished from bexarotene, after 100 minutes a second increase in M/O can be seen. This second effect of BMS493 suggests a different influence than bexarotene. Instead of shifting the aggregation once by 70 minutes, BMS493 causes a second aggregation influence which leads to a total time-shift of nearly 100 minutes. Nevertheless, this experiment was conducted just once. If the effect of BMS493 can be confirmed, a possible explanation would be that RAR ligands affect the primary and additionally the secondary aggregation pathway of $A\beta$.

These experiments reveal that LILBID-MS has the power to study the effect of molecules which induce a delay in $A\beta$ aggregation. Generally, M/O time-courses can show deceleration of aggregation as well as determine the influence of molecules to affect the primary or also the secondary aggregation process of $A\beta$. It was possible to show that LILBID can follow the effect of the RAR ligand BMS493 influencing two separate aggregation steps whereas bexarotene influences exclusively the primary nucleation. Even though an influence of those two molecules on the aggregation process can be detected, no interaction of these molecules to the $A\beta$ peptide was found. However, it is strongly concentration dependent whether a ligand interaction can be detected with MS. Just a single concentration was tested for the experiments shown herein; thus it might be possible to record an interaction of the ligand to $A\beta$ by varying the concentration and stoichiometry of the constituents.

5.3.2 Peptides and Peptidomimetics Influence $A\beta$ Oligomerization by Structural Changes

The non-existing signal for a ligand interacting to $A\beta$ is conceivably explainable by transient bindings. These might not be detected with MS [190]. Weak interactions are transient [191] which leads to a possible disruption of the ligand-peptide complex by ionization with either the LILBID or ESI mechanism. This situation should change for molecules designed to interact specifically with certain parts of the $A\beta$ peptide. Amino acids 16-20 (KLVFF) have a primary role in interactions of $A\beta$ (compare section 4.2.1). They play a major role in intermolecular interactions as well as in structure-forming intramolecular interactions. These are based on hydrophobic interactions leading to the evolvement of a central hydrophobic core (CHC) of $A\beta$ fibrils. One molecule designed to mimic the KLVFF sequence of $A\beta$ is OR1. Thus OR1 might affect inter- and intramolecular interactions. Figure 5.14A depicts OR1-influenced $A\beta$ spectra recorded for incubation times of 0 h and 48 h (yellow). At start of the incubation experiment almost exclusively $A\beta$ monomers are present. Interestingly, an interaction of OR1 to the $A\beta$ peptide can be detected (indicated by asterisks). The higher specificity of this molecule compared to the class of RXR and RAR ligands enables to detect ligand binding by mass spectrometry which can be base for analyzing the influence of KLVFF peptides on the $A\beta$ structure with IMS experiments (compare figure 5.16 and 5.17 in the second part of this section). This situation does not change significantly upon incubation. OR1 inhibits the $A\beta$ oligomerization completely. The amount of oligomers in the OR1-influenced sample did not change during 48 h; neither the size nor the amount of oligomeric species change upon incubation dramatically. For comparison the light gray spectrum shows the aggregation of pure $A\beta$ for the same incubation time. Clearly, pure $A\beta$ shows a high amount of oligomers visible up to the nonamer. The inhibiting effect of OR1 is also depicted by the M/O values. Pure $A\beta$ has a low value of 0.48 after 48 h of incubation whereas OR1 changes this value just slightly from 2.69 to 2.42. This proves the ability of the peptide OR1 to completely inhibit the aggregation of $A\beta$.

Next to the effect to inhibit the oligomerization of $A\beta$ it is desirable for a ligand to dissolve $A\beta$ aggregates. In order to test this effect, OR1 was added to an aggregated $A\beta$ sample. Figure 5.14B shows significant spectra of this experiment; the lower black spectrum is the aggregated $A\beta$ solution before OR1 addition. Clearly a high amount of oligomers can be seen. After addi-

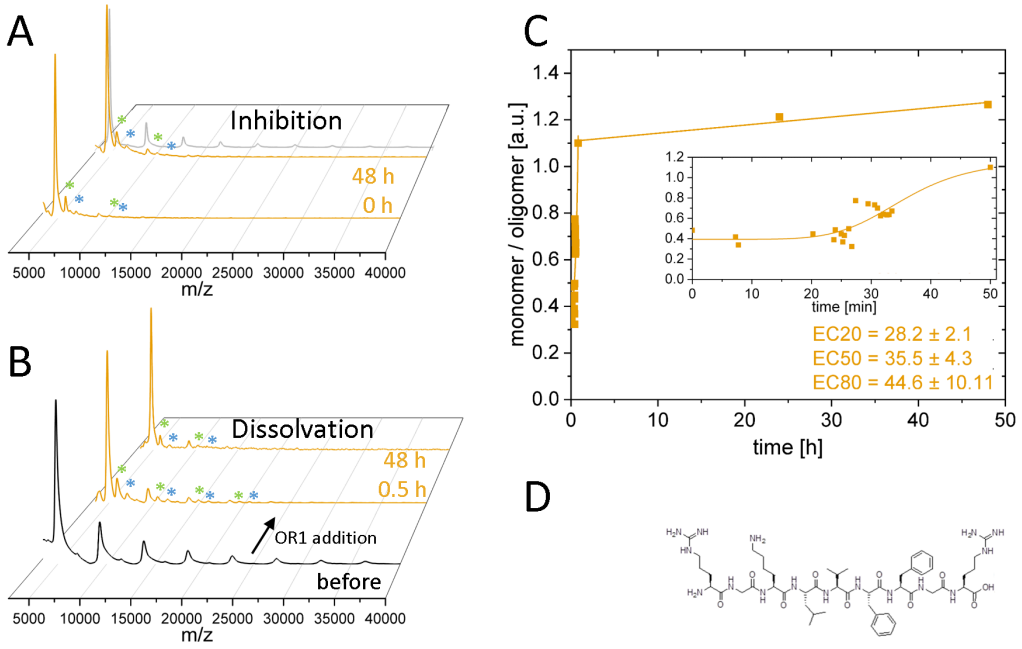

Fig. 5.14: The peptide OR1 inhibits and reverses $A\beta$ oligomerization. 100 μM of synthetic $A\beta_S$ was incubated in the absence or presence of 4-fold excess of OR1 at 22 °C; solvent conditions were the same as in the experiments described before. A shows LILBID spectra of $A\beta$ influenced by OR1, fresh and 48 h incubated (yellow). For comparison an aggregated $A\beta$ sample without OR1 after 48 h incubation is shown (light gray). The interactions of OR1 to $A\beta$ are indicated (green for $A\beta + 1\,OR1$, blue for $A\beta + 2\,OR1$). B shows the desolvation of $A\beta$ oligomers by OR1 likewise. Spectra of the experiment in B were basis to calculate monomer-to-oligomer ratios whose time-course is represented in C. The fit for long aggregation times has a linear character. The inset shows an enlargement of the first 50 minutes. The fit has a logistic sigmoidal character; the values for effective concentrations of 20, 50 and 80 % of aggregation are indicated. D shows the molecular structure of OR1. (picture modified from [4]).

tion of OR1 into this solution, the peptide binds to $A\beta$ (indicated by asterisks). The amount and size of the oligomers start to decrease within 30 minutes (lower yellow spectrum). This disaggregation of $A\beta$ oligomers continues for the next 48 h. At the end of this dissolvation experiment the aggregation was reversed, with a spectrum similar to freshly solvated $A\beta$. Figure 5.14C shows the evolvement of the disaggregation of $A\beta$ oligomers more detailed. The time-course of the M/O ratio reveals that the disaggregation process is completed already after 1 h. The inset shows a zoom to the first minutes of disaggregation after OR1 addition. After a lag-phase of about 28 minutes (expressed by the EC20 value) the oligomers are dissolved rapidly with a half-time of about 8 minutes (expressed by the EC50 value).

The ability of inhibition and reversion of soluble $A\beta$ oligomers is one of the goals to be achieved when searching for pharmaceuticals treating AD. Region of action for those pharmaceutics is the CSF and the brain, so it is impossible for OR1 to achieve this goal. OR1 is a peptide which would be degraded by peptidases in the human body directly after uptake. Furthermore, OR1 is a big hydrophilic molecules which will be massively hindered to cross the blood-brain barrier and thus will not be available at the location of action. Thus OR1 has to be modified in a way which conserves its effect on $A\beta$ but which is stable against degradation and enables to cross the blood-brain barrier. To achieve this a peptidomimetic was developed. Since peptidases only attack L-amino-acids, an approach to prevent degradation is the use of D-amino-acids [147]. To maintain structural similarity to the L-amino-acid sequence, which is necessary to allow the specific interaction to $A\beta$, a retroinverso peptide was used; therefore the starting point for the development of the modified peptidomimetic is a FFVLK order of the D-isomers. To increase the probability of the molecule to cross the blood-brain barrier it has to be small and hydrophobic [148, 192]. To achieve this, a molecule has to be designed which complies those properties. This involves several steps of synthesis. After each of the synthetis steps, the ability of the molecular intermediates to inhibit $A\beta$ fibril formation was confirmed with fluorescence correlation spectroscopy (FCS). Details of the molecular design are described in Stark et al. [4]. Hydrophilic groups of the retroinverso peptide FFVLK were exchanged to hydrophobic phenyl groups. The final structure TSP25 (figure 5.15D) was used to carry out more extensive studies on its ability to influence $A\beta$ aggregation.

The results achieved with LILBID-MS on the influence of TSP25 is summarized in figure 5.15. As for OR1 the ability to inhibit $A\beta$ oligomerization as well as to reverse it was tested. Figure 5.15A shows spectra of a TSP25-containing sample. For comparison the aggregated state of $A\beta$ after an incubation of 48 h in the absence of TSP25 is shown in light gray. Once more pure $A\beta$ incubated for 48 h shows a high amount of oligomers up to the octamer. The addition of the peptidomimetic TSP25 causes inhibition of this oligomerization process. Even if freshly solvated $A\beta$ contained some oligomers (lower yellow spectrum), the aggregation of those oligomers was stopped upon addition of TSP25; after 48 h of incubation at room temperature neither the size, nor the intensity of the oligomer signals increased. Rather the contrary happens: the biggest oligomer visible at 0 h of incu-

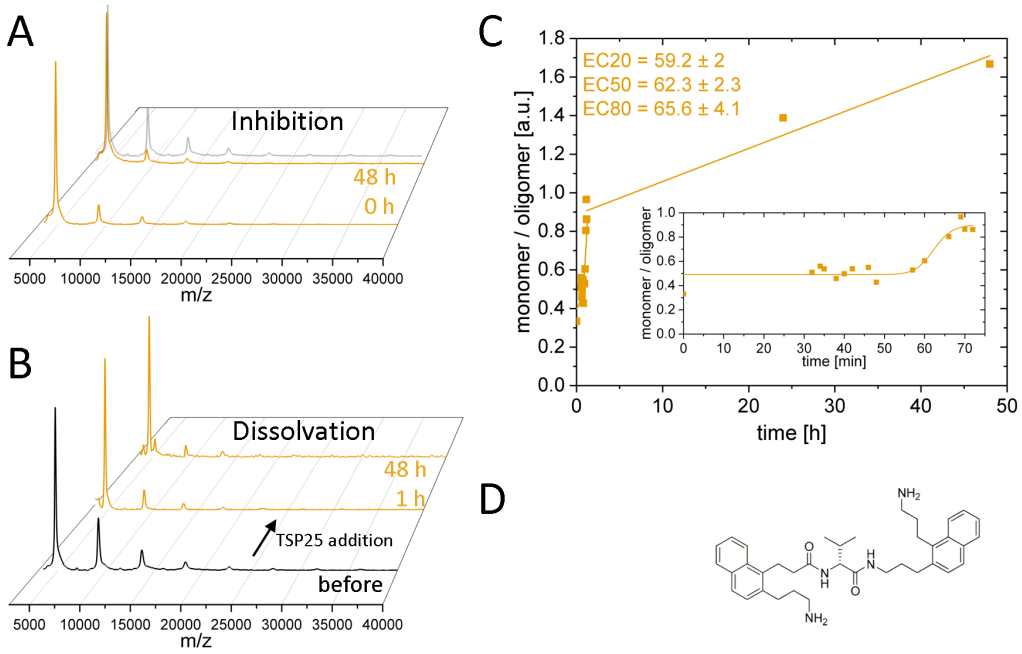

Fig. 5.15: The peptidomimetic TSP25 inhibits and reverses $A\beta$ oligomerization. 100 μM of synthetic $A\beta_S$ was incubated in the absence or presence of 4-fold excess of TSP25 at 22 °C; sample conditions were the same as in the experiments described before. A shows LILBID spectra of $A\beta$ influenced by TSP25 for two incubation times (yellow). For comparison a spectrum of pure $A\beta$ for the same incubation time is shown (light gray). B shows the dissolvation of $A\beta$ oligomers by TSP25 equally. Spectra of the experiment in B were basis to calculate monomer-to-oligomer ratios which time-course is represented in C. The inset shows an enlargement of the first 75 minutes. (picture modified from [4])

bation is a pentamer, after 48 h of incubation this oligomer gets dissolved. This is also reflected by the M/O ratio of those spectra: the value increases within 48 h from 1.33 to 1.87 meaning that $A\beta$ gets more monomeric. In contrast to the peptide OR1 no signals for interaction of TSP25 to $A\beta$ can be detected. This is a hint for less specific interactions of the peptidomimetic in comparison to OR1. However, the interaction was analyzed for a single ratio of 4:1 $A\beta$ to TSP25. Detection of ligand binding might be possible for other ratios.

Furthermore, the ability of TSP25 not only to stop, but to dissolve $A\beta$ oligomers was tested. Those results are presented in figure 5.15B and C. B shows convincing spectra for the disaggregation where TSP25 was added to an $A\beta$ solution after aggregation for 48 h (black spectrum). Already the spectrum recorded 1 h after TSP25 addition shows massively decreased oligomers. This dissolvation proceeds for the next 48 h; the M/O ratios increases continuously during that time. The result after 48 h is comparable to the effect

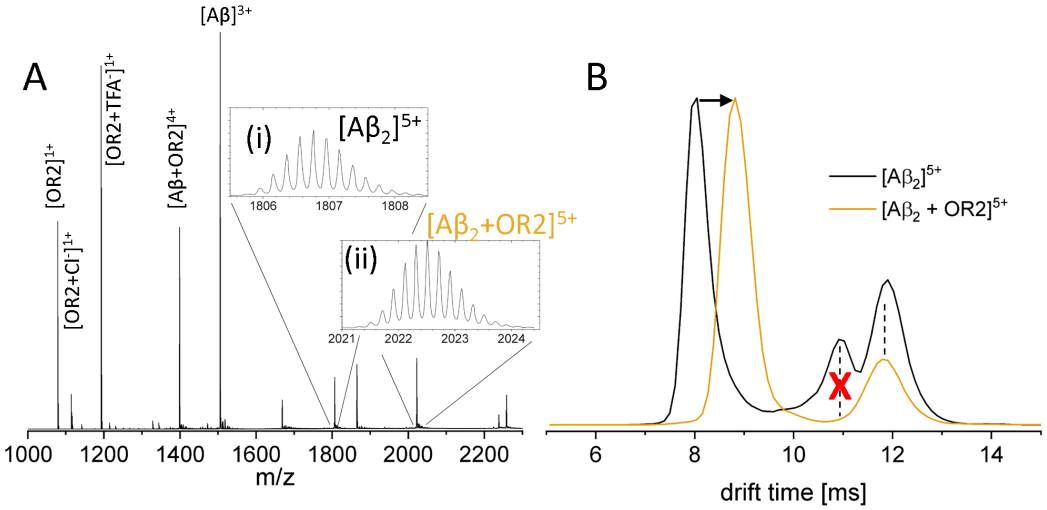

Fig. 5.16: IMS detects specific structural influences by OR2. A shows an ESI spectrum of 50 μM synthetic $A\beta_S$ in solvent conditions as described before with a 4-fold excess of OR2. The assignment of the peaks are indicated; the insets show enlargements of the spectrum contributing to the 5-times charged $A\beta_S$ dimer without (i) and with OR2 (ii). Those were used for the IMS analysis shown in B. The black ATD shows three structures being present for pure $A\beta$. The interaction of OR2 (yellow) alters each of them differently (indicated by lines and arrows).

of OR1. However, figure 5.15C shows that the kinetic of dissolvation with TSP25 is slower than with OR1. Comparing the onset of the time courses for both inhibitors reveals differences regarding the lag time. OR1 dissolves $A\beta$ aggregates with a lag-phase of 28 minutes followed by a dissolvation with a half-time of about 8 minutes. The times for the effect of TSP25 are significantly increase: the lag-phase is about 59 minutes (represented by the EC20 value) and the half-time of the first disaggregation process, which dissolvates most of the oligomers, is about 3 minutes. The complete disaggregation process continues for 48 h.

These results show that the modification of compound OR1 to achieve stability against peptidase degradation and to reach a smaller, more hydrophobic structure were gained with the pay off of lower affinity. This would be a reason why no signals for the interaction of the ligand to $A\beta$ can be detected and can also be the reason for a less efficient and slower process of oligomer inhibition and dissolvation. Nevertheless, it might be possible that this loss in effectiveness might be compensated by an increase in TSP25 concentration.

The KLVFF peptides of the OR family show interactions to $A\beta$, which re-

sults in stable $A\beta$-OR1 peaks which can be distinguished from $A\beta$ oligomer peaks in mass spectra (compare figure 5.14A). We used these signals to investigate the influence of this class of molecules to the $A\beta$ peptide. Figure 5.16 depicts the ESI-IMS analysis of OR2 interacting to $A\beta$. Figure 5.16A depicts the ESI spectrum of $A\beta$ in presence of OR2. All the appearing peaks can be assigned due to isotopic resolution. Both molecules, as well as their complexes, can be detected. The monomer of $A\beta$ lacks a molecular structure (compare section 4.2) and is irrelevant to detect quaternary structures of complexes making it unsuitable as target for this analysis. However, the dimer has a sufficient signal-noise ratio to conduct ion-mobility experiments. The signal at $m/z = 1806$ originates from the 5-times charged dimer species $[A\beta_2]^{5+}$ exclusively, without overlap of other oligomers (compare inset (i) and (ii) in figure 5.16A). This is also the case for the complex signal $[A\beta_2+OR2]^{5+}$ at $m/z = 2022$. Thus, both signals were used for structure analysis. Figure 5.16B shows the ATD of both species. The black signal for unbound $A\beta$ dimer shows three species. Corresponding to the assignment in figure 5.10 these peaks are caused by native MB, native DB and unfolded MB conformation of the $A\beta$ dimer. Comparison of the IM peaks of free and OR2-bound $A\beta$ dimer show that the interaction of OR2 to $A\beta$ changes the structure of those three different species significantly but in different ways: the native MB conformation enlarges as long as it is in its native folding (left peak in figure 5.16B). However, the unfolding product is unaffected by OR2 interaction (right peak). The peak of native DB conformation vanishes. The effect of OR2 on the MB arranged dimer can be explained with the following interpretation: The two loops of $A\beta$ are stabilized by hydrophobic and ionic interactions respectively (compare figure 4.1 and figure 6.1A). The hydrophobic site of the peptide is the weaker bound. Most likely unfolding the $A\beta$ peptide means unfolding this hydrophobic site. The ionic site of $A\beta$ (which is stabilized by a salt-bridge between the C-terminal end at Ala42 and the side chain of Lys28 [131]) is stable enough to withstand the energy impact by gas-collisions and stays intact. If OR2 would influence this ionic site of $A\beta$ it would influence the folded as well as the unfolded species of $A\beta$. However, if OR2 influences the folding of the hydrophobic part and enlarges the $A\beta$ structure by widening this loop, there will not be an influence of OR2 to the unfolded species. Gas collisions would lead to entire unfolding of the hydrophobic loop which makes an influence of OR2 invisible. Thus, these data are in line with the interpretation that OR2 interacts with the hydrophobic loop at the site of KLVFF which loosens the compaction of that site resulting in an enlargement of the $A\beta$ dimer.

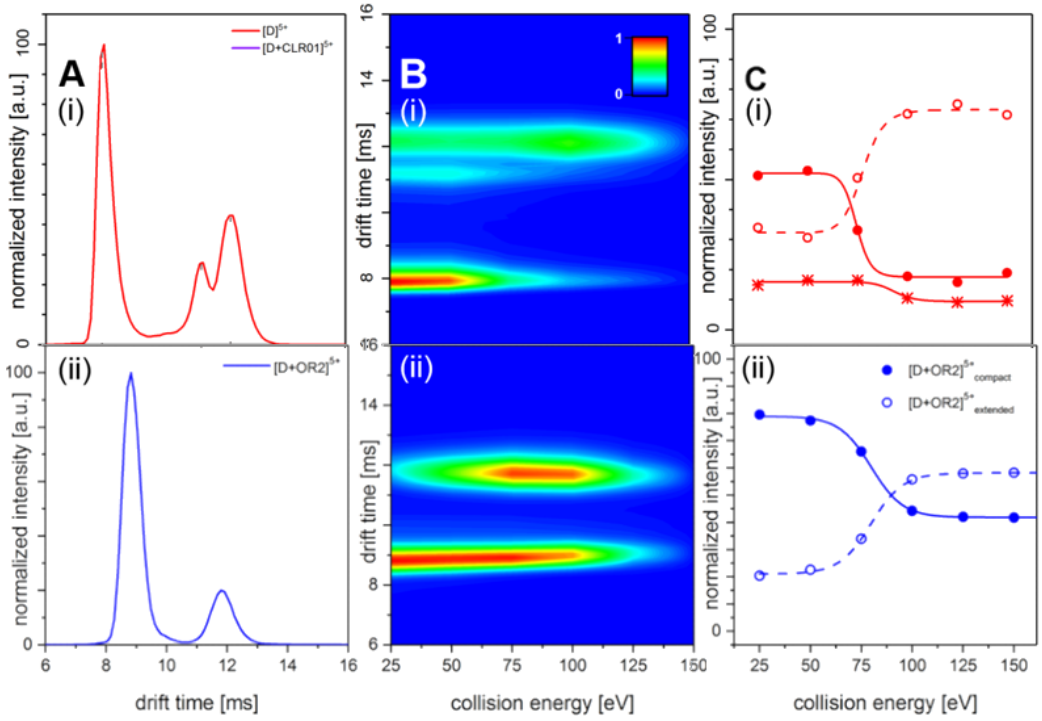

Fig. 5.17: OR2 stabilizes the structure of $A\beta$ oligomers slightly. A shows a comparison of IMS signals of pure (i) and OR2 bound (ii) $A\beta$. The heatmap of CIU experiments in B reveals an increase in the stability of $A\beta$ dimers caused by OR2 (ii). A more detailed perspective is given by a numerical depiction of this CIU experiment in C. The ATD of pure $A\beta$ (i) and OR2 bound $A\beta$ (ii) are base for calculating mean energies for unfolding. Integrals of Gaussian fits on the IMS signals were used to calculate the intensities of those signals. The sum of all IMS intensities was used to normalize the scale. Reproduced with permission from Journal of American Chemical Society, submitted for publication. Unpublished work copyright 2019 American Chemical Society. [186]

Strikingly, the DB arranged structure disappears completely upon OR2 binding (middle peak in figure 5.16B). The monomers within a layer of a DB arranged oligomer are connected via salt-bridges between the side-chain of Asp1' of monomer A to the side-chain of Lys28 of monomer B [121]. If OR2 loosens the compactness of the hydrophobic loop of $A\beta$ it also increases the distance between the two monomers which build the base for DB stacking of oligomers. The distance between Asp1' and Lys28 increases. This makes a salt-bridge between both monomers unfavorable which results in a loss of DB arranged oligomers (compare figure 6.1C).

This interpretation also gives a possible explanation for the results found for collision induced dissociation experiments. Figure 5.17 shows the unfolding of the $A\beta$ dimer for different collision energies, detected with IMS; A

repeats the depiction of the ATD shown in figure 5.16B. Figure 5.17B shows the IMS signals recorded for several collision energies as a heatmap (blue for low and red for high intensities). In (i) free $A\beta$ dissociates: the natively folded MB arranged dimer at drift-times of 8 ms dissociates into the species with a drift-time of 12 ms, whereas the DB arranged dimer at 11 ms disappears due to the competing effect of CID without a sign for unfolding. This situation changes for OR2 interaction (figure 5.17B(ii)). The MB conformer has a higher ratio of the natively folded towards its unfolded conformation, revealing that OR2 interaction leads to a higher amount of folded $A\beta$ MB dimers. To emphasize it: no signal for a DB arrangement is detected. However the dissociation of the dimeric $A\beta$ species is unaffected by OR2 binding: both signals disappear at about 120 eV.

Figure 5.17C gives a more detailed look on the unfolding process. (i) shows that free $A\beta$ has an inflection point of 85 eV. As seen in figure 5.17B, this mean unfolding energy does not change much upon OR2 interaction: the inflection point is located at a constant energy of 90 eV. However, the relative amount of the folded MB species changes upon OR2 interaction to a more folded conformation. Just 55 % of free $A\beta$ are folded at the lowest collision energy of 25 eV. For strong collisions with 150 eV the amount decreases clearly to 20 %. The situation is different when OR2 interacts: for low energies of 25 eV the amount of folded MB dimer is roughly 80 % which is an increase by an factor of nearly 1.5. For high collision energies (150 eV) this increase is even higher: unfolding of the MB dimer is just possible to a leftover of 40 % folded $A\beta$ MB dimer before dissociation; this is an increase by roughly a factor 2. These results show clearly that ligands can influence the structure of $A\beta$ which can be detected with IMS. CIU and CID experiments allow to analyze the stability of $A\beta$ oligomers which gives information about the inter- and intramolecular bonds of $A\beta$.

5.3.3 Salt-Bridge Disruption by Molecular Tweezer CLR01 Inhibits Beta-Amyloid Oligomerization

Section 5.3.2 descibes the MS and IMS findings for the case that a ligand interacts with the hydrophobic site of $A\beta$. The situation changes when a ligands interacts with the ionic loop at the opposite site of $A\beta$. One example for such a ligand is CLR01. The effect of this molecular tweezer is to interact with lysine side-chains [155] and is described in figure 5.18.

Figure 5.18 shows the result of a CIU experiment for the molecular tweezer CLR01. A shows the influence of CLR01 on the ATD of the 5-times charged $A\beta$ dimer at low collision energies. Some similarities but also some differen-

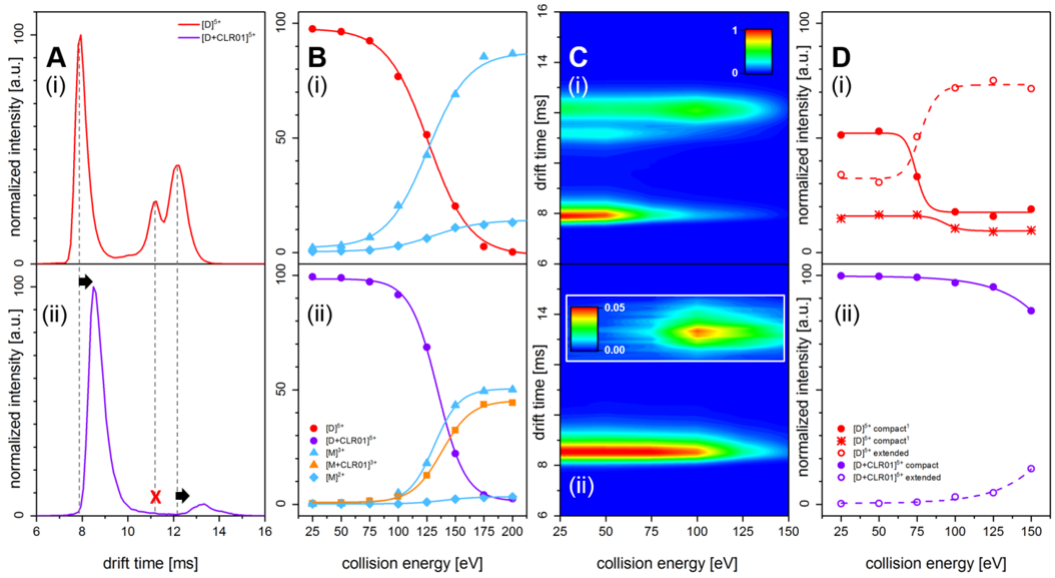

Fig. 5.18: ESI-IMS reveals that CLR01 influences the $A\beta$ structure by ionic interaction. A shows the influence of CLR01 binding (ii) on IMS structure of 5-times charged $A\beta$ dimer. Structure influences are indicated. B depicts the result of CID experiments revealing no influence of CLR01 binding to the strength of monomer-monomer interaction. This scenario changes for CIU. C shows a heatmap of the spectra of this experiment displaying just slight unfolding of CLR01 bound $A\beta$ dimer (ii) before dissociation. A numerical picture of this CIU experiment is shown in D. Integrals of Gaussian fits on the IMS signals were used to calculate the intensities of those signals. The sum of all IMS intensities was used to normalize the scale. Reproduced with permission from Journal of American Chemical Society, submitted for publication. Unpublished work copyright 2019 American Chemical Society. [186]

ces to the OR2 interaction can be seen: CLR01 enlarges the natively folded MB arranged conformation similar to the case for OR2. But in contrast to OR2 we can see CCS enlargement also for the unfolded species. This could be explained by an interaction of CLR01 to the ionic loop of $A\beta$: native $A\beta$ has a hydrophobic interaction between amino acids 17 and 32. This interaction is not influenced by CLR01, but the enlargement is due to a loss of the salt-bridge interaction at the ionic site at Lys28 [155]. Upon collision the hydrophobic site unfolds which makes an influence on the $A\beta$ structure on the hydrophobic loop ineffective (compare figure 5.17A). However, also the hydrophobically unfolded species of $A\beta$ is enlarged due to CLR01 interaction. This observation can be explained by a loss of the folding of the ionic loop additional to the loss the folding of the hydrophobic loop upon collision. When CLR01 interacts with Lys28 the positively-charged partner of the salt-bridge, which forms the S-shaped structure, gets shielded. This prevents the evolvement of the salt bridge. Thus, both loops of the S-shaped conformation unfold upon collision which causes an additional shift of the drift-time. It has to be underlined again that a signal contributing to the DB conformation is missing. Nevertheless, this is to be expected if CLR01 blocks the positive charge of the Lys28 side-chain. This side-chain is involved in the intermolecular DB interaction by evolving a salt-bridge to the second monomer of that dimeric layer. If the positive charge is blocked, an interaction is hindered which makes the DB conformation unfavorable. Figure 5.18B shows the influence of CLR01 interaction on the stability of the $A\beta$ dimer against dissociation. The free 5-times charged $A\beta$ dimer dissociates into a 2-times and a 3-times charged monomer upon collision. If CLR01 is bound to the dimer it remains bound to the 3-times charged monomer. The energy necessary to dissociate 50 % of $A\beta$ dimer is unaffected by CLR01. The heatmap in figure 5.18C shows the complete collision experiment. The MB dimer appears nearly exclusively in its folded conformation upon CLR01 interaction (figure 5.18C(ii)) revealing a stability increase against unfolding. This is shown in more detail in figure 5.18D. Nearly 100 % of the $A\beta$ dimer is folded for low collision energies, which is 2-times more than free $A\beta$. Increasing the collision energy leads to unfolding; however, this process is hindered by CLR01. $A\beta$ unfolds just to a small extent before dissociation when CLR01 interacts. Furthermore, energies necessary to unfold the S-shaped $A\beta$ peptide are influenced massively by CLR01. The molecule CLR01 has two phosphate groups which can interact with surrounding positive charges. Possibly, a second interaction can be intermolecular to the second $A\beta$ peptide or intramolecular to Asp5 or Lys16 [155]. An intermolecular interaction

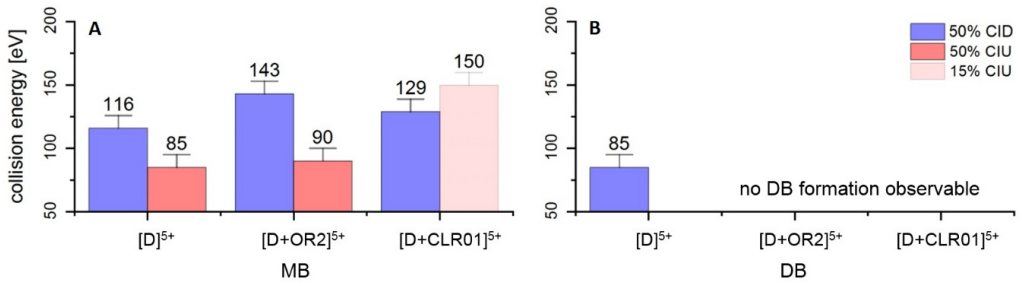

Fig. 5.19: Summary of energies necessary to unfold or dissociate an $A\beta$ dimer. Free, OR2-bound and CLR01-bound $A\beta$ (left to right) are compared for both arrangements (MB and DB). Strikingly no DB oligomer appears upon interaction of both ligands. Reproduced with permission from Journal of American Chemical Society, submitted for publication. Unpublished work copyright 2019 American Chemical Society. [186]

would increase the stability of the peptide against dissociation whereas an intramolecular interaction against unfolding.

Figure 5.19 shows the stability of both oligomer arrangements (MB and DB) against CIU and CID upon interaction of OR2 and CLR01. Strikingly, both ligands suppress the formation of DB oligomers (figure 5.19B). CID for the MB conformation is nearly unaltered upon inhibitor interaction. CID experiments for CLR01 interactions in figure 5.18B reveal that the energy for dissociation of an $A\beta$ dimer stays nearly constant after CLR01 interaction (a slight change from 116 eV to 129 eV occurs). If CLR01 interacts intermolecular, the binding strength between two $A\beta$ peptides would be enhanced which increases energies necessary to dissociate an $A\beta$ dimer. Contrary, an intramolecular interaction would influence the strength of the $A\beta$ folding. Therefore, higher collision energies would be necessary to unfold the intact hydrophobic loop. Figure 5.19A reveals that the latter situation is the case. Just a minority of 15 % of the MB $A\beta$+CLR01 species unfolds before dissociation (figure 5.19A). This is a massive increase in structural stability of $A\beta$. Thus, it is tempting to speculate that this stability increase can be explained by the second phosphate group of the CLR01 molecule. As mentioned before, CLR01 will have two separate interaction partners. Lys28 is opposite to Lys16 with a distance of roughly 20 Å. If one phosphate group of CLR01 is interacting with Lys28, the opposite Lys16 is near enough to be a possible second interaction partner. This hypothesis is affirmed by the fact that also Lys16 was detected as interaction partner of CLR01 [155]. By concurrent interaction of CLR01 to both lysine side-chains, the hydrophobic loop would be stabilized. The conjunction of Lys28-CLR01-Lys16 would increase the

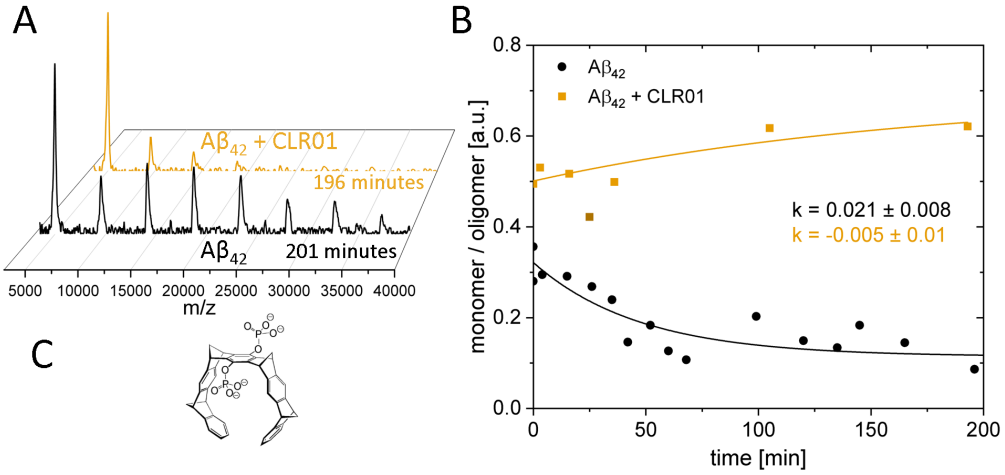

Fig. 5.20: LILBID-MS reveals that the structural changes by CLR01 on the $A\beta$ peptide influences the oligomerization kinetic. 50 μM of recombinant $A\beta_R$ was incubated in the absence or presence of 4-fold excess of CLR01 at 22 °C; solvent conditions were the same as in the experiments described before. A shows two respective spectra for an incubation time of about 200 minutes. B shows the time-course of the M/O ratio during the incubation experiment. C shows the molecular structure of the CLR01 molecule. Reproduced with permission from Journal of American Chemical Society, submitted for publication. Unpublished work copyright 2019 American Chemical Society. [186]

stability of the hydrophobic site massively with the additional ionic interaction. This would lead to suppression of unfolding.

Incubation experiments of $A\beta$ with peptides of the OR family reveal that the structure of $A\beta$ is important for regular oligomerization. Since CLR01 affects the $A\beta$ structure, LILBID-MS experiments were conducted to detect the influence of CLR01 on the aggregation kinetic. A summary of these results is depicted in figure 5.20. Figure 5.20A shows respective spectra of free and CLR01-containing $A\beta$ after incubation for about 200 minutes: clearly less oligomers appear if CLR01 interacts with $A\beta$. Figure 5.20B shows this inhibition procedure in terms of time evolvement of the M/O ratio. The oligomerization process of free $A\beta$ leads to a constant decrease of M/O values from 0.33 to 0.12 (black circles in figure 5.20B). Without the influence of CLR01, $A\beta$ oligomerizes within 200 minutes with the same kinetic constant as for previous experiments. During incubation the intensity of the monomer signal decreases and the intensities of the oligomer signals increase, especially for the large species from pentamer to dodecamer. Both results in an M/O decrease. However, CLR01 reduces the size of the oligomers and inhibits their formation. The effect of suppressing $A\beta$ oligomers results in increased

M/O values (yellow squares in figure 5.20B). CLR01 interaction leads to two effects: the intensity decrease of the monomer is stopped and the oligomer intensities stay constantly low. Both leads to the effect of a nearly constant M/O value with a slight increase from 0.5 to 0.63. This shows that CLR01 inhibits oligomerization and dissociates small oligomers.

This allows to draw the conclusion that changes on the $A\beta$ structure by CLR01 inhibit the aggregation. The S-shaped structure of beta-amyloids is disturbed which prevents a regular formation of fibrils. Even more, this structure disturbance by CLR01 reverses initially aggregated $A\beta$ (M/O=0.5) to some degree towards a monomeric condition (M/O=0.63). The disruption of the salt-bridge between Lys28 and Ala42 leads to a loss of DB arranged oligomers which suppresses the oligomerization of $A\beta$. Furthermore, the interaction of CLR01 stabilizes the three-dimensional S-shaped structure of $A\beta$. A possible explanation is that the two phosphate groups of CLR01 are interacting intramolecular which stabilizes the hydrophobic part of $A\beta$ (compare figure 6.1B).

6 A Molecular Model of Beta-Amyloid

Monomeric beta-amyloid is described as unstructured in literature, while $A\beta$ fibrils are perfectly structured (compare section 4.2). Thus it is relevant to study $A\beta$ oligomers to determine structural motifs which are relevant for aggregation. However, it is struggling to determine the molecular structure of $A\beta$ oligomers which are polymorph and transient during fibrillation. Nevertheless, recently published structures show $A\beta$ fibrils with a dimer as base module [119, 121, 131]. The monomers within that dimer have a ying-yang like arrangement (figure 6.1A). Gremer et al. show that the interaction between those two monomers is via a salt-bridge between the positively charged side-chain of Lys28 of monomer A and the negatively charged side-chain of Asp1′ of monomer B. These two positions are in spatial proximity because an $A\beta$ monomer has an S-shaped conformation consisting of two loops: a hydrophobic loop which is formed by hydrophobic interactions where the amino-acids 16-20 (KLVFF) play a major role, and an ionic loop which is stabilized by a salt-bridge between the C-terminal carboxy group of Ala42 and the side-chain of Lys28. Figure 6.1A shows that this S-shaped conformation describes the peptide for the amino-acids 11-42; the first 10 amino-acids are an L-like elongation. The amino-acids His6 and His13 are positive partners for ionic interactions to the negative side-chain of Glu11. This results in a kink of the first 10 amino-acids relative to the KLVFF region (16-20). This brings Lys28 and Asp1′ in spatial proximity.

IMS is a low-resolution technique when talking about molecular structures. However, the combination of IMS results with high-resolution structures can allow interpretation of the IMS results on a high-resolution level. The results show that the cryo-EM structure of a beta-amyloid fibril published in 2017 by Gremer et al. [121] describes our IMS-MS findings best, which renders it as base for interpretation. Thereby the structure of small oligomers of $A\beta$ can be determined.
The monomer lacks an unfolding product upon CIU which confirms that it is natively unstructured. But IMS reveals that the monomeric $A\beta$ subunits show a structure when they are part of an oligomer, starting directly with

the dimer. Already the dimer shows unfolding which reveals that the dimer is natively structured. Interpretation of the IMS results lead to consensus of structural motifs of small $A\beta$ oligomers with the interactions in $A\beta$ fibrils published by Gremer et al (compare figure 6.1A).
The growth of the aggregates occurs linearly for oligomers bigger than a tetramer; for oligomers smaller than that the growth is spherically (figure 5.9B). This shows that small oligomers do not evolve like linear fibrils but they grow as a sphere. On the other hand, bigger oligomers can be described by a fibril-like linear growth. This exhibits the tetramer as a hallmark for a regular fibril growth. In addition, the key role of the tetramer is underlined by the stability of the oligomers against collision induced unfolding: figure 5.11D shows that the energy to unfold an oligomer bigger than a tetramer increases linearly with its size.
The IMS results for small oligomers described in section 5.2 reveal two arrangements being formed abreast: the dimer-based (DB) arrangement which was published for fibrils, as well as a regular stacking of $A\beta$ having a monomer as base (MB). Understanding the quaternary arrangement of $A\beta$ oligomers deals as basis to study the effect of $A\beta$ ligands.

This analysis can be performed with different kinds of ligands with a distinct effect on $A\beta$. Time-resolved LILBID-MS measurements enable to detect various influences of molecules including non-effecting [146], delaying (RXR and RAR ligands) and inhibiting (OR peptides and the molecular tweezer CLR01) the oligomerization. Furthermore, IMS can be used to investigate the effect of ligands on the structure.
RXR and RAR ligands (bexarotene and BMS493) are interacting unspecifically and transient with the $A\beta$ peptide which leads to a delay of aggregation. Due to the transient character of the interaction, MS cannot detect a signal of the $A\beta$-ligand complex. Ligands which interact more specifically with $A\beta$ (like OR peptides and the molecular tweezer CLR01) were used to investigate the ligand's influence on the $A\beta$ structure with IMS.

Figure 6.1B depicts the interpretation of the effect when CLR01 binds to $A\beta$. As explained in section 4.2.1, the molecular tweezer CLR01 binds to lysine side chains (the molecular structure is given in figure 6.1D(i)). Lys28 plays a major role in the structure of the monomeric $A\beta$ subunit, as well as in the arrangement of DB oligomers. When CLR01 interacts to the positive charge of the Lys28 side-chain, it blocks the ability of Lys28 to be a partner for salt-bridge interactions (the regular interaction of Lys28 can be seen in

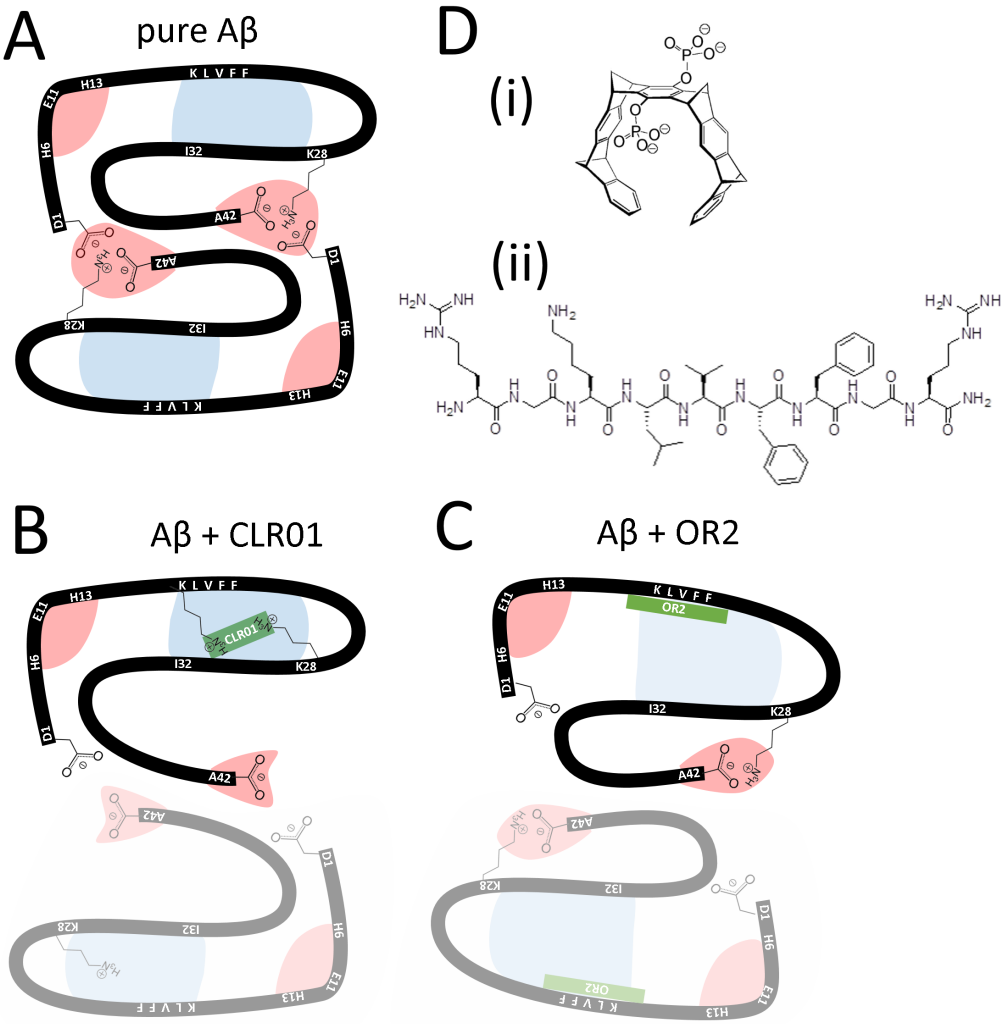

Fig. 6.1: A model of inter- and intramolecular interaction of a DB arranged $A\beta$ dimer. Ionic interactions are indicated by red shadows, blue shadows represent hydrophobic interactions. A shows free DB arranged $A\beta$ dimer; the structure represents the interpretation by Gremer et al. [121] (PDB 5OQV). In B the interaction of CLR01 to Lys16 and Lys28 of $A\beta$ is shown. C describes the interaction of OR2 to the KLVFF region of $A\beta$. The molecular structures of both ligands are shown in D, (i) for CLR01 and (ii) for OR2.

figure 6.1A. This results in two effects: first the monomeric subunits lack the Ala42-Lys28 salt-bridge (reddish) breaking the intramolecular ionic loop. This leads to a less compact S-shaped $A\beta$ structure. Second Lys28 is involved in connecting the monomeric subunits in a DB arranged oligomer. When CLR01 blocks one side of this connection, a DB arrangement is unfavored and exclusively MB oligomers occur. LILBID-MS reveals that this loss of the DB conformation has a high effect on the oligomerization of $A\beta$. Furthermore, CLR01 carries two negatively charged phosphate groups. It was shown for Ac-Lys-OMe that the phosphate moieties interact electrostatically with the ϵ-NH_3^+ of the lysine side-chain and with the backbone NH [157]. As the $A\beta$ structure places Lys28 opposite to Lys16, the IMS results could be explained if this second ϵ-NH_3^+ group deals as interaction partner. This electrostatic attraction can be stronger than the attraction by the backbone NH. This would lead to enhanced cohering forces of the hydrophobic branch. Indeed, CIU experiments show that the folding of the hydrophobic side of $A\beta$ is strengthened. This leads to the hypothesis of a link between the two lysines by CLR01.

Peptides of the OR family have a different effect when interacting with $A\beta$; nevertheless, this results in the same outcome. The disturbance of the $A\beta$ structure leads to inhibition of oligomerization. Peptides containing the KLVFF sequence (the structure for OR2 is given in figure 6.1D(ii)) interact with the hydrophobic core of $A\beta$ at amino-acids 16-20 (compare section 4.2.1). Thereupon they loosen the compactness of the hydrophobic loop (blueish) which results in enlarged drift-times for the native MB conformation in IMS experiments. Figure 6.1C shows that schematically. The unfolding product due to CIU is not affected by OR interaction which makes it possible to distinguish the position of interaction from CLR01. Enlarging the hydrophobic loop leads to a loss of the intermolecular salt-bridge interaction of Asp1′ to Lys28 and thus to a loss of the connection for DB arranged oligomers. Like in the case for CLR01, this makes a regular fibril-like oligomerization with a dimer-base unfavorable and exclusively oligomers with a monomer-base can evolve. This influences the ability of $A\beta$ to evolve a regular oligomerization kinetic.

Electron-microscopy pictures for incubated $A\beta$ in absence of any ligand show strand-like ordered fibrils [155]. Those regular fibrils are identified as *on-pathway* aggregates which show neurotoxic behavior (compare section 4.2). Ligand interaction of CLR01 [155] and OR peptides [146] lead

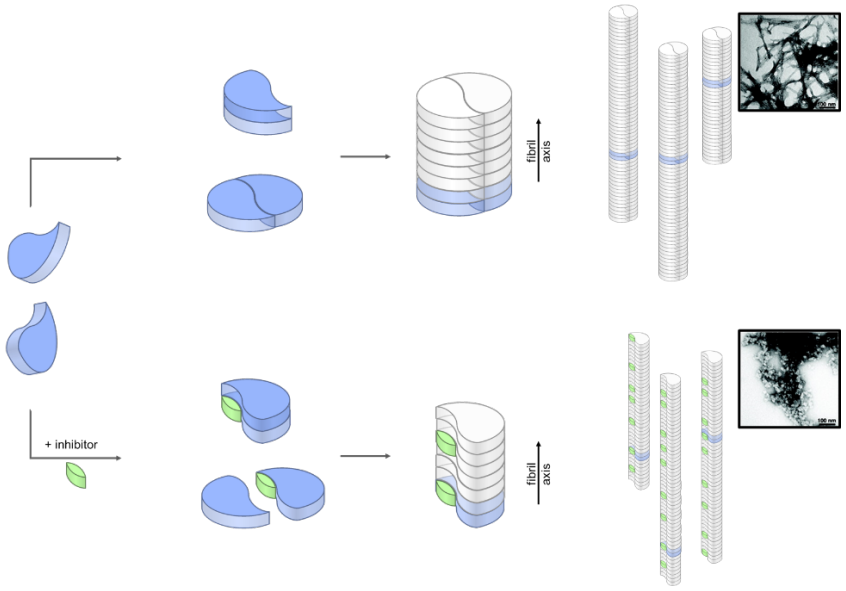

Fig. 6.2: A model for $A\beta$ oligomerization. Two pathways are indicated. The upper one is the so-called *on-pathway* which involves pure $A\beta$ forming DB arranged oligomers. This leads to fibrils (detected by Sinha et al. with EM [155]). The lower *off-pathway* is the result of inhibitor (green) interaction to $A\beta$. Just MB arranged oligomers appear which form amorphous aggregates (detected by Sinha et al. with EM [155]). Reproduced with permission from Journal of American Chemical Society, submitted for publication. Unpublished work copyright 2019 American Chemical Society. [186]

to a loss of this ordinary structure and to an evolvement of amorphous aggregates. Those were described as *off-pathway* aggregates lacking neurotoxicity. Combining this fact with the herein shown effect of ligands to the molecular structure of $A\beta$ leads to a possible interpretation of the fibrillization process of beta-amyloid: neurotoxic *on-pathway* fibrils do evolve from dimer-based oligomers (upper pathway in figure 6.2). These oligomers do evolve spherically for oligomers smaller than a tetramer but they start to evolve in a strand-like manner for oligomers bigger than a tetramer. Ligands which influence the $A\beta$ structure in a way which prevents the intermolecular interaction to form dimer-based oligomers in favor of monomer-based oligomers lead to a loss of regular *on-pathway* fibrils. The oligomerization is altered to form amorphous *off-pathway* aggregates (lower pathway in figure 6.2). Since these structures do not show neurotoxicity, this facilitates that IMS can identify variations in monomer-subunits leading to a loss of neurotoxicity.

7 Summary and Outlook of the Analysis of Amyloids with Mass Spectrometry

This second section of the dissertation describes the possibility to investigate amyloidogenic peptides and proteins with mass spectrometry. By comparing the outcomes of two different native MS techniques, advantages and disadvantages of each of the ionization techniques can be identified. Combining the advantage of LILBID-MS to detect high-order amyloid oligomers even in a time-dependent manner with the ESI-MS advantage of a good spectral resolution and the possibility for structural analysis of the peptide via ion-mobility spectrometry, expands the view on the investigated biochemical process. The study on $A\beta$ is an example to investigate amyloids. Generally it is also applicable to other amyloid systems. This thesis gives examples for the type-2 diabetes related protein human insulin, the Parkinson's disease related protein α-synuclein and the Alzheimer's diseases related peptide $A\beta$. The results for $A\beta$ allowed to postulate a molecular model of the underlying oligomerization. Correlating these low spatial resolution results to structures with high-resolution allows to conclude for the molecular mechanisms of $A\beta$ oligomerization. Additionally, LILBID-MS enabled to test several compounds which influence the aggregation behavior; molecules of different classes (RAR and RXR receptor ligands, peptides and peptidomimetics, as well as a molecular tweezer for lysine side-chains) were examined. Molecules of the latter two classes were used to study the ligand's effect on the $A\beta$ structure. Even if these ligands interact with different modes of action, the effect on the quaternary of $A\beta$ oligomers is the same: the dimer-base is weakened which leads to non-toxic amorphous aggregates. This allows to conclude on the molecular structure of disease relevant $A\beta$ oligomers. Neurotoxic oligomers evolve with a dimer-base. If ligand molecules weaken this dimer-base, oligomers with a monomer-base evolve which will generate amorphous aggregates and thus lack neurotoxicity.

Alltogether these findings help to understand the mechanism of neurotoxic $A\beta$ oligomerization. This facilitates to design molecules to successfully inhibit the evolvement of neurotoxic $A\beta$ oligomers for the purpose of treat-

ing Alzheimer's disease. Time-resolved IMS-MS can thereby deal as fast method to evaluate the effect of ligands on the structure of beta-amyloid and their influence on the aggregation kinetic.

Several open questions require further experiments on studying the oligomerization of $A\beta$ and the operation of ligands. First of all, the conditions used herein are not native. The $A\beta$ concentration of 25 µM is a factor 10,000 higher compared to in-vivo concentrations of the CSF [113]. Also the temperature as well as the ionic strength differ from in-vivo conditions. This has to be considered and those parameters have to be optimized when extrapolating the results shown herein to in-vivo conditions. Furthermore, in most of the cases a synthetically produced peptide was used. A native way for peptide production is via gene-expression. This protein-production combined with a monomerization procedure which can be applied shortly before the MS experiment can result in a more reproducible way of $A\beta$ oligomerizations. A protocol which describes a method to produce $A\beta$ peptides in this way was published by Walsh et al. [159]. Even if this peptide production was used for the experiment on the RXR ligand BMS493 (compare figure 5.13), this procedure has to be optimized for conducting MS experiments. To use recombinant $A\beta$ might give results closer to native conditions.
To optimize these parameters it is necessary to improve the MS measurements. Since higher salt and lower peptide concentrations will lead to a decrease of MS signals, the sensitivity of the MS analysis has to be refined. This involves further optimization of the ionization procedure; in terms of LILBID-MS this can for example be achieved by optimizing the IR-irradiation of the droplets. This can lead to a more effective ion production and thus to an increase in signal intensity. Furthermore, LILBID-MS resolution is not sufficient to detect the isotopic pattern of the analytes. A higher resolution of the LILBID-MS technique would enable to detect the interaction of low mass ligands. Furthermore, the LILBID-MS instrument might be extended with IMS. Since LILBID-MS is soft and produces low charged ions, LILBID-IMS-MS would enable to measure the CCS of $A\beta$ unaffected by the ionization-procedure and charge-state.

Native MS could now be employed for a more systematic screening of ligands of different classes. The molecules presented here are just a small extract of possible agents. To scan more molecules of different classes would enable to manifest and refine the molecular model of $A\beta$ aggregation which is described in this dissertation. Since only a single concentration

and stoichiometry of ligands and $A\beta$ was tested, variations of both parameters can raise additional information of the interaction mechanism. The lack of the interactions of RAR and RXR ligands to $A\beta$ might for example be caused by concentrations or stoichiometries which are too low. To make a reliable statement that these ligand interactions cannot be detected with MS, it is necessary to scan for different concentrations and stoichiometries. This would enable to confirm the transient character of the interaction. Since the concentrations and stoichiometries of all the ligands were the same throughout the experiments, the results in this dissertation show that RAR and RXR ligands interact with less affinity than other ones (e.g. OR peptides).

Some processes which have a key role in oligomerization occur on time-scales which cannot be addressed with modern mass spectrometry techniques. Copper and zinc for example accelerate the aggregation kinetic of $A\beta$ [193]. This accelerated aggregation is too fast to be recorded with LILBID-MS in a time-dependent manner (the supplementary figure 9.4 shows this for the influence of zinc). Additionally, an evaluation of the mechanism of ligand interaction to amyloids and the determination of the binding strength of monomeric subunits within an oligomer can just be analyzed on fast time-scales. Thus, to obtain values of these processes an extension of the LILBID-MS instrument with the setup for time-resolved MS experiments described in Part I of this dissertation is necessary. Detecting time-resolved processes on a sub-second time-scale enables to measure physico-chemical parameters of the different $A\beta$ species. It would for example be possible to determine the binding strength of the two conformations of $A\beta$ oligomers (MB and DB) by evaluation of exchange rates between different $A\beta$ isotopes. Different exchange rates of free and ligand-bound $A\beta$ enable to determine the binding strength of MB and DB aggregates. Thereby the detection of different exchange rates of monomers which are part of an amorphous or a fibrillary aggregate is possible. This will help to identify options to specifically attack neurotoxic *on-pathway* aggregates.

Bibliography

1. Leney, A. C. & Heck, A. J. Native Mass Spectrometry: What is in the Name? *Journal of the American Society for Mass Spectrometry* **28,** 5–13 (2017).
2. Morgner, N., Barth, H.-D. & Brutschy, B. A New Way To Detect Noncovalently Bonded Complexes of Biomolecules from Liquid Micro-Droplets by Laser Mass Spectrometry. en. *Australian Journal of Chemistry* **59,** 109 (2006).
3. Morgner, N., Kleinschroth, T., Barth, H.-D., Ludwig, B. & Brutschy, B. A novel approach to analyze membrane proteins by laser mass spectrometry: from protein subunits to the integral complex. *Journal of the American Society for Mass Spectrometry* **18,** 1429–38 (2007).
4. Stark, T., Lieblein, T., Pohland, M., *et al.* Peptidomimetics That Inhibit and Partially Reverse the Aggregation of Aβ1-42. *Biochemistry* **56,** 4840–4849 (2017).
5. Chen, F., Gülbakan, B., Weidmann, S., *et al.* Applying Mass Spectrometry to Study Non-Covalent Biomolecule Complexes. *Mass Spectrometry Reviews* **35,** 48–70. arXiv: NIHMS150003 (2016).
6. Heck, A. J. Native mass spectrometry: A bridge between interactomics and structural biology. *Nature Methods* **5,** 927–933. arXiv: NIHMS150003 (2008).
7. Schmidt, C. & Robinson, C. V. Dynamic protein ligand interactions - Insights from MS. *FEBS Journal* **281,** 1950–1964 (2014).
8. Sharon, M. How far can we go with structural mass spectrometry of protein complexes? *Journal of the American Society for Mass Spectrometry* **21,** 487–500 (2010).
9. Sharon, M. Structural MS pulls its weight. *Science* **340,** 1059–1060 (2013).

10. Konermann, L., Vahidi, S. & Sowole, M. A. Mass spectrometry methods for studying structure and dynamics of biological macromolecules. *Analytical Chemistry* **86,** 213–232 (2014).

11. Hyung, S. J. & Ruotolo, B. T. Integrating mass spectrometry of intact protein complexes into structural proteomics. *Proteomics* **12,** 1547–1564. arXiv: NIHMS150003 (2012).

12. Calabrese, A. N. & Radford, S. E. Mass spectrometry-enabled structural biology of membrane proteins. *Methods* **147,** 187–205 (2018).

13. Cech, N. B. & Enke, C. G. Practical implications of some recent studies in electrospray ionization fundamentals. *Mass Spectrometry Reviews* **20,** 362–387 (2001).

14. Kebarle, P. & Tang, L. From Ions in Solution to Ions in the Gas Phase: The Mechanism of Electrospray Mass Spectrometry. *Analytical Chemistry* **65** (1993).

15. Kebarle, P. & Peschke, M. On the mechanisms by which the charged droplets produced by electrospray lead to gas phase ions. *Analytica Chimica Acta* **406,** 11–35 (2000).

16. Dole, M., Mack, L. L., Hines, R. L., *et al.* Molecular beams of macroions. *The Journal of Chemical Physics* **49,** 2240–2249. arXiv: arXiv:1011.1669v3 (1968).

17. Benesch, J. L. P. & Ruotolo, B. T. Mass spectrometry: Come of age for structural and dynamical biology. *Current Opinion in Structural Biology* **21,** 641–649. arXiv: NIHMS150003 (2011).

18. Warnke, S., Hoffmann, W., Seo, J., *et al.* From Compact to StringThe Role of Secondary and Tertiary Structure in Charge-Induced Unzipping of Gas-Phase Proteins. *Journal of the American Society for Mass Spectrometry* **28,** 638–646 (2017).

19. Carrotta, R., Bauer, R., Waninge, R. & Rischel, C. Conformational characterization of oligomeric intermediates and aggregates in β-lactoglobulin heat aggregation. *Protein Science* **10,** 1312–1318 (2002).

20. Sun, J., Kitova, E. N., Wang, W. & Klassen, J. S. Method for distinguishing specific from nonspecific protein-ligand complexes in nanoelectrospray ionization mass spectrometry. *Analytical Chemistry* **78,** 3010–3018 (2006).

21. Hoffmann, J. *Mass spectrometry investigations on biomolecular macrocomplexes in native solutions: New insights with LILBID-MS* Dissertation (Goethe-Universität Frankfurt, 2011).

22. Hoffmann, J., Aslimovska, L., Bamann, C., *et al.* Studying the stoichiometries of membrane proteins by mass spectrometry: microbial rhodopsins and a potassium ion channel. *Physical chemistry chemical physics : PCCP* **12,** 3334–5 (2010).

23. Van Duijn, E. Current limitations in native mass spectrometry based structural biology. *Journal of the American Society for Mass Spectrometry* **21,** 971–978 (2010).

24. Barrera, N. P. & Robinson, C. V. Advances in the Mass Spectrometry of Membrane Proteins: From Individual Proteins to Intact Complexes. *Annual Review of Biochemistry* **80,** 247–271 (2011).

25. Barrera, N. P., Isaacson, S. C., Zhou, M., *et al.* Mass spectrometry of membrane transporters reveals subunit stoichiometry and interactions. *Nature Methods* **6,** 585–587 (2009).

26. Kleinekofort, W., Avdiev, J. & Brutschy, B. A new method of laser desorption mass spectrometry for the study of biological macromolecules. *International Journal of Mass Spectrometry and Ion Processes* **152,** 135–142 (1996).

27. Kleinekofort, W., Pfenninger, A., Plomer, T., Griesinger, C. & Brutschy, B. Observation of noncovalent complexes using laser-induced liquid beam ionization / de sorption. *International Journal of Mass Spectrometry and Ion Processes* **156,** 195–202 (1996).

28. Henrich, E., Sörmann, J., Eberhardt, P., *et al.* From Gene to Function: Cell-Free Electrophysiological and Optical Analysis of Ion Pumps in Nanodiscs. *Biophysical Journal* **113,** 1331–1341 (2017).

29. Laganowsky, A., Reading, E., Hopper, J. T. S. & Robinson, C. V. Mass Spectrometry of Intact Membrane Protein Complexes. *Nature protocols* **8,** 639–651 (2014).

30. Peetz, O., Henrich, E., Laguerre, A., *et al.* Insights into Cotranslational Membrane Protein Insertion by Combined LILBID-Mass Spectrometry and NMR Spectroscopy. *Analytical Chemistry* **89,** 12314–12318 (2017).

31. Hellwig, N., Peetz, O., Ahdash, Z., *et al.* Native mass spectrometry goes more native: investigation of membrane protein complexes di-

rectly from SMALPs. *Chemical communications (Cambridge, England)* (2018).

32. Morgner, N., Zickermann, V., Kerscher, S., *et al.* Subunit mass fingerprinting of mitochondrial complex I. *Biochimica et biophysica acta* **1777,** 1384–91 (2008).

33. Morgner, N., Barth, H.-D., Brutschy, B., *et al.* Binding sites of the viral RNA element TAR and of TAR mutants for various peptide ligands, probed with LILBID: a new laser mass spectrometry. *Journal of the American Society for Mass Spectrometry* **19,** 1600–11 (2008).

34. Morgner, N., Hoffmann, J., Barth, H.-D., Meier, T. & Brutschy, B. LILBID-mass spectrometry applied to the mass analysis of RNA polymerase II and an F1Fo-ATP synthase. *International Journal of Mass Spectrometry* **277,** 309–313 (2008).

35. Maciejko, J., Mehler, M., Kaur, J., *et al.* Visualizing specific Cross-Protomer Interactions in the Homo-Oligomeric Membrane Protein Proteorhodopsin by DNP-enhanced Solid-state NMR Journal: *Journal of the American Chemical Society* **137,** 9032–9043 (2015).

36. Winger, B. E., Light-Wahl, K. J., Ogorzalek Loo, R. R., Udseth, H. R. & Smith, R. D. Observation and implications of high mass-to-charge ratio ions from electrospray ionization mass spectrometry. *Journal of the American Society for Mass Spectrometry* **4,** 536–545 (1993).

37. Konijnenberg, A., Butterer, A. & Sobott, F. Native ion mobility-mass spectrometry and related methods in structural biology. *Biochimica et Biophysica Acta - Proteins and Proteomics* **1834,** 1239–1256 (2013).

38. Benesch, J. L. P., Ruotolo, B. T., Simmons, D. A. & Robinson, C. V. Protein Complexes in the Gas Phase: Technology for Structural Genomics and Proteomics. *Chemical Reviews* **107,** 3544–3567 (2007).

39. Gabelica, V. & Marklund, E. Fundamentals of ion mobility spectrometry. *Current Opinion in Chemical Biology* **42,** 51–59 (2018).

40. May, J. C., Goodwin, C. R., Lareau, N. M., *et al.* Conformational ordering of biomolecules in the gas phase: Nitrogen collision cross sections measured on a prototype high resolution drift tube ion mobility-mass spectrometer. *Analytical Chemistry* **86,** 2107–2116 (2014).

41. Salbo, R., Bush, M. F., Naver, H., *et al.* Traveling-wave ion mobility mass spectrometry of protein complexes: Accurate calibrated collision cross-sections of human insulin oligomers. *Rapid Communications in Mass Spectrometry* **26,** 1181–1193 (2012).

42. Ruotolo, B. T., Benesch, J. L. P., Sandercock, A. M., Hyung, S.-J. & Robinson, C. V. Ion mobility-mass spectrometry analysis of large protein complexes. *Nature Protocols* **3,** 1139–1152 (2008).

43. Kaltashov, I. A. & Eyles, S. J. Studies of biomolecular conformations and conformational dynamics by mass spectrometry. *Mass Spectrometry Reviews* **21,** 37–71 (2002).

44. Scarff, C. A., Thalassinos, K., Hilton, G. R. & Scrivens, J. H. Travelling wave ion mobility mass spectrometry studies of protein structure: biological significance and comparison with X-ray crystallography and nuclear magnetic resonance spectroscopy measurements. *Rapid communications in mass spectrometry : RCM* **22,** 3297–3304. arXiv: NIHMS150003 (2008).

45. Heo, C. E., Choi, T. S. & Kim, H. I. Competitive Homo- and Hetero-Self-assembly of Amyloid-β 1-42 and 1-40 in the Early Stage of Fibrillation. *International Journal of Mass Spectrometry* **428,** 15–21 (2018).

46. Chen, Y.-C. & Urban, P. L. Time-resolved mass spectrometry. *TrAC Trends in Analytical Chemistry* **44,** 106–120 (2013).

47. Rob, T. & Wilson, D. Time-resolved mass spectrometry for monitoring millisecond time-scale solution-phase processes. *European Journal of Mass Spectrometry* **18,** 205 (2012).

48. Li, K. S., Shi, L. & Gross, M. L. Mass Spectrometry-Based Fast Photochemical Oxidation of Proteins (FPOP) for Higher Order Structure Characterization. *Accounts of Chemical Research* **51,** 736–744 (2018).

49. Vahidi, S., Stocks, B. B., Liaghati-Mobarhan, Y. & Konermann, L. Submillisecond protein folding events monitored by rapid mixing and mass spectrometry-based oxidative labeling. *Analytical Chemistry* **85,** 8618–8625 (2013).

50. Perry, R. H., Splendore, M., Chien, A., Davis, N. K. & Zare, R. N. Detecting reaction intermediates in liquids on the millisecond time scale using desorption electrospray ionization. *Angewandte Chemie (International ed. in English)* **50,** 250–4 (2011).

51. Miao, Z., Chen, H., Liu, P. & Liu, Y. Development of submillisecond time-resolved mass spectrometry using desorption electrospray ionization. *Analytical chemistry* **83,** 3994–7 (2011).

52. Kolakowski, B. M. & Konermann, L. From small-molecule reactions to protein folding: Studying biochemical kinetics by stopped-flow elec-

trospray mass spectrometry. *Analytical Biochemistry* **292,** 107–114 (2001).

53. Lee, J. K., Kim, S., Nam, H. G. & Zare, R. N. Microdroplet fusion mass spectrometry for fast reaction kinetics. *Proceedings of the National Academy of Sciences.* arXiv: `arXiv:1408.1149` (2015).

54. Breuker, K. & Mclafferty, F. W. Stepwise evolution of protein native structure with electrospray into the gas phase, 10ˆ-12 to 10ˆ2 s. *PNAS* **105,** 18145–18152 (2008).

55. Zinck, N., Stark, A.-K., Wilson, D. J. & Sharon, M. An improved rapid mixing device for time-resolved electrospray mass spectrometry measurements. *ChemistryOpen* **3,** 109–14 (2014).

56. Ankenbruck, N., Courtney, T., Naro, Y. & Deiters, A. Optochemical Control of Biological Processes in Cells and Animals. *Angewandte Chemie - International Edition* **57,** 2768–2798 (2018).

57. Kumpulainen, T., Lang, B., Rosspeintner, A. & Vauthey, E. Ultrafast Elementary Photochemical Processes of Organic Molecules in Liquid Solution. *Chemical Reviews* **117,** 10826–10939 (2017).

58. Klan, P., Solomek, T., Bochet, C. G., *et al.* Photoremovable Protecting Groups in Chemistry and Biology: Reaction Mechanisms and Efficacy. *Chemical Reviews* **113,** 119–191 (2013).

59. Brieke, C., Rohrbach, F., Gottschalk, A., Mayer, G. & Heckel, A. Light-controlled tools. *Angewandte Chemie (International ed. in English)* **51,** 8446–76 (2012).

60. Brandt, E. H. Levitation in Physics. *Science* **243,** 349–355 (1989).

61. Holzscheiter, M. H. Ion-Trap Quantum Computation. *Los Alamos Science,* 264–283 (2002).

62. Paul, W. & Steinwedel, H. Ein neues Massenspektrometer ohne Magnetfeld. *Zeitschrift für Naturforschung A* **8,** 448–450 (1953).

63. Todd, J. F. & March, R. E. A retrospective review of the development and application of the quadrupole ion trap prior to the appearance of commercial instruments. *International Journal of Mass Spectrometry* **190,** 9–35 (1999).

64. March, R. E. Quadrupole ion trap mass spectrometry: a view at the turn of the century. *International Journal of Mass Spectrometry* **200,** 285–312 (2000).

65. Wuerker, R. F., Shelton, H. & Langmuir, R. V. Electrodynamic Containment of Charged Particles. *Journal of Applied Physics* **30,** 342 (1959).

66. Arnold, S. & Folan, L. M. Fluorescence spectrometer for a single electrodynamically levitated microparticle. *Review of Scientific Instruments* **57,** 2250 (1986).

67. Davis, E. J., Buehler, M. F. & Ward, T. L. The double-ring electrodynamic balance for microparticle characterization. *Review of Scientific Instruments* **61,** 1281 (1990).

68. Davis, E. J. A History of Single Aerosol Particle Levitation. *Aerosol Science and Technology* **26,** 212–254 (1997).

69. Bogan, M. J. & Agnes, G. R. MALDI-TOF-MS analysis of droplets prepared in an electrodynamic balance: "wall-less" sample preparation. *Analytical chemistry* **74,** 489–96 (2002).

70. Bogan, M. J. & Agnes, G. R. Wall-less sample preparation of ţm-sized sample spots for femtomole detection limits of proteins from liquid based UV-MALDI matrices. *Journal of the American Society for Mass Spectrometry* **15,** 486–95 (2004).

71. Guan, W., Joseph, S., Park, J. H., Krstic, P. S. & Reed, M. a. Paul trapping of charged particles in aqueous solution. *Proceedings of the National Academy of Sciences of the United States of America* **108,** 9326–30 (2011).

72. Kohno, J. Y., Higashiura, T., Eguchi, T., Miura, S. & Ogawa, M. Development of a Tandem Electrodynamic Trap Apparatus for Merging Charged Droplets and Spectroscopic Characterization of Resultant Dried Particles. *Journal of Physical Chemistry B* **120,** 7696–7703 (2016).

73. Ostermayr, T. M., Gebhard, J., Haffa, D., *et al.* A transportable Paul-trap for levitation and accurate positioning of micron-scale particles in vacuum for laser-plasma experiments. *Review of Scientific Instruments* **89** (2018).

74. Werth, G., Gheorghe, V. N. & Major, F. G. *Charged Particle Traps II: Applications* 286 (Springer Science & Business Media, 2009).

75. Zhao, X. & Krstic, P. S. A molecular dynamics simulation study on trapping ions in a nanoscale Paul trap. *Nanotechnology* **19** (2008).

76. Mathieu, P. M. E. Le Mouvement Vibratoire d'une Membrane de Forme Elliptique. *Journal de Mathématiques pures et appliquées* **2,** 137–203 (1868).

77. March, R. E. An Introduction to Quadrupole Ion Trap Mass Spectrometry. *Journal of Mass Spectrometry* **32,** 351–369 (1997).

78. McLachlan, N. *Theory and Application of Mathieu Functions:* 1st ed., 401 (Oxford, Clarendon Press, Oxford, 1947).

79. Nappi, M., Weil, C., Cleven, C. D., *et al.* Visual representations of simulated three-dimensional ion trajectories in an ion trap mass spectrometer. *International Journal of Mass Spectrometry and Ion Processes* **161,** 77–85 (1997).

80. Lamb, D., Moyle, A. M. & Brune, W. H. The environmental control of individual aqueous particles in a cubic electrodynamic levitation system. *Aerosol Science and Technology* **24,** 263–278 (1996).

81. Vehring, R., Aardahl, C. L., Davis, E. J., Schweiger, G. & Covert, D. S. Electrodynamic trapping and manipulation of particle clouds. *Review of Scientific Instruments* **68,** 70–78 (1997).

82. Shaw, R. A., Lamb, D. & Moyle, A. M. An electrodynamic levitation system for studying individual cloud particles under upper-tropospheric conditions. *Journal of Atmospheric and Oceanic Technology* **17,** 940–948 (2000).

83. Kramer, B., Hubner, O., Vortisch, H., *et al.* Homogeneous nucleation rates of supercooled water measured in single levitated microdroplets. *The Journal of Chemical Physics* **111,** 6521 (1999).

84. Shaw, R. A. & Lamb, D. Experimental determination of the thermal accommodation and condensation coefficients of water. *Journal of Chemical Physics* **111,** 10659–10663 (1999).

85. Xue, H., Moyle, A. M., Magee, N., Harrington, J. Y. & Lamb, D. Experimental Studies of Droplet Evaporation Kinetics: Validation of Models for Binary and Ternary Aqueous Solutions. *Journal of the Atmospheric Sciences* **62,** 4310–4326 (2005).

86. Singh, M., Mayya, Y. S., Gaware, J. & Thaokar, R. M. Levitation dynamics of a collection of charged droplets in an electrodynamic balance. *Journal of Applied Physics* **121** (2017).

87. Achtzehn, T., Müller, R., Duft, D. & Leisner, T. The Coulomb instability of charged microdroplets: Dynamics and scaling. *European Physical Journal D* **34,** 311–313 (2005).

88. Bogan, M. J. & Agnes, G. R. Preliminary investigation of electrodynamic charged droplet processing to couple capillary liquid chromatography with matrix-assisted laser desorption/ionization mass spectrometry. *Rapid Communications in Mass Spectrometry* **18,** 2673–2681 (2004).

89. Rayleigh, L. On the equilibrium of liquid conducting masses charged with electricity. *The London, Edinburgh, and Dublin Philosophical Magazine and Journal of Science* **14,** 184–186 (1882).

90. Wender, C. *Speicherung und gezielte Kollision zweier Partikel in einer elektrodynamischen Falle* Diplomarbeit (Technische UniversitĺAt at Ilmenau Matehmatisch, 2007), 1–96.

91. Zhang, R., Zhang, L. & Somasundaran, P. Study of mixtures of n-dodecyl-β-D-maltoside with anionic, cationic, and nonionic surfactant in aqueous solutions using surface tension and fluorescence techniques. *Journal of Colloid and Interface Science* **278,** 453–460 (2004).

92. Glycerine Producers' Association. *Physical properties of glycerine and its solutions* 1–27. arXiv: `arXiv:1011.1669v3` (Glycerine Producers' Association, New York, 1963).

93. Gekko, K. & Timasheff, S. N. Mechanism of Protein Stabilization by Glycerol: Preferential Hydration in Glycerol-Water Mixtures. *Biochemistry* **20,** 4667–4676 (1981).

94. Fischer, T. *Optimierung der Speicherung und gezielten Freigabe von geladenen Tropfen mit einer elektrodynamischen Falle* Masterpraktikum (Goethe-University Frankfurt, 2017).

95. Alzheimer, A. Über eine eigenartige Erkrankung der Hirnrinde. *Allgemeine Zeitschrift für Psychiatrie und psychisch-gerichtliche Medizi* **64,** 146–148 (1907).

96. Sipe, J. D., Benson, M. D., Buxbaum, J. N., *et al.* Nomenclature 2014: Amyloid fibril proteins and clinical classification of the amyloidosis. *Amyloid* **21,** 221–224 (2014).

97. Frimpong, A. K., Abzalimov, R. R., Uversky, V. N. & Kaltashov, I. A. Characterizationof intrinsically disordered proteins with electrospray inization mass spectrometry: Conformationl heterogeneity of α-synuciein. *Proteins: Structure, Function and Bioinformatics* **78,** 714–722 (2010).

98. Paslawski, W., Mysling, S., Thomsen, K., Jørgensen, T. J. D. & Otzen, D. E. Co-existence of two different α-synuclein oligomers with different core structures determined by hydrogen/deuterium exchange mass spectrometry. *Angewandte Chemie - International Edition* **53,** 7560–7563 (2014).

99. Liu, Y. Q., Ho, L. H., Carver, J. A. & Pukala, T. L. Ion Mobility Mass Spectrometry Studies of the Inhibition of Alpha Synuclein Amyloid Fibril Formation by (-)-Epigallocatechin-3-Gallate. *Australian Journal of Chemistry* **64,** 36–40 (2011).

100. Bernstein, S. L., Liu, D., Wyttenbach, T., *et al.* α-Synuclein: Stable compact and extended monomeric structures and pH dependence of dimer formation. *Journal of the American Society for Mass Spectrometry* **15,** 1435–1443 (2004).

101. Konijnenberg, A., Ranica, S., Narkiewicz, J., *et al.* Opposite Structural Effects of Epigallocatechin-3-gallate and Dopamine Binding to α-sSynuclein. *Journal of the American Chemical Society* **88,** 8468–8475 (2016).

102. Han, J. Y., Choi, T. S. & Kim, H. I. Molecular Role of Ca2+and Hard Divalent Metal Cations on Accelerated Fibrillation and Interfibrillar Aggregation of α-Synuclein. *Scientific Reports* **8,** 1–11 (2018).

103. Mason, R. J., Paskins, A. R., Dalton, C. F. & Smith, D. P. Copper Binding and Subsequent Aggregation of α-Synuclein Are Modulated by N-Terminal Acetylation and Ablated by the H50Q Missense Mutation. *Biochemistry* **55,** 4737–4741 (2016).

104. Connolly, B. S. & Lang, A. E. Pharmacological treatment of Parkinson disease: A review. *JAMA - Journal of the American Medical Association* **311,** 1670–1683 (2014).

105. Lim, S. Y., Fox, S. H. & Lang, A. E. Overview of the extranigral aspects of parkinson disease. *Archives of Neurology* **66,** 167–172. arXiv: `NIHMS150003` (2009).

106. Birkmayer, W. & Hornykiewicz, O. Der L-Dioxyphenylalanin (=L-DOPA)-Effekt beim Parkinson-Syndrom des Menschen: Zur Pathogenese und Behandlung der Parkinson-Akinese. *Archiv für Psychiatrie und Nervenkrankheiten Vereinigt mit Zeitschrift für die Gesamte Neurologie und Psychiatrie* **203,** 560–574 (1962).

107. Ehrnhoefer, D. E., Bieschke, J., Boeddrich, A., *et al.* EGCG redirects amyloidogenic polypeptides into unstructured, off-pathway oligomers. *Nature structural & molecular biology* **15,** 558–566 (2008).

108. Chen, S. W., Drakulic, S., Deas, E., *et al.* Structural characterization of toxic oligomers that are kinetically trapped during α-synuclein fibril formation. *Proceedings of the National Academy of Sciences* **112,** E1994–E2003 (2015).

109. Martin, J., Zangl, R., Lieblein, T. & Morgner, N. *Influence of EGCG on the aggregation of α-Synuclein wildtype and its mutant A53T* in *European Mass Spectrometry Conference 2018* (Saarbrücken, 2018).

110. Povova, J., Ambroz, P., Bar, M., *et al.* Epidemiological of and risk factors for Alzheimer's disease: a review. *Biomedical papers of the Medical Faculty of the University Palacký, Olomouc, Czechoslovakia* **156,** 108–14 (2012).

111. Folch, J., Ettcheto, M., Petrov, D., *et al.* Review of the advances in treatment for Alzheimer disease: strategies for combating β-amyloid protein. *Neurología (English Ed.)* **33,** 47–58 (2017).

112. Kumar, A., Singh, A. & Ekavali. A review on Alzheimer's disease pathophysiology and its management: An update. *Pharmacological Reports* **67,** 195–203. arXiv: `/msrj.chm.msu.edu/fall-2014-24/ [http:]` (2015).

113. Hamley, I. W. The Amyloid Beta Peptide: A Chemist's Perspective. Role in Alzheimer's and Fibrillization. *Chemical Reviews* **112,** 5147–5192 (2012).

114. Alzheimer's Association. 2018 Alzheimer's Disease Facts and Figures. *Alzheimer's & dementia : the journal of the Alzheimer's Association* **14,** 367–429 (2018).

115. Hippius, H. & Neundörfer, G. The discovery of Alzheimer's disease. *Dialogues in Clinical Neuroscience* **5,** 101–108 (2003).

116. Zhao, L. N., Long, H., Mu, Y. & Chew, L. Y. The toxicity of amyloid β oligomers. *International Journal of Molecular Sciences* **13,** 7303–7327 (2012).

117. Rajasekhar, K, Chakrabarti, M. & Govindaraju, T. Function and toxicity of amyloid beta and recent therapeutic interventions targeting amyloid beta in Alzheimer's disease. *Chem. Commun.* **51,** 13434–13450 (2015).

118. Petkova, A. T., Ishii, Y., Balbach, J. J., *et al.* A structural model for Alzheimer's β-amyloid fibrils based on experimental constraints from solid state NMR. *Proceedings of the National Academy of Sciences of the United States of America* **99,** 16742–7 (2002).

119. Wälti, M. A., Ravotti, F., Arai, H., *et al.* Atomic-resolution structure of a disease-relevant Aβ(1-42) amyloid fibril. *Proceedings of the National Academy of Sciences* **113,** E4976–E4984 (2016).

120. Gu, L. & Guo, Z. Alzheimer's Aβ42 and Aβ40 peptides form interlaced amyloid fibrils. *J Neurochem* **126,** 305–311. arXiv: NIHMS150003 (2013).

121. Gremer, L., Schölzel, D., Schenk, C., *et al.* Fibril structure of amyloid-β(1-42) by cryo-electron microscopy. *Science (New York, N.Y.)* **358,** 116–119 (2017).

122. Lee, S. J. C., Nam, E., Lee, H. J., Savelieff, M. G. & Lim, M. H. Towards an understanding of amyloid-β oligomers: characterization, toxicity mechanisms, and inhibitors. *Chem. Soc. Rev.* **46,** 310–323 (2017).

123. Goedert, M. & Spillantini, M. G. A Century of Alzheimer ' s Disease. *Science* **314,** 777–781 (2006).

124. Irwin, J. A., Edward Wong, H. & Kwon, I. Determining binding sites of polycyclic aromatic small molecule-based amyloid-beta peptide aggregation modulators using sequence-specific antibodies. *Analytical Biochemistry* **470,** 61–70 (2015).

125. Hartley, D. M., Walsh, D. M., Ye, C. P., *et al.* Protofibrillar intermediates of amyloid beta-protein induce acute electrophysiological changes and progressive neurotoxicity in cortical neurons. *The Journal of neuroscience : the official journal of the Society for Neuroscience* **19,** 8876–8884 (1999).

126. Gilbert, B. J. The role of amyloid in the pathogenesis of Alzheimer's disease. *J Clin Pathol* **66,** 362–366 (2013).

127. Bu, X. L., Rao, P. P. & Wang, Y. J. Anti-amyloid Aggregation Activity of Natural Compounds: Implications for Alzheimer's Drug Discovery. *Molecular Neurobiology* **53,** 3565–3575 (2016).

128. Anand, R., Gill, K. D. & Mahdi, A. A. Therapeutics of Alzheimer's disease: Past, present and future. *Neuropharmacology* **76,** 27–50 (2014).

129. Defelice, F. G. & Ferreira, S. T. Physiopathological modulators of amyloid aggregation and novel pharmacological approaches in Alzheimer's disease. *Anais da Academia Brasileira de Ciencias* **74,** 265–284 (2002).

130. Miller, Y., Ma, B. & Nussinov, R. Polymorphism in alzheimer Aβ amyloid organization reflects conformational selection in a rugged energy landscape. *Chemical Reviews* **110,** 4820–4838 (2010).

131. Colvin, M. T., Silvers, R., Ni, Q. Z., *et al.* Atomic Resolution Structure of Monomorphic Aβ42 Amyloid Fibrils. *Journal of the American Chemical Society* **138,** 9663–9674. arXiv: 15334406 (2016).

132. Xiao, Y., Mcelheny, D., Parthasarathy, S., *et al.* Aβ(1-42) Fibril Structure Illuminates Self-recognition and Replication of Amyloid in Alzheimer's. *Nat Struct Mol Biol.* **22,** 499–505 (2015).

133. Jiang, D., Rauda, I., Han, S., Chen, S. & Zhou, F. Aggregation pathways of the amyloid β(1-42) peptide depend on its colloidal stability and ordered β-sheet stacking. *Langmuir* **28,** 12711–12721 (2012).

134. Kłoniecki, M., Jabłonowska, A., Poznański, J., *et al.* Ion mobility separation coupled with MS detects two structural states of alzheimer's disease Aβ1-40 peptide oligomers. *Journal of Molecular Biology* **407,** 110–124 (2011).

135. Woods, L. A., Radford, S. E. & Ashcroft, A. E. Advances in ion mobility spectrometry-mass spectrometry reveal key insights into amyloid assembly. *Biochimica et Biophysica Acta - Proteins and Proteomics* **1834,** 1257–1268 (2013).

136. Sitkiewicz, E., Kłoniecki, M., Poznański, J., Bal, W. & Dadlez, M. Factors influencing compact-extended structure equilibrium in oligomers of aβ1-40 peptide - An ion mobility mass spectrometry study. *Journal of Molecular Biology* **426,** 2871–2885 (2014).

137. Taylor, M., Moore, S., Mayes, J., *et al.* Development of a proteolytically stable retro-inverso peptide inhibitor of β-amyloid oligomerization as a potential novel treatment for Alzheimers Disease. *Biochemistry* **49,** 3261–3272 (2010).

138. Roses, A. D. & Saunders, A. M. APOE is a major susceptibility gene for Alzheimer's disease. *Current Opinion in Biotechnology* **5,** 663–667 (1994).

139. Cramer, P. E., Cirrito, J. R., Wesson, D. W., *et al.* ApoE-Directed Therapeutics Rapidly Clear b-Amyloid and Reverse Deficits in AD Mouse

Models. *Science (New York, N.Y.)* **335,** 1503–1506. arXiv: NIHMS150003 (2012).

140. Mandrekar-Colucci, S. & Landreth, G. E. Nuclear Receptors as Therapeutic Targets for Alzheimer's Disease. *Expert Opin Ther Targets* **15,** 1085–1097. arXiv: NIHMS150003 (2011).

141. Tousi, B. The emerging role of bexarotene in the treatment of Alzheimer's disease: Current evidence. *Neuropsychiatric Disease and Treatment* **11,** 311–315 (2015).

142. Habchi, J., Arosio, P., Perni, M., *et al.* An anti-cancer drug suppresses the primary nucleation reaction that initiates the formation of toxic Aβ aggregates associated with Alzheimer's disease. *Science Advances* **2,** e1501244 (2016).

143. Cohen, S. I. A., Linse, S., Luheshi, L. M., *et al.* Proliferation of amyloid-β 42 aggregates occurs through a secondary nucleation mechanism. *PNAS* **110,** 9758–9763 (2013).

144. Habchi, J., Chia, S., Limbocker, R., *et al.* Systematic development of small molecules to inhibit specific microscopic steps of Aβ42 aggregation in Alzheimer's disease. *Proceedings of the National Academy of Sciences* **114,** E200–E208 (2016).

145. Austen, B. M., Paleologou, K. E., Ali, S. a. E., *et al.* Designing peptide inhibitors for oligomerization and toxicity of Alzheimer's β-amyloid peptide. *Biochemistry* **47,** 1984–1992 (2008).

146. Cernescu, M., Stark, T., Kalden, E., *et al.* Laser-induced liquid bead ion desorption mass spectrometry: an approach to precisely monitor the oligomerization of the β-amyloid peptide. *Analytical chemistry* **84,** 5276–84 (2012).

147. Matharu, B., El-Agnaf, O., Razvi, A. & Austen, B. M. Development of retro-inverso peptides as anti-aggregation drugs for β-amyloid in Alzheimer's disease. *Peptides* **31,** 1866–1872 (2010).

148. Pardridge, W. M. The blood-brain barrier: bottleneck in brain drug development. *NeuroRx : the journal of the American Society for Experimental NeuroTherapeutics* **2,** 3–14 (2005).

149. Attar, A., Chan, W.-T. C., Klärner, F.-G., Schrader, T. & Bitan, G. Safety and pharmacological characterization of the molecular tweezer CLR01 - a broad-spectrum inhibitor of amyloid proteins' toxicity. *BMC pharmacology & toxicology* **15,** 23 (2014).

150. Attar, A. & Bitan, G. Disrupting Self-Assembly and Toxicity of Amyloidogenic Protein Oligomers by Molecular Tweezers - from the Test Tube to Animal Models Aida. *Curr Pharm Des* **20,** 2469–2483. arXiv: NIHMS150003 (2014).

151. Attar, A., Rahimi, F. & Bitan, G. Modulators of amyloid protein aggregation and toxicity: EGCG and CLR01. *Translational Neuroscience* **4,** 385–409 (2013).

152. Attar, A., Ripoli, C., Riccardi, E., *et al.* Protection of primary neurons and mouse brain from Alzheimer's pathology by molecular tweezers. *Brain* **135,** 3735–3748 (2012).

153. Schrader, T., Bitan, G. & Klärner, F.-G. Molecular tweezers for lysine and arginine - powerful inhibitors of pathologic protein aggregation. *Chemical communications* **52,** 11318–11334 (2016).

154. Sinha, S., Du, Z., Maiti, P., *et al.* Comparison of three amyloid assembly inhibitors: The sugar scyllo- inositol, the polyphenol epigallocatechin gallate, and the molecular tweezer CLR01. *ACS Chemical Neuroscience* **3,** 451–458 (2012).

155. Sinha, S., Lopes, D. H. J., Du, Z., *et al.* Lysine-specific molecular tweezers are broad-spectrum inhibitors of assembly and toxicity of amyloid proteins. *Journal of the American Chemical Society* **133,** 16958–16969 (2011).

156. Sinha, S., Lopes, D. H. J. & Bitan, G. A key role for lysine residues in amyloid β-protein folding, assembly, and toxicity. *ACS Chemical Neuroscience* **3,** 473–481 (2012).

157. Fokkens, M., Schrader, T. & Klärner, F. G. A molecular tweezer for lysine and arginine. *Journal of the American Chemical Society* **127,** 14415–14421 (2005).

158. Zarándi, M., Soós, K., Fülöp, L., *et al.* Synthesis of Aβ(1-42) and its derivatives with improved efficiency. *Journal of Peptide Science* **13,** 94–99 (2007).

159. Walsh, D. M., Thulin, E., Minogue, A. M., *et al.* A facile method for expression and purification of the Alzheimer's disease-associated amyloid β-peptide. *FEBS Journal* **276,** 1266–1281 (2009).

160. Fezoui, Y, Hartley, D. M., Harper, J. D., *et al.* An improved method of preparing the amyloid beta-protein for fibrillogenesis and neurotoxicity experiments. *Amyloid: the international journal of experimental*

and clinical investigation: the official journal of the International Society of Amyloidosis **7,** 166–178 (2000).

161. Stine, W. B., Dahlgren, K. N., Krafft, G. a. & LaDu, M. J. In vitro characterization of conditions for amyloid-beta peptide oligomerization and fibrillogenesis. *The Journal of biological chemistry* **278,** 11612–22 (2003).

162. Guo, Z., Xue, C., Lin, T. Y. & Chang, D. Thioflavin T as an amyloid dye: fibril quantification, optimal concentration and effect on aggregation. *R. Soc. open sci.* **4** (2016).

163. Cerf, E., Sarroukh, R., Tamamizu-Kato, S., *et al.* Antiparallel beta-sheet: a signature structure of the oligomeric amyloid beta-peptide. *The Biochemical journal* **421,** 415–423 (2009).

164. Younan, N. D. & Viles, J. H. A Comparison of Three Fluorophores for the Detection of Amyloid Fibers and Prefibrillar Oligomeric Assemblies. ThT (Thioflavin T); ANS (1-Anilinonaphthalene-8-sulfonic Acid); and bisANS (4,4-Dianilino-1,1-binaphthyl-5,5-disulfonic Acid). *Biochemistry* **54,** 4297–4306. arXiv: `0508027v3 [physics]` (2015).

165. Re, F., Airoldi, C., Zona, C., *et al.* Beta Amyloid Aggregation Inhibitors: Small Molecules as Candidate Drugs for Therapy of Alzheimers Disease. *Current Medicinal Chemistry* **17,** 2990–3006 (2010).

166. D'Amico, M., Di Carlo, M. G., Groenning, M., *et al.* Thioflavin T promotes Aβ(1-40) amyloid fibrils formation. *Journal of Physical Chemistry Letters* **3,** 1596–1601 (2012).

167. Gade Malmos, K., Blancas-Mejia, L. M., Weber, B., *et al.* ThT 101: a primer on the use of thioflavin T to investigate amyloid formation. *Amyloid* **24,** 1–16 (2017).

168. Biancalana, M. & Koide, S. Molecular Mechanism of Thioflavin-T Binding to Amyloid Fibrils. *Biochimica et Biophysica Acta - Proteins and Proteomics* **1807,** 1405–1412. arXiv: `NIHMS150003` (2010).

169. Yoshimura, Y., Lin, Y., Yagi, H., *et al.* Distinguishing crystal-like amyloid fibrils and glass-like amorphous aggregates from their kinetics of formation. *Proceedings of the National Academy of Sciences* **109,** 14446–14451 (2012).

170. Bartolini, M., Naldi, M., Fiori, J., *et al.* Kinetic characterization of amyloid-beta 1-42 aggregation with a multimethodological approach. *Analytical Biochemistry* **414,** 215–225 (2011).

171. Bernstein, S. L., Wyttenbach, T., Baumketner, A., *et al.* Amyloid beta-protein: monomer structure and early aggregation states of Abeta42 and its Pro19 alloform. *Journal of the American Chemical Society* **127,** 2075–2084 (2005).

172. Bernstein, S. L., Dupuis, N. F., Lazo, N. D., *et al.* Amyloid-β protein oligomerization and the importance of tetramers and dodecamers in the aetiology of Alzheimer's disease. *Nature chemistry* **1,** 326–331 (2009).

173. Bleiholder, C. & Bowers, M. T. The Solution Assembly of Biological Molecules Using Ion Mobility Methods: From Amino Acids to Amyloid β-Protein. *Annual Review of Analytical Chemistry* **10,** 365–386 (2017).

174. Hoffmann, W., von Helden, G. & Pagel, K. Ion mobility-mass spectrometry and orthogonal gas-phase techniques to study amyloid formation and inhibition. *Current Opinion in Structural Biology* **46,** 7–15 (2017).

175. Pujol-Pina, R., Vilaprinyó-Pascual, S., Mazzucato, R. & Arcella, A. SDS-PAGE analysis of Aβ oligomers is disserving research into Alzheimerť s disease : appealing for ESI-IM-MS. *Scientific Reports* **5,** 1–13 (2015).

176. Young, L. M., Saunders, J. C., Mahood, R. A., *et al.* ESI-IMS-MS: A method for rapid analysis of protein aggregation and its inhibition by small molecules. *Methods* **95,** 62–69 (2016).

177. Gabelica, V. & Marklund, E. Fundamentals of ion mobility spectrometry. *Curr. Opin. Chem. Biol.* **42,** 51–59 (2018).

178. Soper, M. T., DeToma, A. S., Hyung, S.-J., Lim, M. H. & Ruotolo, B. T. Amyloid-β-neuropeptide interactions assessed by ion mobility-mass spectrometry. *Physical Chemistry Chemical Physics* **15,** 8952–8961 (2013).

179. Young, L. M., Mahood, R. a., Saunders, J. C., *et al.* Insights into the consequences of co-polymerisation in the early stages of IAPP and Aβ peptide assembly from mass spectrometry. *The Analyst* **140,** 6990–6999 (2015).

180. Zheng, X., Liu, D., Klärner, F. G., *et al.* Amyloid β-Protein Assembly: The Effect of Molecular Tweezers CLR01 and CLR03. *Journal of Physical Chemistry B* **119,** 4831–4841 (2015).

181. Martin, J. *LILBID-MS Analyse des α-Synuclein: Aggregation, Inhibierung, Antikörper* Masterthesis (Goethe-University Frankfurt, 2018), 1–68.

182. Landau, M., Eisenberg, D., Flot, D., *et al.* Molecular basis for amyloid-polymorphism. *Proceedings of the National Academy of Sciences* **108,** 16938–16943 (2011).

183. Shankar, G. M., Li, S., Mehta, T. H., *et al.* Amyloid-β protein dimers isolated directly from Alzheimer's brains impair synaptic plasticity and memory. *Nature Medicine* **14,** 837–842. arXiv: `arXiv:1011.1669v3` (2008).

184. Sandberg, A., Luheshi, L. M., Sollvander, S., *et al.* Stabilization of neurotoxic Alzheimer amyloid- oligomers by protein engineering. *Proceedings of the National Academy of Sciences* **107,** 15595–15600. arXiv: `arXiv:1408.1149` (2010).

185. Morel, B., Varela, L., Azuaga, A. I. & Conejero-Lara, F. Environmental conditions affect the kinetics of nucleation of amyloid fibrils and determine their morphology. *Biophysical Journal* **99,** 3801–3810 (2010).

186. Lieblein, T., Zangl, R., Martin, J., *et al.* Structural Rearrangement of Amyloid- β upon Inhibitor Binding Suppresses Formation of Alzheimer ' s Disease Related Oligomers. *Journal of American Chemical Society* **submitted** (2019).

187. Bleiholder, C., Dupuis, N. F., Wyttenbach, T. & Bowers, M. T. Ion mobility-mass spectrometry reveals a conformational conversion from random assembly to beta-sheet in amyloid fibril formation. *Nature chemistry* **3,** 172–177 (2011).

188. Huy, P. D. Q., Thai, N. Q., Bednarikova, Z., *et al.* Bexarotene Does Not Clear Amyloid Beta Plaques but Delays Fibril Growth: Molecular Mechanisms. *ACS Chemical Neuroscience* **8,** 1960–1969 (2017).

189. Abelein, A., Lang, L., Lendel, C., Gräslund, A. & Danielsson, J. Transient small molecule interactions kinetically modulate amyloid β peptide self-assembly. *FEBS Letters* **586,** 3991–3995 (2012).

190. Woods, A. G. Advancements of Mass Spectrometry in Biomedical Research. *Advances in experimental medicine and biology* **806,** 453–481 (2014).

191. Wang, Q., Zhuravleva, A. & Gierasch, L. Exploring weak, transient protein-protein interactions in crowded in vivo environments by in-cell NMR spectroscopy. *Biochemistry* **50,** 9225–9236 (2011).

192. Banks, W. A. Characteristics of compounds that cross the blood-brain barrier. *BMC neurology* **9,** S3 (2009).

193. Faller, P. Copper and zinc binding to amyloid-β: Coordination, dynamics, aggregation, reactivity and metal-ion transfer. *ChemBioChem* **10,** 2837–2845 (2009).

194. Weber, D. K., Sani, M.-A. & Gehman, J. D. A routine method for cloning, expressing and purifying Aβ(1-42) for structural NMR studies. *Amino Acids* **46,** 2415–2426 (2014).

195. Morgner, N. & Robinson, C. V. Massign: an assignment strategy for maximizing information from the mass spectra of heterogeneous protein assemblies. *Analytical chemistry* **84,** 2939–48 (2012).

196. Larriba, C. & Jr, C. J. H. Free molecular collision cross section calculation methods for nanoparticles and complex ions with energy accommodation. *Journal of Computational Physics* **251,** 344–363 (2013).

Part III

Supplementary Information

8 Time-Resolved Mass Spectrometry

Participation of Colleagues To gain the production of all the components on the way to construct a work-piece for LILBID-MS extension, the help of the workshop was necessary. Especially Markus van Tankeren and Christoph Langer assisted with the CAD construction of the components and physically produced the parts in the in-house workshop.
The in-house electrical engineer Jochen Feldhaar planned, refined and constructed the whole electronic system. A constant discussion enabled to optimize the electronic performance.
Jonathan Schulte worked as a master student on the production of the glass capillaries of the piezo-driven droplet generator.
Droplet combination (figure 2.9) as well as release from the Paul-trap (figure 2.10) was achieved by Tobias Fischer. Tobias Fischer was a master student who was working on the system during the time of the project.
Nils Hellwig assisted the construction of the transfer stage as well as the flight tube extension of the LILBID-MS. He planed the construction as well as communicated with the workshop to productively manufacture the components. He also supported in adjusting the optical path of the IR lasers onto the droplet in the newly developed flight tube.

Materials and Methods

Work-Piece Construction For planing of all constructions the 3D-CAD software *Autodesk Inventor 2017* was used. This simulates a design of each of the components which can be used as template for work-piece construction with a CNC machine in the in-house workshop. The materials of each of the components are described within the text.
Piezo-crystal tubes for droplet generation are of the type *c255 o2,2 i1,07 L13 wAg* by the company *PI Ceramics GmbH* with an inner diameter of 1.07 mm. The glass capillaries for droplet production are made of *borosilicate* with an

outer diameter of 1 mm and an inner diameter of 0.58 mm (*Science Products GmbH, GB100-10*). Positioning of the droplet generator respective to the Paul-trap is done with XY-stages *G065-040-000* by *QIoptiq Photonics GmbH*.
Visualization of the levitated droplet is done with a camera of the type *DFK 22AUC03* by the company *The Imaging Source Europe GmbH* through a N-BK7 window *WG11010-B* by *Thorlabs GmbH*. Illumination of the levitated droplet inside the Paul-trap is done with LEDs *Golden DRAGON plus, LCW W5AM* by *Osram* where the lenses *FL-90 LED-Lens* by *Showin Technology Co.,Ltd* were attached. Communication with the camera was with the software *IC Capture Version 2.4.642.2631* by *The Imaging Source* and recording of videos was with the freeware software *DVD Video Soft* Version *3.0.46.1030*.
For UV illumination of the levitated droplet a fused silica window *WG40530-UV* by *Thorlabs GmbH* was implemented in the box of the Paul trap. Adjusting of precise time-delays for droplet injection into the trap as well as ejection from the trap to the transfer stage is done with *Stanford Research Systems* type *DG535*.
The transfer stage and the explosion chamber are planned and constructed on the same way as the Paul-trap. The fibers for the light barrier of the transfer stage are purchased from *Thorlabs* made of the material *TPO*with a diameter of 600 µm and a numerical aperture of 0.39. The stop valve of the explosion chamber is of the type *Z950025* by *LH Leybold*.

Electronics Design and construction of the electronic system was done by the in-house electrical engineer Jochen Feldhaar. The main commercial parts are a signal generator (*AFG-2005* by *Good Will Instrument Co.*) and transformers for high-voltage production of AC signal with *Tauscher, 17025001 TEVFCH 84/43,5*. Applying a DC voltage to compensate for gravity acting on the droplet is done with the power supply *6116A* by *Hewlett Packard*. Transmission of the high-voltage signals to the Paul-trap is via pressure-sealed SHV connectors. Transmission of the electric signals for operating the droplet generator (the piezo-crystal actuation, as well as the charging and grounding electrode) is achieved with the pressure-sealed conduct *09-3111-81-04* by *Binder*.

System Characterization To simulate the process of droplet levitation *Simion 8.1* was used. The 3D-CAD design of the Paul-trap was transferred from *Autodesk Inventor* to the *Simion* workbench. This enables to precisely simulate the particle movement in the correct electric field. The properties of the simulated particle match those of the droplet: a water droplet with a diameter of 50 µm results in a mass of $4 \cdot 10^{16}\,u$, the amount of charges is assumed to be 2 pC [90].

To characterize the system for droplet levitation, videos were recorded using the camera *DFK 22AUC03* by the company *The Imaging Source Europe GmbH* with the freeware software *DVD Video Soft* Version *3.0.46.1030*. Those videos were analyzed with *Matlab 2011a*. Therewith, each frame of the video was digitized (with a value of zero where no droplet is appearing and a value of one with a droplet). This enables to determine the size of the area of droplet levitation, as well as the amount of frames with a levitated droplet and thus the levitation time (schematically shown in figure 8.1). For each data point in section 2.1.2 the levitation of at least three consecutive droplets was analyzed.

To determined the droplet size in figure 2.7 droplets from the generator were collected in an Eppendorf tube which enables to weigh the produced mass of the droplets within a specific time (several minutes). This enables to calculate the volume and thus the diameter of a single droplet.

Supplementary Figures

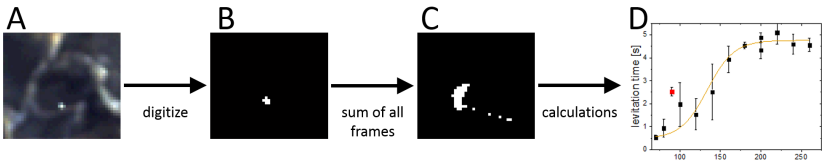

Fig. 8.1: A scheme of the principle of video recording the droplet levitation to determine the stability of levitation. A shows a frame of the video of a levitated droplet recorded through the recess of the upper cap-electrode. B shows the digitized version of that frame. By summarizing all frames the area of levitation can be determined; levitation time can be evaluated by counting the amount of frames a droplet is levitated. This is base for calculating levitation values depending on several parameters (D).

9 Mass Spectrometric Analysis of Amyloids

Participation of Colleagues The whole project was a highly collaborative work with Janosch Martin and Rene Zangl. Both supported to conduct most of the experiments. Discussion and interpretation of the results was done collectively.
Janosch worked on this project for his master thesis and especially conducted the experiments for insulin and α-synuclein (figure 5.1 as well as figure 5.2 and 5.3).
Rene Zangl worked on this project for his bachelor thesis, his master studies as well as for his master thesis. He contributed massively to the work shown in this dissertation. He conducted nearly all of the ESI-IMS measurements and contributed to the interpretation of the results. He also prepared the pictures for publication (figures 5.6, 5.9, 5.10, 5.11, 5.17, 5.18, 5.19 and 6.2). MD simulations of $A\beta$ oligomers (figure 5.10) were performed by Jan Hoffmann and Rene Zangl.

Materials and Methods

Peptide Conditions Human insulin was purchased from *Sigma-Aldrich* as solution of the recombinant peptide *I9278*. The peptide solution was buffer exchanged to guarantee MS suitability using *Micro Spin Columns P-6* by *Bio-Rad*.
Lyophilized α-synuclein was purchased from *rPeptide, S-1001-1*. It was dissolved in water, aliquoted to *LoBind Eppendorf* tubes, re-lyophilized and stored at -80 °C. The aliquoted and lyophilized peptide was resuspended with a buffer solution described in the main text and used for the experiments without a procedure for monomerization.
Synthetic $A\beta$ was purchased from *AnaSpec (AS-24224)* and prepared as published before [4]. For the purpose of monomerization the peptide was dissolved in hexafluoroisopropanol (HFIP) (*Sigma-Aldrich, 105228*) with 3 µl of concentrated NaOH. This solution was aliquoted to *LoBind Eppendorf* tubes and the solvent evaporated using a vacuum centrifuge (*Eppendorf,*

Concentrator plus). For the experiments, the dried peptide film was resuspended using 1% DMSO and a buffer solution indicated in the main text to the desired final peptide concentration.
Recombinant $A\beta$ was either prepared by Marie Hutchison using His-tagged SUMO fusion protein (this protocol was previously published by Weber et al. [194]) or by Johnny Habchi using a protocol published by Walsh et al. [159]. In terms of the former production method, the peptide was lyophilized and stored at -80 °C after purification. This recombinant peptide was used exclusively for the experiments to evaluate the effect of CLR01 (section 5.3.3). The latter production method requires monomerization with a 6 M GuHCl solution and a purification of the expressed $A\beta$ with size-exclusion chromatography on a FPLC system (*Äkta* using a *Superdex 75 10/300 GL* column). After purification the peptide was stored for a short time on ice and directly used afterwards. This recombinant production method was used exclusively to produce $A\beta$ for evaluating the effect of BMS493 (figure 5.13).

Conditions of Additives To evaluate the power of the two MS ionization techniques LILBID and ESI to catch specific oligomers zinc-phosphate (purchased from *Sigma-Aldrich, 587583*) was added to human insulin.
Bexarotene was purchased from *Sigma-Aldrich,SML0282*, solvated in DMSO and added to the $A\beta$ solution with respect to a total DMSO concentration of 1%. BMS493 was kindly supplied by Johnny Habchi, university of Cambridge. The peptide and peptidomimetics OR2 and TSP25 were synthesized by Tina Stark (as published in [4]). Both molecules were solvated in deionized water and stored at 4 °C. CLR01 was kindly provided by Thomas Schrader in collaboration with Marie Hutchison. It was stored in deionized water at -20 °C.

Experimental Conditions LILBID-MS measurements on $A\beta$ were conducted as published before [4]. Briefly, $A\beta$ was incubated with conditions as described in the text. 4 µl of the sample solution were loaded to a piezo-driven droplet generator (*MD-K-130* by *microdrop technologies GmbH*). It was assured that the laser intensity for ionization was below the damage threshold of $A\beta$ oligomers. The instrument was calibrated using *bovine serum albumin* (BSA). The MS signals of the negative ions of 500 droplets were averaged

to produce a mass spectrum. To calculate the monomer-to-oligomer ratio of the $A\beta$ peptide the formula

$$M/O = \frac{I_1}{\sum n \cdot I_n} \tag{9.1}$$

(where I is the intensity and n the oligomeric size of the respective peak) was used. At least 3 values were averaged to produce a data point. This procedure was repeated for each time point (except for the analysis of bexarotene in figure 5.12). To obtain the aggregation time course on short time-scales the sample was incubated within the capillary of the droplet generator. The solutions for analyzing the effect of BMS493 contained 5 µM DNA which does not interact with $A\beta$. The DNA with the sequence of CACCCTAACTCA-CACACATTCT and a molecular weight of 6544 g/mol was purchased from *BioSpring* as ammonium salt which was purified via ion exchange. The DNA was solvated at buffer conditions of the respective sample.

To process the LILBID-MS spectra the software *Massign* was used [195]. With this tool the raw spectra were calibrated, smoothed and background subtracted. For calculating M/O values *Matlab 2011a* was used.

ESI-MS measurements were performed on a *Synapt G2S* by *Waters Corpn.* with a high-mass upgrade of the quadrupole. The positive ion mode was used with a capillary voltage of 1.9 kV. The cone had a voltage of 100 V with an offset of 80 V. No backing pressure was used, the source temperature was adjusted to 20 °C. Calibration of the instrument was done with a conventional CsI solution.

IMS experiments were performed on the same instrument as for the ESI-MS measurements. Before starting an IMS experiment the instrument was equilibrated for 1 h. A travelling wave with a height of 40 V, a velocity of 700 m/s and a gas flow of nitrogen of 90 ml/min resulting in a pressure of 3.5 mbar was used. Denatured cytochrome c, apo-myoglobin and ubiquitin were used for CCS calibration. The procedure of this calibration followed the instructions given by Ruotolo et al. [42]. For CID and CIU experiments the collision voltage of the trap was varied in steps of 5 V from 5 V to 50 V.

Analysis of ESI-MS and IMS data was done with *Origin 2018* by *OriginLab Corporation*. This software was also used for data analysis and illustration of any of the figures shown in Part II of this thesis.

MD simulations were performed by Jan Hoffmann and Rene Zangl using the software *Gromacs 5.0.7*. Thereby different oligomer sizes were produced in MB and DB conformation of the PDB structures 5OQV and 2NAO. These simulations are necessary to compare solid-phase structures of uncharged

molecules (by ssNMR and cryo-EM) to gas-phase structures determined with IMS. 10 ns of structural changes were simulated using the force filed *AMBER99SB-ILDN*. The simulated structures were used to calculate the CCS with the *IMOS* software [196]. For CCS calculations gas, temperature and pressure were adapted to experimental conditions.

Supplementary Figures

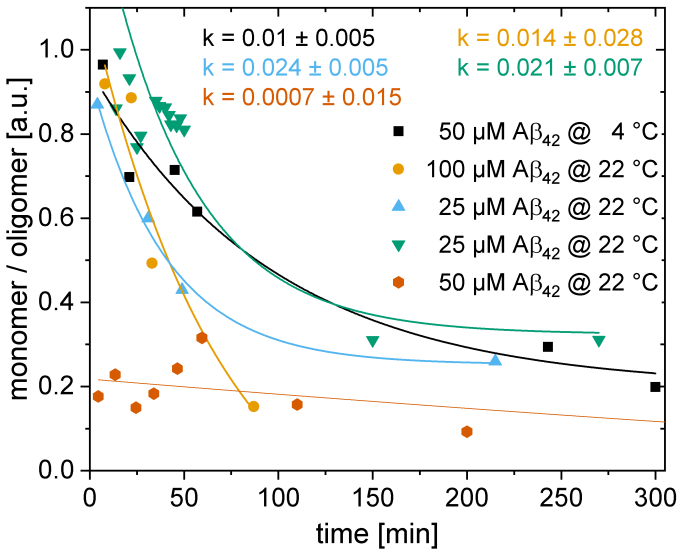

Fig. 9.1: Comparability of the time-course of Monomer-to-Oligomer values for different $A\beta_S$ incubation measurements.

A difference in the kinetic of $A\beta$ incubated at different temperatures can be determined even for $A\beta$ samples of different batches (figure 9.1). The exponential fits are of the form $M/O = A \cdot e^{-kt} + y_0$. The k-values of different measurements with the same concentration and incubation temperature are in good agreement (blue and green). Thus, kinetic measurements by LILBID-MS allows statements on the speed of oligomerization reactions. Nevertheless, in some cases $A\beta$ does not aggregate or is already aggregated at start of the experiment (red hexagons).

Figure 9.2 shows a comparison of the oligomerization kinetics of synthetic (black squares) and recombinant $A\beta$ (yellow circles and blue triangles). Both, the procedure for peptide production as well as the procedure for monomerization influence the aggregation kinetics. The monomerization using GuHCl with purification via SEC on a FPLC system leads to the fastes kinetic of the three treatments of $A\beta$; even if it has the lowest peptide concentration.

Figure 9.3A shows the ATD of the 9-times charged pentamer of $A\beta$ for low (upper), medium (middle) and high (lower) collision energies. Clearly, two natively folded species (8.5 ms and 10 ms) are detected which unfold upon collisions to the species at 12.5 ms and 16 ms, respectively. The collision

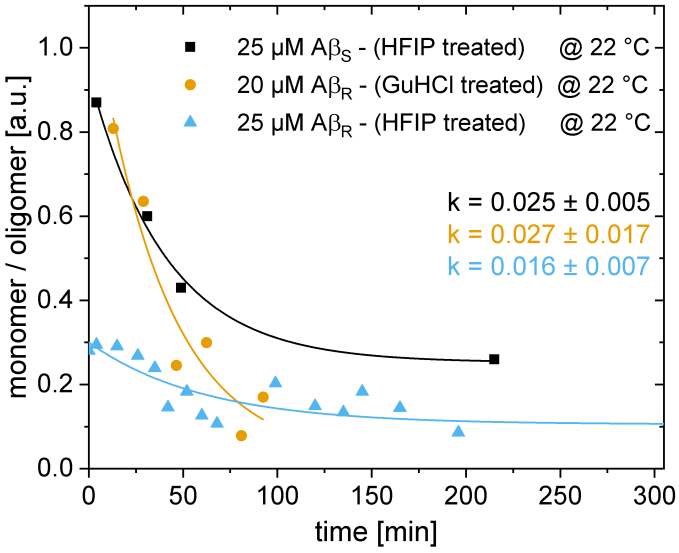

Fig. 9.2: Comparing oligomerization kinetics of recombinant and synthetic $A\beta$.

induced unfolding for different collision energies can be followed in B which shows the whole set of spectra as a heat map. The 8.5 ms species unfolds at an energy of about 180 eV into the species with an drift time of 12.5 ms, whereas the species of 10 ms unfolds at a higher energy of about 270 eV into the species with a drift time of 16 ms. Due to CCS calculations the smallest species at 8.5 ms can be assigned to the natively folded MB conformation, whereas the species at a drift time of 10 ms represents the DB conformed pentamer.

Figure 9.4 shows that 50 µM of free $A\beta$ aggregates with a normal kinetic, having a k-value of 0.032. The aggregation at start of incubation was un-

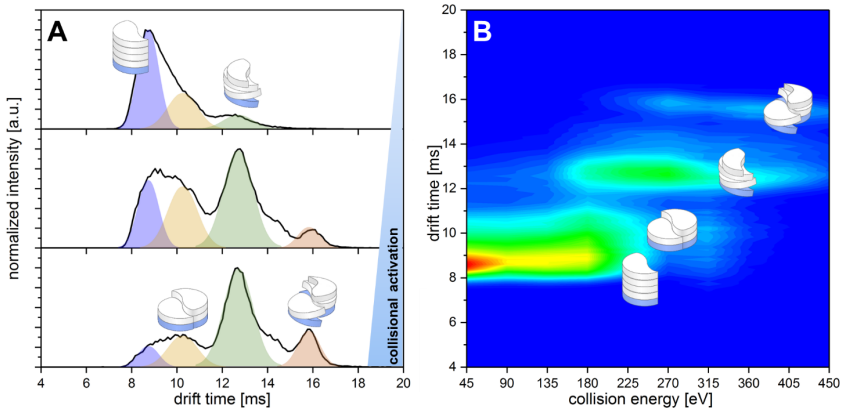

Fig. 9.3: ATD of an ESI-IMS CIU experiment on the 9-times charged pentamer.

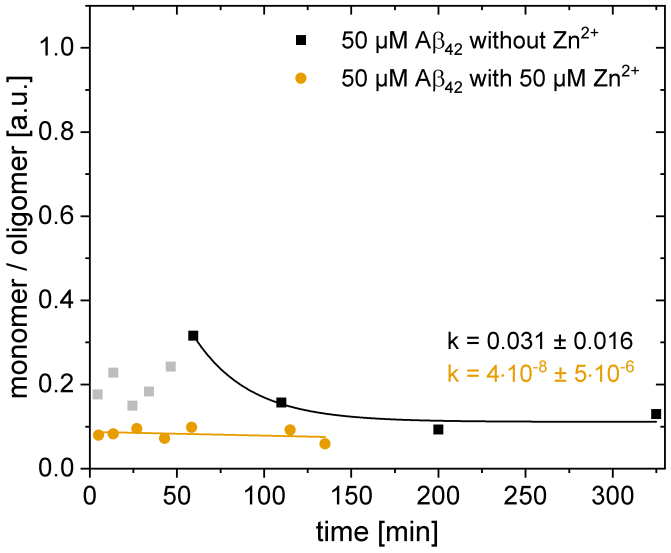

Fig. 9.4: Time-resolved LILBID-MS measurement of free and zinc-influenced $A\beta$.

usual and were excluded from the fit to determine the kinetic (gray points). This behavior was found several times. 50 minutes after start of the experiment, $A\beta$ aggregated regularly. The addition of an equimolar amount of zinc-phosphate results in an massive increase of the oligomerization which kinetic cannot be detected within the time necessary to operate the LILBID-MS instrument.

Part IV

Appendix

10 List of Figures

List of Abbreviations

11

$A\beta$	beta-amyloid
AD	Alzheimer's disease
AOI	analyte of interest
apoE	apolipoprotein E
APP	amyloid precursor protein
α**-syn**	α-synuclein
CCS	collision cross section
CMC	critical micelle concentration
CIU	collision induced unfolding
CID	collision induced dissociation
CNS	central nervous system
CSF	cerebrospinal fluid
DB	dimer base
DDM	n-dodecyl-β-D-maltoside
DMSO	dimethyl sulfoxide
DNA	deoxyribonucleic acid
EGCG	epigallocatechin-3-gallate
ESI	electrospray ionization
FDA	U.S. food and drug administration
FPLC	fast protein liquid chromatography
HDL	high-density lipoprotein
hIAPP	human islet amyloid precursor protein
HFIP	hexafluoroisopropanol
IMP	integral membrane proteins
IMS	ion mobility spectrometry
IR	infrared
KCl	potassium chloride
LB	Lewy bodies
LILBID	laser-induced liquid-bead ion desorption

MB monomer base

MD molecular dynamic

MS mass spectrometry

m/z mass-to-charge ratio

NMR nuclear magnetic resonance

PD Parkinson's disease

PPG photolabile protecting group

RAR retinoid A receptor

RF radio frequency

RNA ribonucleic acid

RXR retinoid X receptor

SEC size exclusion chromatography

SMALPs styrene maleic acid co-polymer lipid particles

ThT thioflavin-T

ToF time of flight

TR time-resolved

TW traveling wave

UV ultraviolet

13 Deutsche Zusammenfassung

Diese Dissertation befasst sich mit zeitaufgelöster Massenspektrometrie (MS). Da in dieser Arbeit sowohl die technische Weiterentwicklung des LILBID-MS Instruments, als auch die Anwendung von zeitaufgelösten Massenspektrometriemessungen zur Untersuchung des beta-amyloid Peptids gezeigt werden, ist das Dokument zweigeteilt.

Die Methode der LILBID Massenspektrometrie bringt einige Vorteile bei der Untersuchung von biologischen Systemen mit sich. So ist es zum Beispiel möglich, sowohl Membranproteine in einer nahezu natürlichen Umgebung zu untersuchen, als auch das Verhalten von nicht-kovalent interagierenden Proteinen. Die Ionisierung von Molekülen geschieht dabei durch den Beschuss von kleinen, die gelöste Probe enthaltenden Flüssigkeitstropfen mit Infrarotlasern. Die Absorption des Laserlichts resultiert in einer explosionsartigen Expansion des Tropfens, was wiederum die darin gelösten Moleküle in ihrem natürlichen Ladungszustand in die Gasphase transferiert. Dort können sie dann in einem Flugzeitanalysator (ToF, engl. für *time of flight*) untersucht werden.
Der ersten Teil befasst sich damit die LILBID Tröpfchen als Reaktionsgefäß für zeitaufgelöste MS Messungen zu nutzen. In den Tropfen soll eine Reaktion gestartet werden, die nach einer bestimmten Reaktionszeit massenspektrometrisch untersucht werden kann. Dafür ist es notwendig, die LILBID-Tropfen zu levitieren, um eine Manipulation der darin enthaltenen Probe zu ermöglichen. Hierfür wurde eine Paul-Falle entwickelt, die zur elektrodynamischen Speicherung von Tröpfchen dient. Im zweiten Teil wird die LILBID-MS Methode genutzt, um die Oligomerisierung des beta-amyloid ($A\beta$) Peptids zeitaufgelöst zu untersuchen. Mittels Ionenmobilitätsspektrometrie (IMS) kann zusätzlich die dreidimensionale Struktur des $A\beta$ Peptids untersucht werden. Die Kombination beider Methoden ermöglicht es, den Einfluss struktureller Attribute auf die reguläre Fibrillbildung zu ermitteln.

Paul-Fallen sind etablierte Instrumente, die z.B. in Massenspektrometern zur Analyse von Ionen genutzt werden können. Die Levitation eines Was-

sertropfens unterscheidet sich allerdings grundlegend von der eines Ions: sowohl die Masse, als auch die Ladungsmenge variieren drastisch. Deswegen müssen alle Eigenschaften der Paul-Falle auf diesen unkonventionellen Einsatz angepasst werden. Dies wurde mit einem Test-Setup realisiert, das die Entwicklung, Modifikation und den Austausch der einzelnen Komponenten ermöglicht. Es wurden sowohl Komponenten entwickelt, die das Erzeugen elektrisch geladener Tropfen ermöglichen, als auch ein Elektrodensystem, welches elektrodynamische Hochspannungsfelder erzeugen kann.

Um jedoch einen sinnvollen Ausgangspunkt für die zu testenden Parameter des elektrodynamischen Wechselfeldes zu haben, wurden Simulationen mit der Software *Simion* durchgeführt. *Simion* simuliert die Bewegung geladener Teilchen in einem elektrodynamischen Feld. Dadurch konnten die Größenordnungen der elektrischen Felder (Frequenz und Spannung) bestimmt werden, die eine Levitation von makroskopischen Partikeln erlauben.

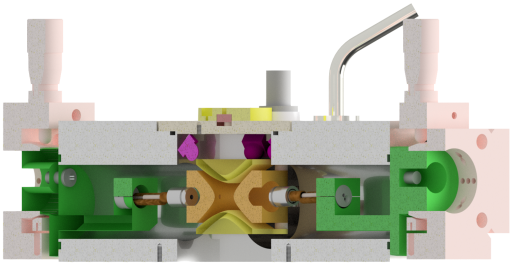

Fig. 13.1: Eine 3-dimensionale technische Zeichnung des Bauteils einer Paul-Falle zur Tröpfchenlevitation.

Mit Hilfe dieses Wissens konnte eine elektrische Schaltung entwickelt werden, die Hochspannungswechselfelder mit den passenden Kenngrößen erzeugen kann. Dies ermöglichte wiederum eine detaillierte Untersuchung der Levitationseigenschaften in Abhängigkeit von den elektrischen Parametern, sowie den Flüssigkeitseigenschaften. Dadurch konnten die Parameter zur Tropfenlevitation optimiert werden. Das Betreiben der Paul-Falle mit den optimierten Parametern ermöglicht eine akkurate und wiederholbare Levitation der LILBID Tröpfchen für einen Zeitraum von mehreren Minuten. Dies war die Grundlage für das Design und die Entwicklung eines Werkstücks zur Erweiterung des LILBID-MS Instruments.

Vorwissen über die Funktionsweise des herkömmlichen LILBID Instruments zeigt, dass die Überführung des Tropfens in das Hochvakuum des MS Instruments nicht ausgehen von Normaldruck möglich ist. Deswegen ist es nötig, die Tropfenlevitation in hermetischer Umgebung durchzuführen, in der ein kontrolliertes Vakuum erzeugt werden kann. Abbildung 13.1 zeigt eine 3-dimensionale technische Zeichnung des Bauteils zur Erweiterung des LILBID Instruments. Der Vollschnitt ermöglicht die Einsicht in das In-

nere des Gehäuses und damit einen Blick auf die einzelnen Komponenten. Zwei Tröpfchenwerfer mit metallischen Enden zur induktiven, elektrischen Ladung der Tropfen zielen auf die Ringelektrode der Paul-Falle (orange-gelb). Durch Öffnungen an exakt diesen Stellen kann ein Tropfen in die aktive Zone der Paul-Falle injiziert werden. Die Position der Tröpfchenwerfer kann im Mikrometermaß durch XY-Verschiebeeinheiten variiert werden. Visualisierung des levitierten Tropfens in der Falle wird durch eine Kamera (nicht gezeigt) erreicht, die auf den durch LEDs (lila) angestrahlten Tropfen fokussiert ist.

Ist ein Tropfen erfolgreich levitiert, kann die zu untersuchende Reaktion gestartet werden. Dies kann durch zwei Mechanismen geschehen: entweder in einem Tropfen befinden sich alle beteiligten Reaktanden, wovon einer mit einer photolabilen Schutzgruppe gecaged ist, oder durch Mischen zweier Tropfen, die jeweils nur einen Reaktanden enthalten. Photochemisches uncagen einer photolabilen Schutzgruppe kann durch Bestrahlung des Tropfens mit einem UV-Laser erreicht werden. Dieser kann durch ein Quarzkristallfenster (gelb an der Oberseite der Paul-Fallen Konstruktion in Abbildung 13.1) auf den levitierten Tropfen fokussiert werden. Beim Mischen zweier Tropfen enthalten die zwei gegenüberliegenden Tröpfchenwerfer jeweils einen Reaktanden. Wenn Tröpfchenwerfer A negativ geladene Tropfen erzeugt, kann ein schnelles und effektives Mischen dadurch erreicht werden, dass Tröpfchenwerfer B positiv geladene Tröpfchen erzeugt.

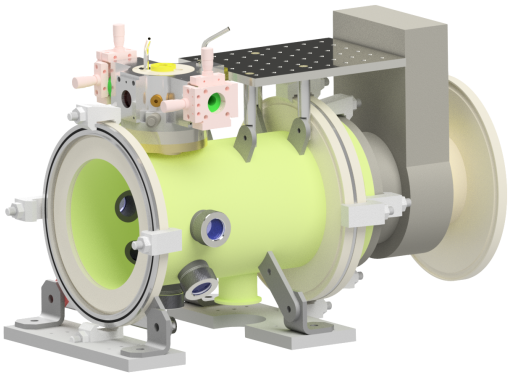

Fig. 13.2: Eine 3-dimensionale technische Zeichnung des gesamten Aufbaus für die zeitauflösende LILBID-MS Apparatur.

Nach dem Start der Reaktion muss der Tropfen nach wohl definierten Reaktionszeiten in das Hochvakuum des Massenspektrometers transferiert werden. Dafür wurde eine Transfereinheit mit einem differenziellen Zwischenvakuum entwickelt, für die Vorkenntnis vom herkömmlichen LILBID Instruments genutzt werden kann. Durch Abschaltung des levitierenden Wechselfeldes und Beschleunigung des Tropfens durch Erdgravitation wird der

Tropfen aus der Falle freigegeben. Die Geschwindigkeit der Tropfenfreigabe kann erhöht werden, wenn eine abstoßende Spannung an der oberen Kappenelektrode angelegt wird.
Abbildung 13.2 zeigt eine 3-dimensionale Technische Zeichnung des Anbaus der Tröpfchenfalle an das Flugrohr des Massenspektrometers. Die Transfereinheit (hier verdeckt durch die anderen Bauteile) ermöglicht die positionierbare Montage der Tröpfchenfalle auf dem Flugrohr des Massenspektrometers. Da im herkömmlichen Fall des LILBID Instruments die Flugbahn des Tropfens horizontal ist (durch einen Anbau an der linken Öffnung des Flugrohrs in Abbildung 13.2), der aus der Tröpfchenfalle ausgestoßene Tropfen jedoch eine vertikale Flugbahn hat, musste auch das Flugrohr des Massenspektrometers neu designt werden (gelblich in Abbildung 13.2). Diese Konstruktion ermöglicht den Anbau der Tröpfchenfalle an das LILBID Instrument.

Der zweite Teil der Dissertation widmet sich der massenspektrometrischen Untersuchung des $A\beta$ Peptids, dessen Oligomerisierung in Zusammenhang mit der Alzheimer Demenz gebracht werden kann. Die Oligomerisierung von $A\beta$ führt über neurotoxische *on-pathway* Oligomere zur Ausbildung von Fibrillen, sogenannte Plaques. Ziel dieses Teils ist es, den Mechanismus der Oligomerisierung zu verstehen und gezielt zu beeinflussen, sodass die Ausbildung von Plaques verhindert werden kann. Dafür wird LILBID-MS, mit der die Oligomerisierungskinetik bestimmt werden kann, mit Ionenmobilitätsspektrometrie, zur Bestimmung der Peptidstruktur, genutzt.

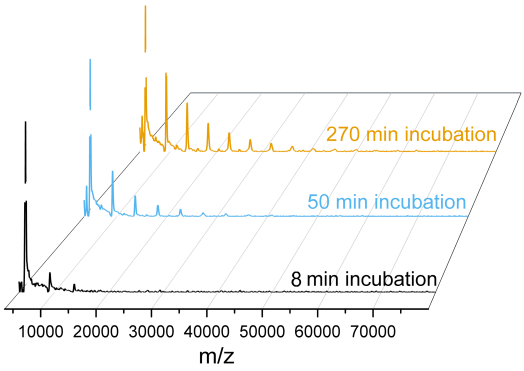

Fig. 13.3: LILBID-MS Spektren von $A\beta$ nach unterschiedlichen Inkubationszeiten (schwarz: 8 Minuten, blau: 50 Minuten, gelb: 270 Minuten).

Wie eingangs beschrieben, hat $A\beta$ die natürliche Eigenschaft, Oligomere auszubilden. Zur Untersuchung des Prozesses an sich ist jedoch eine Umkehrung der Oligomerisierung zu des Experiments notwendig. Verschiedene biochemische Verfahren sind in der Lage, die Oligomerisierung rückgängig zu machen und $A\beta$ zu monomerisieren. Ausgehend von diesem monomeren Zustand kann nun die Oligomerisierung untersucht und der Ein-

fluss verschiedener Liganden auf das Verhalten bestimmt werden.

Abbildung 13.3 zeigt LILBID-MS Spektren von $A\beta$ nach verschiedenen Inkubationszeiten. Direkt nach Versuchsbeginn (unteres, schwarzes Spektrum) zeigt die monomerisierte Probe nahezu keine Oligomere; lediglich eine kleine Menge $A\beta$ Dimer und Trimer können detektiert werden. Nach einer Inkubation bei Raumtemperatur von 270 Minuten kann jedoch der Vorschritt der Oligomerisierung beobachtet werden (oberes, gelbes Spektrum). Oligomere bis hin zum 11-mer können detektiert werden. Bei stetiger Aufnahme von Spektren während der Inkubation kann der Oligomerisierungsprozess zeitlich verfolgt werden, woraus letztendlich Kinetiken bestimmt werden können. Dies ermöglicht es, den Einfluss verschiedener Faktoren auf die Kinetik der $A\beta$ Oligomerisierung zu untersuchen.

So kann beispielsweise der Einfluss von Liganden unterschiedlicher Klassen (RXR und RAR Rezeptorliganden, Peptide und Peptidomimetika, die molekulare Pinzette CLR01) auf das Aggregationsverhalten und auf die Struktur von $A\beta$ untersucht werden. Abbildung 13.4 zeigt auszugsweise die Analyse der $A\beta$ Oligomerisierung unter Einfluss von OR Peptiden. LILBID-MS Spektren in Abbildung 13.4A zeigen die Interaktion des Liganden bereits unmittelbar zu Beginn der Inkubation (grüne und blaue Sternchen). Die Ligandinteraktion inhibiert das Voranschreiten der Oligomerisierung; selbst nach einer Inkubation von 48 Stunden kann kein Auftreten neuer Oligomere festgestellt werden. Dieser Befund eröffnet die Frage nach dem molekularen Mechanismus, der hinter der Inhibition der Oligomerisierung steht. Der strukturelle Einfluss des OR Liganden auf das $A\beta$ Peptid kann mit IMS untersucht werden und ist in Abbildung 13.4B für den $A\beta$-Dimer dargestellt. Der $A\beta$-Dimer zeigt unbeeinflusst von Liganden drei strukturelle Spezies (schwarzes Spektrum). Davon können zwei Spezies als nativen Strukturen ermittelt werden (die linken beiden Banden). Mit Hilfe von MD Simulationen

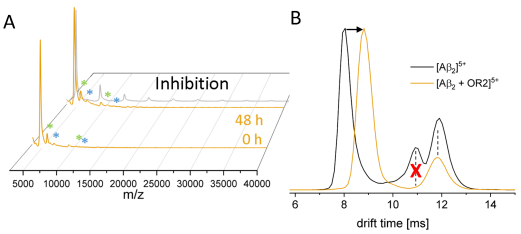

Fig. 13.4: Massenspektrometrische Untersuchung des Einflusses von Peptid-Liganden auf $A\beta$. LILBID-MS Spektren in A zeigen Inhibition der $A\beta$ Oligomerisierung, IMS Spektren in B zeigen den Einfluss auf die Struktur des $A\beta$-Dimers.

können diese nativen Strukturen verschieden angeordneten Dimeren zugeordnet werden. Die kleinere der beiden Strukturen zeigt einen Dimer, der aus parallel angeordneten Monomeren besteht. Diese Monomere liegen in axialer Richtung einer Fibrille übereinander und bilden eine monomere Basis (MB) für die Ausbildung von MB Oligomeren. Die größere native Dimerstruktur besteht aus Monomeren, die rotationssymetrisch in einer Ebene angeordnet sind (Ying-Yang ähnlich). Dimere mit diesem Arrangement führen zu $A\beta$ Oligomeren, die einen Dimer als Basis der fibrillären Struktur haben (DB). Die Interaktion von OR führt zu einer Vergrößerung der MB Struktur und gar zu einem Unterdrücken der DB Struktur. Diese strukturelle Änderung führt dazu, dass die Oligomerisierung von $A\beta$ inhibiert wird.

Das Unterdrücken der DB Struktur von $A\beta$ Oligomeren ist auch bei der Interaktion anderer Liganden der Fall (beispielsweise durch Interaktion der molekularen Klammer CLR01). In jedem dieser Fälle kann in elektronenmikroskopischen Bildern erkannt werden, dass sich kugelförmige, amorphe Aggregate anstatt geregelter fibrillärer Strukturen ausbilden. Amorphe Aggregate sind nicht neurotoxisch und können deswegen als ”gutartige” $A\beta$ Aggregate bezeichnet werden. Abbildung 13.5 zeigt dies schematisch. Der obere Reaktionspfad zeigt die Oligomerisierung von reinem $A\beta$. Oligomere dieses Weges bilden sich in in einem DB Arrangement und führen zu neurotoxischen Fibrillen (die elektronenmikroskopische Aufnahme wurde aus Sinha et al. [155] übernommen). Durch die Interaktion eines Liganden wird die DB Entwicklung von Oligomeren unterdrückt, was zu Oligomeren führt, die auf einem Monomer basieren. Elektronenmikroskopische Aufnahmen zeigen in diesem Fall amorphe Aggregate (ebenfalls aus Sinha et al. [155] übernommen). Amorphe Aggregate gelten als nicht neurotoxisch.

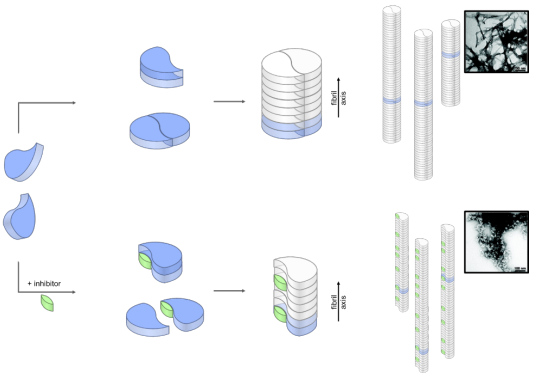

Fig. 13.5: Schema des Mechanismus der $A\beta$ Oligomerisierung.

Diese Ergebnisse zeigen, dass die Grundlage zur Bildung der verschiedenen Aggregate bereits beim Dimer gelegt wird. Experimente mit Massenspektrometrie und Ionenmobilitätsspektrometrie konnten den molekularen Mechanismus aufklären, der hinter der Entstehung neurotoxische Fibrillen

steht. Auf der Suche nach einer Behandlung der Alzheimer Demenz kann die Eigenschaft der Unterdrückung neurotoxischer Oligomere ein Ziel für die Entwicklung von Pharmazeutika sein. Massenspektrometrie in Kombination mit Ionenmobilitätsspektrometrie kann hierbei als schnelle und einfache Methode dienen, um diesen Effekt von $A\beta$ Liganden zu beobachten.